

UNCLASSIFIED

AD NUMBER

AD866979

LIMITATION CHANGES

TO:

Approved for public release; distribution is unlimited.

FROM:

Distribution authorized to U.S. Gov't. agencies and their contractors; Critical Technology; DEC 1969. Other requests shall be referred to U.S. Army Aviation Materiel Laboratories, Fort Eustis, VA 23604. This document contains export-controlled technical data.

AUTHORITY

USAAMRL ltr, 23 jun 1971

THIS PAGE IS UNCLASSIFIED

AD 866979

AD

## **USAAVLABS TECHNICAL REPORT 69-93**

### **HIGH-TEMPERATURE SENSORS FOR SMALL GAS TURBINES**

By

**A. Marshall Gaylord**

**W. A. Compton**

**December 1969**

**U. S. ARMY AVIATION MATERIEL LABORATORIES  
FORT EUSTIS, VIRGINIA**

**CONTRACT DAAJ02-68-C-0043**

**SOLAR DIVISION OF INTERNATIONAL HARVESTER COMPANY  
SAN DIEGO, CALIFORNIA**



This document is subject to special export controls, and each transmittal to foreign governments or foreign nationals may be made only with prior approval of US Army Aviation Materiel Laboratories, Fort Eustis, Virginia 23604.

Reproduced by the  
**CLEARINGHOUSE**  
for Federal Scientific & Technical  
Information Springfield Va. 22151

120



#### Disclaimers

The findings in this report are not to be construed as an official Department of the Army position unless so designated by other authorized documents.

When Government drawings, specifications, or other data are used for any purpose other than in connection with a definitely related Government procurement operation, the United States Government thereby incurs no responsibility nor any obligation whatsoever; and the fact that the Government may have formulated, furnished, or in any way supplied the said drawings, specifications, or other data is not to be regarded by implication or otherwise as in any manner licensing the holder or any other person or corporation, or conveying any rights or permission, to manufacture, use, or sell any patented invention that may in any way be related thereto.

#### Disposition Instructions

Destroy this report when no longer needed. Do not return it to the originator.





DEPARTMENT OF THE ARMY  
U. S. ARMY AVIATION MATERIEL LABORATORIES  
FORT EUSTIS, VIRGINIA 23604

The research described herein was conducted by  
Solar Division of International Harvester Company  
under U. S. Army Contract DAAJ02-68-C-0043.

Appropriate technical personnel of this Command  
have reviewed this report and concur with the  
conclusions contained herein.

The findings and recommendations outlined herein  
will be considered in planning future programs  
relating to turbine inlet temperature measurement  
techniques for gas turbine engines.



Task 1G162203D14416  
Contract DAAJ02-68-C-0043  
USAAVLABS Technical Report 69-93  
December 1969

**HIGH-TEMPERATURE SENSORS FOR  
SMALL GAS TURBINES**

**Final Report**  
**Solar Number RDR 1645**

**By**  
**A. Marshall Gaylord**  
**W. A. Compton**

**Prepared by**  
**Solar Division of International Harvester Company**  
**San Diego, California**

**for**

**U. S. ARMY AVIATION MATERIEL LABORATORIES**  
**FORT EUSTIS, VIRGINIA**

This document is subject to special export controls,  
and each transmittal to foreign governments or foreign  
nationals may be made only with prior approval of US Army  
Aviation Materiel Laboratories, Fort Eustis, Virginia 23604.

### ABSTRACT

Temperature sensors for application to the turbine inlet of small gas turbine engines were developed. Two thermocouple designs to sense gas temperature were developed and tested. An optical sensor for first-stage turbine blade temperature measurement was tested in the laboratory and on a gas turbine engine.

A bare multiple-junction platinum-rhodium thermocouple with a platinum-rhodium radiation shield was tested at temperatures to 2550°F. Response time, calibration, drift, and life were measured in a simulated gas turbine environment.

A rugged, protected thermocouple probe was developed using advanced materials systems able to operate in an oxidizing environment to 2800°F. The probe consists of a W-3Re versus W-25Re thermoelement grounded in the flattened tip of a tantalum protection tube. The tube is coated by a duplex silicide coating to prevent oxidation of the refractory metal components. The unique flattened tip, fabricated by diffusion bonding techniques, maximizes the response rate of the probe. Response in moving gas and lifetime in a thermal shock cycle were measured.

The radiation sensor consists of a silicon photovoltaic detector, a quartz lens, a high-temperature fiber optic bundle, an interface device, and a signal linearization system. It measures blade temperature and can resolve individual blades. The fiber optic bundle allows remote placement of the temperature-sensitive detector in a relatively cool environment. Silicon detectors provide high-temperature sensitivity and accuracy with an insensitivity to emittance and transmission errors. A unique interface device protects the optical system from transmission losses resulting from contamination of the optical system. Engine testing was performed with considerable success. The components functioned well over 16 start-endurance run-stop cycles. Reflected radiation from the flame caused a positive bias in temperature reading. Viewing of the backside of the blades will prevent this effect.

## FOREWORD

This report, prepared by the Solar Division of International Harvester Company, presents the laboratory development of several high-temperature sensors for small gas turbines.

The program was sponsored by the U. S. Army Aviation Materiel Laboratories (USAAVLABS) under Contract DAAJ02-68-C-0043 (Task 1G162203D14416). The USAAVLABS Project Engineer for the program was Mr. Roger G. Furgurson. The Solar Program Manager was Mr. W. A. Compton, Assistant Director of Research, and the principal investigator was Mr. A. Marshall Gaylord, Research Engineer.

Special acknowledgement is extended to staff members of the Solar Research Laboratory. Systems analysis and design of the Saturn Sensor Head were contributed by Mr. T. E. Duffy, Senior Research Engineer; design and construction of much of the test equipment were performed by Mr. R. L. Long, Senior Research Technician; and the Heat Transfer Analysis was performed by Mr. H. Mnew, Engineering Specialist.

**BLANK PAGE**

TABLE OF CONTENTS

	<u>Page</u>
ABSTRACT. . . . .	iii
FOREWORD . . . . .	v
LIST OF ILLUSTRATIONS. . . . .	viii
LIST OF TABLES. . . . .	xiii
LIST OF SYMBOLS . . . . .	xv
INTRODUCTION . . . . .	1
THERMOCOUPLES . . . . .	3
Thermocouple Error Analysis . . . . .	4
Fast-Response Thermocouple . . . . .	13
Long-Life Thermocouple Design and Fabrication. . . . .	30
Conclusions and Recommendations . . . . .	43
RADIATION SENSOR. . . . .	46
Design of a Radiation Sensor for a Turbine Engine . . . . .	46
Component Testing. . . . .	63
Simulated Atmosphere Testing . . . . .	77
Engine Testing . . . . .	81
Conclusions and Recommendations . . . . .	97
LITERATURE CITED . . . . .	99
DISTRIBUTION . . . . .	102

## LIST OF ILLUSTRATIONS

<u>Figure</u>		<u>Page</u>
1	Schematic Design for a Fast-Response Thermocouple . . . .	14
2	Thermocouple Response for Multijunction and Single-Junction Thermocouples. Times Are Shown as Multiples of the Time Constant $\tau_A$ . . . . .	17
3	Variation of Normal Pressure Around Right Cylinder . . . .	18
4	Moving Gas Test Rig . . . . .	21
5	Drift of Pt-30Rh Thermoelement During Exposure at 2550°F . .	22
6	Drift of Pt-6Rh Thermoelement During Exposure at 2550°F . .	23
7	Temperature-Time Cycle . . . . .	23
8	Typical Oscilloscope Traces of Response Tests . . . . .	25
9	Time Constant as a Function of Gas Velocity and Port Area . .	26
10	Time Constant of Exposed Junctions as a Function of Velocity and Wire Diameter. . . . .	26
11	Time Constant for a Shielded Thermocouple as a Function of Gas Velocity and Wire Diameter . . . . .	27
12	Time Constant Versus Gas Velocity for Exposed Thermocouples . . . . .	27
13	Radiation Shield of Pt-10Rh . . . . .	28
14	Time Constant Versus Gas Velocity for a Shielded Thermocouple . . . . .	29

# LIST OF ILLUSTRATIONS (Cont)

<u>Figure</u>		<u>Page</u>
15	Time Constant Versus Mass Flow for an Exposed Single-Junction Thermocouple . . . . .	29
16	Time Constant Versus Mass Flow for a Multijunction Thermocouple . . . . .	30
17	Design for a Long-Life Thermocouple . . . . .	31
18	Probe Tip Parallel (A) and Perpendicular (B) to Gas Flow. . . . .	31
19	Cold-Formed Tip of Long-Life Probe . . . . .	33
20	Bonded Long-Life Probe . . . . .	34
21	Microstructure of the TNV-7 Coating. . . . .	36
22	Test Specimens for Oxidation Tests in Moving Gas . . . . .	37
23	Cross Section of Failed Test Specimen . . . . .	37
24	Apparatus To Cycle Probes Into Moving Gas Streams . . . . .	38
25	W-Re Wires After 47 Hours of Exposure . . . . .	39
26	Typical Coating Failure . . . . .	40
27	Time Constant of a Long-Life Thermocouple Versus Gas Velocity . . . . .	41
28	Time Constant of a Long-Life Thermocouple Versus Mass Flow. . . . .	42
29	Time Constants for Three Tip Orientations. . . . .	42
30	Fast-Response Thermocouple . . . . .	44
31	Long-Life Thermocouple . . . . .	45

# LIST OF ILLUSTRATIONS (Cont)

<u>Figure</u>		<u>Page</u>
32	Blackbody Radiation . . . . .	47
33	Schematic Optical System . . . . .	49
34	Temperature Exponent . . . . .	51
35	Spectral Radiation . . . . .	54
36	Schematic Radiation Sensor Design . . . . .	55
37	Silicon Spectral Sensitivity . . . . .	56
38	Silicon Detector . . . . .	57
39	Operational Amplifier Circuit . . . . .	57
40	Interface Devices . . . . .	58
41	Logarithmic Amplifier Linearization System . . . . .	60
42	Detector Output Showing 11-Segment Linearization . . . . .	61
43	Diode Function Generator Linearization System . . . . .	63
44	Calibration Test Equipment . . . . .	64
45	Diode Calibration . . . . .	65
46	Diode Characteristics . . . . .	65
47	Amplifier Circuit Diagram . . . . .	66
48	Ambient Temperature Compensation . . . . .	66
49	Fiber Optic Bundle . . . . .	67
50	Fiber Optic Temperature Test . . . . .	68



LIST OF ILLUSTRATIONS (Cont)

<u>Figure</u>		<u>Page</u>
51	Collimator Interface . . . . .	71
52	Soot Tester . . . . .	72
53	Windows and Interface After Exposure . . . . .	73
54	Signal Linearizer . . . . .	75
55	Detector Input to Linearizer. . . . .	75
56	Linearized Signal . . . . .	77
57	High-Temperature Engine Simulator . . . . .	78
58	Target Holder and Blades . . . . .	79
59	Simulated Atmosphere Test . . . . .	80
60	Signal From Rotating Target Blades . . . . .	82
61	Radiation Sensor Mounted on the Test Engine . . . . .	85
62	Detector Housing and Fiber Optic . . . . .	86
63	Sensor Mount and Optical Housing. . . . .	87
64	Calibration Target . . . . .	88
65	Saturn Sensor Calibration . . . . .	88
66	Saturn Test Engine With the Radiation Sensor . . . . .	91
67	Start and Loading Cycle . . . . .	92
68	Oscilloscope Traces From Engine Tests . . . . .	93
69	Engine Shutdown. . . . .	95

LIST OF ILLUSTRATIONS (Cont)

<u>Figure</u>		<u>Page</u>
70	Oscilloscope Trace of Shutdown . . . . .	95
71	Effect of Fuel on Sensor Signal . . . . .	96

## LIST OF TABLES

<u>Table</u>		<u>Page</u>
I	Thermocouple Performance Objectives . . . . .	4
II	Thermal EMF and Thermoelectric Power of Three Platinum-Rhodium Thermocouples (Cold Junction at 32°F) . . . . .	15
III	Change of Thermal EMF with Time at 2822°F (1550°C) . . . . .	17
IV	Calibration Drift in Still Air. . . . .	20
V	Calibration Drift . . . . .	24
VI	Thermal Cycle Testing . . . . .	40
VII	Calibration of a Long-Life Probe . . . . .	43
VIII	Approximate Radiant Power/Unit Area . . . . .	50
IX	Data for Silicon Detectors . . . . .	52
X	Emissivity Errors for Spectral Radiation Sensors . . . . .	52
XI	Characteristics of Two Silicon Photodiodes. . . . .	55
XII	Calculated Logarithmic Linearization Errors . . . . .	62
XIII	Fiber Optic Temperature Data . . . . .	68
XIV	Extraneous Signal From Hot Fiber Optics . . . . .	69
XV	Optical Blockage . . . . .	70

LIST OF TABLES (Cont)

<u>Table</u>		<u>Page</u>
XVI	Interface Tests . . . . .	72
XVII	Adjustment of the Signal Linearizer . . . . .	76
XVIII	Signal Linearizer . . . . .	76
XIX	Transmission of Air Collimator . . . . .	89
XX	Detector Current . . . . .	90

### LIST OF SYMBOLS

A	area of the target
A <sub>O</sub>	area of the objective lens
A <sub>C</sub>	area available for convective heat transfer
A <sub>R</sub>	area available for radiant heat transfer
B	constant
C	heat capacity of the solid
C <sub>p</sub>	specific heat of the gas at constant pressure
C <sub>1</sub>	constant = $3.7412 \times 10^{-12} \text{ w - cm}^2$
C <sub>2</sub>	constant = $1.438 \text{ cm - }^\circ\text{K}$
d	diameter of wire
D	distance from objective lens to target
E <sub>C</sub>	conduction error
E <sub>R</sub>	radiation error
E <sub>T</sub>	total error
E <sub>V</sub>	velocity error
E <sub>T</sub>	response error
F <sub>t</sub>	transfer factor
F <sub>tc</sub>	transfer factor present during calibration

LIST OF SYMBOLS (Cont)

$g$	gravitational constant
$G$	mass flow
$h_c$	coefficient of convective heat transfer
$J$	mechanical equivalent of heat
$K$	constant
$k_f$	coefficient of thermal conductivity in the gas
$k_s$	coefficient of thermal conductivity in the solid
$K_R$	radiation form factor
$L$	immersion depth
$n$	temperature exponent
$N_{b\lambda}$	radiance (radiant power) from a blackbody emitted at a wavelength, $\lambda$
$N_\mu$	Nusselt number
$P_r$	Prandtl number
$R_\lambda$	responsivity of a detector
$S$	detector signal (current)
$t$	time
$T$	temperature of a solid body
$T_J$	junction temperature

LIST OF SYMBOLS (Cont)

$T_M$	mount temperature
$T_T$	total temperature of the gas
$T_W$	temperature of the wall to which the probe is radiating
$V$	velocity of the gas
$V_{in}$	input voltage
$V_o$	output voltage
$\alpha$	recovery factor
$\beta$	coefficient of reflection
$\gamma_j$	fraction of signal transmitted by optical element j
$\delta$	density of the wires
$\epsilon$	emittance
$\epsilon_c$	emittance value present during calibration
$\epsilon_\lambda$	emittance at wavelength, $\lambda$
$\epsilon_{0-\infty}$	total emittance
$\lambda$	wavelength
$\lambda_{max}$	wavelength at which the maximum radiance is emitted
$\mu$	dynamic viscosity
$\nu$	total number of air-glass interfaces
$\rho$	density of the gas
$\sigma$	Stefan-Boltzmann constant
$\tau$	time constant
$\phi$	radiant power arriving at the detector

**BLANK PAGE**



## INTRODUCTION

In the constant push for higher performance gas turbine engines, great premiums are placed on higher turbine inlet temperatures. The turbine inlet gases now exceed the allowable operating temperature for blade materials, which are normally cooled to within safe operating margins by compressor bleed air. Gas turbines of this general type offer the greatest potential for improvement in performance of aeropropulsion systems. They will need improved controls for efficient and dependable operation. The critical element of the control is the turbine inlet temperature sensor, which must protect vital engine hardware and sense gas temperature for power control.

The turbine inlet gas and the turbine blade temperatures are the two most difficult parameters to monitor in the advanced gas turbine. The temperature streaking of the turbine inlet gases makes the task of determining average temperature extremely difficult. The necessity of cooling the turbine blades to protect vital engine hardware makes determination of the turbine metal temperature even more difficult. Accurate and reliable measurements of these two areas are critical to the performance and life of advanced gas turbines. The efficiency, specific power, and weight factors dictate that the control operate the engine at the highest possible turbine inlet temperature. However, extreme caution in turbine control must be exercised, since even a small increase in metal temperature of the turbine blades will drastically decrease their creep life.

The critical effect of operational cost for the aircraft, as a function of turbine inlet temperature, makes it mandatory that maximum allowable turbine blade temperatures be maintained. A further example indicates that a 30°F change in turbine inlet gas temperature of a 1500-horsepower helicopter engine could change the payload by 700 pounds; thus, it becomes extremely important that accurate turbine inlet gas temperature sensors be developed.

The most popular method of controlling the turbine inlet gas temperature has been the use of thermocouples located in the turbine exhaust. By suitable extrapolation, it has been possible to determine the turbine inlet gas temperatures with sufficient accuracy to meet most engine requirements. An improvement of this method is the use of computers to sense compressor ratio and fuel flow, which also may be extrapolated to determine turbine inlet gas temperatures. An advanced gas turbine using compressor discharge air to cool the turbine blades, operating at a turbine

inlet gas temperature above the destruct temperature of the turbine blades, makes the previous method inadequate. Thus, a reexamination of the entire turbine inlet gas temperature sensor or transducer field of technology is in order.

This program has considered two approaches believed to be the most immediately available for advanced gas turbines in the early 1970's. One approach optimizes thermocouples for turbine inlet gas temperature measurements by employing the most up-to-date, high-temperature materials technology. Two thermocouple concepts are advanced and demonstrate technical feasibility. The first concept concentrates on fast response and employs a bare platinum-rhodium multiple-junction thermocouple to achieve response times of less than 100 milliseconds. The second, a grounded-junction thermocouple, achieves what is believed to be the optimum in response and lifetime at 2500°F. These thermocouples are available for immediate application to advanced gas turbines presently under development.

The second approach incorporates optical techniques to measure the metal temperature of the first-stage turbine blades. A rugged transducer was designed optimizing each component to fit the turbine engine environment. The radiation sensor consists of an interface device, quartz lens, and fiber optic bundle able to withstand environmental temperatures on the turbine case as high as 1000°F, a silicon photovoltaic detector, and a signal linearizer.

## THERMOCOUPLES

An ideal thermocouple placed at the turbine inlet of a small gas turbine engine for temperature measurement would be accurate, sensitive (large change in signal/unit change in temperature), rugged, durable, would offer small blockage to flow, and would respond quickly to changes in temperature.

The physical laws governing heat transfer and strength of materials dictate that a thermocouple with small mass and thus fast response will not demonstrate strength and ruggedness. In an attempt to resolve the dilemma posed by opposing goals, two designs are offered:

1. To optimize fast response characteristics
2. To concentrate on ruggedness

The choice of materials, methods of fabrication, and probe designs all stem directly from the basic purpose of each probe. Conditions at the inlet of a small gas turbine were defined in the work statement:

1. Gas temperature of 2500°F with possible excursions to 2800°F
2. Gas velocities of 700 fps
3. Gas pressure of 225 psia
4. Available gas passage size of 0.5 inch high, 0.25 inch wide, and 0.5 inch axial to the direction of gas flow

Three main parameters define thermocouple performance:

1. Accuracy
2. Response time
3. Service life

The test program concentrated on defining and optimizing these three parameters.

Performance objectives for each thermocouple were also defined in the work statement. They are summarized in Table I.

TABLE I. THERMOCOUPLE PERFORMANCE OBJECTIVES		
	Fast-Response Thermocouple	Long-Life Thermocouple
Design life*	50 hours	300 hours
Accuracy	±15°F	±30°F
Time constant	100 milliseconds	750 milliseconds
Allowable flow blockage	5 percent	10 percent
Signal strength at 2500°F	10 millivolts	25 millivolts
* Design life was specified in a thermal cycle 50 percent at 1800°F, 30 percent at 2200°F, and 20 percent at 2500°F with two excursions/hour to room temperature.		

General design considerations for thermocouples under the foregoing considerations will be discussed, with emphasis on analysis of the sources of temperature measurement error and considerations peculiar to small gas turbines.

**THERMOCOUPLE ERROR ANALYSIS**

A thermocouple is formed by joining two dissimilar materials, usually in the form of wires, into a circuit. An electrical potential is produced as a function of the temperature difference between the two junctions of the dissimilar materials. If one of the two is maintained at a known low temperature, then the emf produced is a measure of the temperature of the other, the hot junction. Material pairs are chosen to give a linear, reproducible output over as wide a temperature range as possible.

The accuracy with which a system of thermocouple probes is able to measure turbine inlet temperature may be defined as a function of the difference between the indicated average temperature and the average total gas temperature. There are five basic causes for error in a dynamic environment such as exists at the turbine inlet:

1. Failure of the hot junction to reach equilibrium at the total temperature of the gas
2. Deviation of the thermocouple from its standard calibration
3. Incorrect compensation for cold junction temperature

4. Failure of the system to give the correct average from a finite number of point measurements
5. Errors in the electrical system between the thermocouple and the readout or control system

Only the first three will be considered in detail. Averaging errors will be discussed with the design of a system for a small gas turbine engine. The electronic signal conditioning for a thermocouple system will be relatively simple and free from large errors. Since the object of this program is to concentrate on the transducer itself, this error source will not be discussed. Another effect commonly considered as a "transient error" is the time lag between a change in gas temperature and the full knowledge of the change at the temperature readout. The following discussion of errors resulting from failure of the hot junction to reach the total gas temperature is based on an analysis by Moffat (Ref. 1).

The temperature of a thermocouple immersed in a moving gas is determined by the rate of heat transfer between the hot junction and its surroundings. Four mechanisms are important in establishing the temperature:

1. Conversion of kinetic to thermal energy in the boundary layer surrounding the junction
2. Radiation from the probe to the walls and from the flame to the probe
3. Conduction from the junction to its support
4. Convection from the boundary layer to the junction

The difference between the junction temperature and the gas total temperature at steady state is called the total error ( $E_T$ ). This error is the sum of errors caused by three distinct phenomena.

$$E_T = E_V + E_C + E_R \quad (1)$$

where  $E_V$  = velocity error ( $^{\circ}\text{F}$ )

$E_C$  = conduction error ( $^{\circ}\text{F}$ )

$E_R$  = radiation error ( $^{\circ}\text{F}$ )

The velocity error is caused by incomplete conversion of kinetic to thermal energy in the boundary layer surrounding the junction.

$$E_V = T_T - T_J = (1 - \alpha) \frac{V^2}{2gJC_p} \quad (2)$$

where  $T_T$  = total temperature of the gas ( $^{\circ}\text{R}$ )

$T_J$  = junction temperature ( $^{\circ}\text{R}$ )

$V$  = velocity of the gas ( $\text{ft sec}^{-1}$ )

$g$  = gravitational constant ( $\text{ft sec}^{-2}$ )

$J$  = mechanical equivalent of heat ( $\text{ft lb Btu}^{-1}$ )

$C_p$  = specific heat of the gas at constant pressure ( $\text{Btu lb}^{-1} ^{\circ}\text{R}^{-1}$ )

$\alpha$  = recovery factor

The  $V^2/2gJC_p$  term represents the total kinetic energy of the moving gas. The recovery factor ( $\alpha$ ) is the fraction (experimentally determined) of the total kinetic energy that is recovered at the boundary layer. Only two terms of this equation may be varied by the designer: the velocity of the gas ( $V$ ) and the recovery factor ( $\alpha$ ). The velocity to which the junction is exposed may be controlled by surrounding the junction with a shield that adjusts the local velocity to a desired level. In the case of a turbine inlet sensor, the shield would serve to slow the gas, thus reducing the velocity error. There is less control over the recovery factor ( $\alpha$ ). At velocities of Mach 0.2 and above, the recovery factor is experimentally found to be

$$\alpha = 0.68 \pm 0.07 \text{ (wires normal to flow)}$$

$$\alpha = 0.86 \pm 0.09 \text{ (wires parallel to flow)}$$

These values are for junctions without a spherical bead. A welded bead tends to lessen the difference between normal and parallel flow, with both approaching 0.75. At lower velocities, the value of the recovery factor varies over a greater range. To minimize the error, the velocity must be reduced and the recovery factor increased by imposing parallel flow, if possible.

The conduction error is given by

$$E_C = T_T - T_J = \frac{T_T - T_M}{\text{Cosh } L \left( \frac{4h_c}{dk_s} \right)^{1/2}} \quad (3)$$

where  $T_M$  = mount temperature ( $^{\circ}\text{R}$ )

$L$  = immersion depth (ft)

$h_c$  = coefficient of convective heat transfer ( $\text{Btu ft}^{-2} \text{sec}^{-1} \text{ } ^{\circ}\text{R}^{-1}$ )

$d$  = diameter of the wire (ft)

$k_s$  = coefficient of thermal conductivity in the solid ( $\text{Btu ft}^{-1} \text{sec}^{-1} \text{ } ^{\circ}\text{R}^{-1}$ )

The equation represents a balance between heat gained by convection and heat lost by conduction. The coefficient of thermal conductivity of the thermocouple wires is fixed by the choice of materials. Two terms may be varied: the immersion depth ( $L$ ) and the coefficient of convective heat transfer ( $h_c$ ). The immersion depth should be made as long as possible while remaining compatible with size limitations and mechanical stability. The rate of convective heat transfer is a function of the properties of the gas and is characterized by the heat transfer coefficient

$$h_c = \frac{N_\mu k_f}{d} \quad (4)$$

$$N_\mu = 0.478 \left( \frac{\rho V d}{\mu} \right)^{1/2} P_r^{0.3} \quad (5)$$

where  $h_c$  = coefficient of convective heat transfer ( $\text{Btu ft}^{-2} \text{sec}^{-1} \text{ } ^{\circ}\text{R}^{-1}$ )

$N_\mu$  = Nusselt number

$k_f$  = coefficient of thermal conductivity in the gas ( $\text{Btu ft}^{-1} \text{sec}^{-1} \text{ } ^{\circ}\text{R}^{-1}$ )

$\rho$  = density of the gas ( $\text{lb ft}^{-3}$ )

$V$  = velocity of the gas ( $\text{ft sec}^{-1}$ )

$\mu$  = dynamic viscosity ( $\text{lb ft}^{-1} \text{sec}^{-1}$ )

$P_r$  = Prandtl number

The rate of convective heat transfer, and thus  $h_c$ , may be increased by increasing the local velocity of the gas and decreasing the diameter of the wires. These measures are contradictory since decreasing the diameter decreases the mechanical stability of the wires and thus their ability to withstand an increased velocity. In addition, the increased velocity will increase the velocity error.

The radiation error equation represents a balance between heat transferred by radiation and that transferred by convection. Unlike the other errors, the radiation error may be either positive ( $T_J > T_T$ ) or negative ( $T_J < T_T$ ). Positive errors result from direct radiation from the flame; negative errors result from radiation from the probe to the cooler walls. The junction itself may be shielded from direct radiation from the flame by a radiation shield that also controls the velocity of the gas passing over the junction.

$$E_R = T_T - T_J = \frac{K_R \sigma \epsilon A_R (T_J^4 - T_W^4)}{h_c A_C} \quad (6)$$

where  $K_R$  = radiation form factor

$\sigma$  = Stefan-Boltzmann constant ( $\text{Btu sec}^{-1} \text{ft}^{-2} \text{°R}^{-4}$ )

$\epsilon$  = emittance

$A_R$  = area available for radiant heat transfer ( $\text{ft}^2$ )

$A_C$  = area available for convective heat transfer ( $\text{ft}^2$ )

$T_W$  = temperature of the wall to which the probe is radiating ( $\text{°R}$ )

The radiation error is again decreased by increasing  $h_c$ ; that is, by increasing the velocity and decreasing the diameter. It is also decreased by increasing the wall temperature to which the junction radiates. This decrease is accomplished by surrounding the junction with a radiation shield. The shield temperature is much closer to the total gas temperature than either the flame or the walls and



thus reduces the radiation error. The emissivity is fixed by the choice of materials, which is dictated by the maximum design temperature and other considerations.

The time lag between a change in gas temperature and a corresponding change in junction temperature is an exponential function of time.  $E_\tau$ , the difference in temperature, is given by:

$$E_\tau = T_T - T_J = \tau \frac{dT_J}{dt}$$

$$\tau = \frac{\delta C d}{4h_c} \quad (7)$$

where  $\delta$  = density of the wires ( $\text{lb ft}^{-3}$ )

$C$  = heat capacity of the solid ( $\text{Btu lb}^{-1} \cdot \text{R}^{-1}$ )

$d$  = diameter of the wire (ft)

$t$  = time (sec)

$\tau$  = time constant

Decreasing the diameter and increasing  $h_c$  again improve the performance of the probe. An empirical relationship between the time constant,  $\tau$ , and conditions in the gas, developed by Moffat (Ref. 2), can be used to predict response rates for bare-wire junctions and to extrapolate experimental data to higher flow conditions.

$$\tau = \frac{3.5 \times 10^3 \delta C d^{1.25}}{T_T} G^{-15.8/\sqrt{T_T}} \quad (8)$$

where  $d$  = diameter of the wire (in.)

$G$  = mass flow ( $\text{lb ft}^{-2} \text{sec}^{-1}$ )

$T_T$  = total temperature of the gas

$\delta$  = density of the wires ( $\text{lb ft}^{-3}$ )

When applied to the case of a sheathed junction with geometry different from that of a bare-wire thermocouple for which it was developed, equation (8) can be modified to give

$$\tau = \frac{B}{T} G^{-15.8/\sqrt{T_T}} \quad (9)$$

where B is an experimentally determined constant dependent upon the thermocouple geometry, materials, and test conditions. The time constant,  $\tau$ , is also a function of the temperature,  $T_T$ , decreasing with increasing temperature in a linear fashion.

Designing a thermocouple probe to maintain acceptable accuracy requires the optimization of several parameters that have opposing effects on different portions of the total error. The use of a shield surrounding the junction is imperative to allow control of the junction environment. In particular, a shield allows control of the velocity and reduces radiation effects. The velocity must be maintained as high as possible while still maintaining an acceptable velocity error, and the wire diameter must be kept as small as possible commensurate with mechanical stability. The compromise must be reached by experimental methods rather than by analytical design.

A set of environmental conditions was assumed and the errors, associated with a simple exposed junction, were calculated. This assumption gives a basis for determining the factors that must be considered in the design of a turbine inlet thermocouple and indicates the distribution of the total error among the several mechanisms. The assumed conditions were:

Velocity	= 524 fps (M = 0.2)
Total Gas Temperature	= 2400°F
Pressure	= 225 psia
Wall Temperature	= 1500°F
Wire Diameter	= 0.010 inch

The maximum possible errors were calculated using equations (1) through (6) and the worst possible value for the thermocouple parameters, in particular recovery factor ( $\alpha = 0$ ) and emittance ( $\epsilon = 1.0$ ):

Maximum Velocity Error, $E_V$ (max.)	= -24°F ( $\alpha = 0$ )
Maximum Conduction Error, $E_C$ (max.)	= -3°F
Maximum Radiation Error, $E_R$ (max.)	= -62°F ( $\epsilon = 1.0$ )
Total Error, $E_T$ (max.)	= <u>-89°F</u> $\approx 3.8\%$

Calculation of the maximum errors shows that conduction error is not significant when compared with the radiation and velocity errors. Reasonable attention to immersion length (the only practical variable that can be varied to control conduction error) will reduce the conduction error to less than the maximum value.

Real values for the errors are obtained by assigning realistic values to the thermocouple parameters in place of the worst possible values used for the maximum error calculation. The maximum error indicates the magnitude of the problem and the magnitude of the dependence of the real error on the value of the thermocouple parameters. For instance, the real velocity error is calculated by multiplying the recovery factor by the maximum error. If the surroundings are changed to permit only a small maximum error, then the real error will be much less dependent on the value of the recovery factor, and changes or uncertainty in the recovery factor will cause smaller changes or uncertainty in the real error.

The real error for a bare-junction probe under the assumed conditions was calculated to be:

$$\text{Velocity Error} \quad E_V = -6^\circ\text{F} \quad (\alpha = 0.75)$$

$$\text{Conduction Error} \quad E_C = -2^\circ\text{F}$$

$$\text{Radiation Error} \quad E_R = -12^\circ\text{F} \quad (\epsilon = 0.2)$$

However, it must be emphasized that these calculations are approximate, and by changing assumptions the magnitude of the results can be changed greatly. The calculations show the distribution of the probable error of thermocouples at the turbine inlet and demonstrate the effect of such variables as immersion depth, wire diameter, and gas velocity.

The next step is to change the thermocouple surroundings to reduce the maximum error. This reduction is accomplished by placing a shield around the hot junction to act as a radiation shield and to slow the gas velocity around the junction. The shield approaches gas temperature and thus reduces the driving force for negative radiation errors. It also prevents positive errors resulting from direct radiation from the combustor. By adjusting the port sizes in the shield, the gas velocity inside the shield may be controlled to a desired level. An error analysis was made for this design, with the following assumption added to those already listed:

$$\text{Internal Velocity} \quad = 260 \text{ ft/sec} \quad (M = 0.1)$$

$$\text{Flame Temperature} \quad = 3000^\circ\text{F}$$

Wire Diameter = 0.010 inch

Shield Diameter = 0.125 inch

An error was calculated for both the shield and the junction so that the error associated with junction-to-shield radiation could be calculated. The velocity error was calculated assuming a recovery factor of 0.75 for the junction and 0.5 for the shield. The results were:

$$E_V \text{ shield} = -12^\circ\text{F} (\alpha = 0.5, V = 524 \text{ fps})$$

$$E_V \text{ junction} = -1.5^\circ\text{F} (\epsilon = 0.75, V = 260 \text{ fps})$$

Immersion depths of 0.375 inch for the junction and 0.5 inch for the shield were assumed in calculating the conduction error. Temperature gradients of 1000° and 1400°F were assumed for the junction and shield, respectively.

$$E_C \text{ shield} = -6^\circ\text{F}$$

$$E_C \text{ junction} \leq -1^\circ\text{F}$$

Radiation from the flame to the shield and from the shield to the wall was considered. The radiation error for the shield was established and added to the other components to give a total error and thus the shield temperature. The shield temperature was then used to calculate the error caused by radiation from the junction to the shield. A rise of +15°F was found to be caused by radiation from the flame, and a drop of -35°F was found to be caused by radiation to the walls, giving a total radiation error of about -20°F.

$$E_R \text{ shield} = -20^\circ\text{F}$$

The total error for the shield, including velocity and conduction, is -38°F. The maximum error is equal to -75°F.

The radiation error for the junction was calculated assuming a shield temperature 60°F cooler than the gas.

$$E_R \text{ junction} = -5^\circ\text{F} (\epsilon = 0.5)$$

The total error for the junction was then estimated to be

$$\begin{aligned} E_T &= E_V + E_C + E_R \\ &= (-2) + (-1) + (-5) = -8^\circ\text{F} \end{aligned}$$

The maximum error was calculated to be  $-17^\circ\text{F}$ .

These calculations show that it is necessary to reduce the radiation and velocity errors to maintain an acceptable thermocouple accuracy. The most straightforward manner is to use a single shield wall. Although it is possible to use a multi-walled shield, the enlargement in size and complexity is not warranted by the additional benefit over a single-walled shield.

The second source of error is a deviation from the standard calibration assigned to a particular pair of thermoelements. This deviation may be caused by compositional variations between as-received thermocouples, but it is not a serious problem. More important are deviations caused by compositional changes occurring during fabrication or use. Principal mechanisms for compositional change are diffusion, vaporization, and contamination. Contamination is probably the principal cause of drift during use. This is a difficult effect to measure if compositional gradients exist, since the emf of the thermocouple is then a function of the position of the thermal gradient as well as the magnitude of the gradient.

The third source of error is uncertainty in the cold-junction temperature. A thermocouple measures the difference in temperature between the hot junction and a cold junction maintained at a known temperature. Uncertainty of changes in the cold-junction temperature will cause errors in the thermocouple reading of the hot-junction temperature.

The discussion of averaging errors will be limited to the observation that a large number of thermocouples are needed to correctly average the turbine inlet gas temperatures. Steep radial and axial gradients exist and change with time and operating conditions. Careful design and experimentation will be needed to confirm that a given spatial arrangement of thermocouples results in an average reading within a specified accuracy. In addition, as the number of thermocouples increases, problems associated with blockage of the gas flow also increase.

#### FAST-RESPONSE THERMOCOUPLE

Experience demonstrates that only a bare-junction thermocouple will be able to meet the response time requirements for the fast-response thermocouple under

turbine inlet conditions. The error analysis showed that a shield is needed to meet the accuracy requirement. Figure 1 shows the basic design for a fast-response thermocouple to measure turbine inlet gas temperature. This design was fabricated and tested, and the results are reported here.

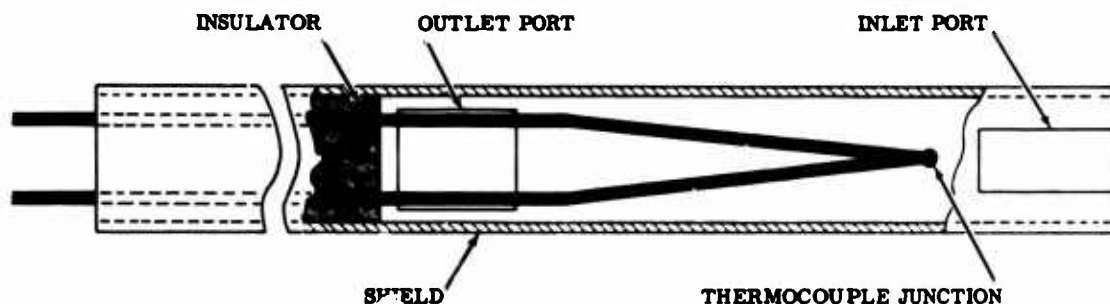


Figure 1. Schematic Design for a Fast-Response Thermocouple.

#### Materials, Design, and Fabrication

Platinum-rhodium is the only standard thermocouple alloy suitable for use at high temperatures (1500° to 2800°F) in an oxidizing atmosphere for long periods of time (Ref. 3 through 9). The lack of sufficient oxidation resistance eliminates most other possible choices. There are several platinum-rhodium alloys commercially available:

1. Pt versus Pt-10Rh
2. Pt versus Pt-13Rh
3. Pt-1Rh versus Pt-13Rh
4. Pt-6Rh versus Pt-30Rh
5. Pt-20Rh versus Pt-40Rh

Thermocouples with pure platinum as one of the thermoelements generally have higher thermal emf and higher sensitivity, but they suffer from lower thermoelectric stability and mechanical strength when compared with thermocouples with Pt-Rh alloys in both thermoelements of the thermocouple (Ref. 6).

The Pt-6Rh versus Pt-30Rh thermocouple combines the greatest number of desirable properties of the Pt-Rh system while minimizing its disadvantages. Table II compares the thermal emf (signal strength) and thermoelectric power (sensitivity) of three of the principal platinum-rhodium thermocouples. The Pt-20Rh versus

TABLE II. THERMAL EMF AND THERMOELECTRIC POWER OF THREE PLATINUM-RHODIUM THERMOCOUPLES (COLD JUNCTION AT 32° F)									
Thermocouple	Thermal emf and Thermoelectric Power								
	800°C 1472° F			1200°C 2192° F			1600°C 2912° F		
	mv	μv/deg C	μv/deg F	mv	μv/deg C	μv/deg F	mv	μv/deg C	μv/deg F
Pt versus Pt-13Rh	7.924	12.30	6.83	13.930	13.85	7.69	18.727	13.70	7.61
Pt-6 versus Pt-30Rh	3.162	7.55	4.19	6.811	10.50	5.83	11.260	11.30	6.28
Pt-20Rh versus Pt-40Rh	0.885	2.24	1.24	2.046	3.55	1.97	3.678	4.48	2.49

Pt-40Rh thermocouple has very low thermal emf and thermoelectric power at all temperatures of interest. The Pt-6Rh versus Pt-30Rh thermocouple compares more favorably. The thermal emf varies from 40 percent (3.162 mv) of the output of the Pt versus Pt-13Rh thermocouple at 1472°F (800°C) to 60 percent (11.260 mv) at 2912°F (1600°C). The thermoelectric power varied from 61 percent ( $4.19 \mu\text{v}/^\circ\text{F}$ ) to 82 percent at 2912°F ( $6.28 \mu\text{v}/^\circ\text{F}$ ) over the same range of temperature. Thermoelectric power is the most important parameter, and it compares favorably with the Pt versus Pt-13Rh thermocouple at high temperatures. At low temperatures, the thermal emf decreases to the point that the signal becomes very small (0.317 mv at 500°F). The low thermal emf is an advantage when cold-junction compensation is considered. The thermoelectric power is so low at room temperature that even large changes in cold-junction temperature will not affect the accuracy of the thermocouple. A 40-degree change at the cold junction will cause less than a 1-degree error at 2500°F. This is compared with a 17-degree error for a Pt versus Pt-10Rh thermocouple. Therefore, no cold-junction compensation is needed with the Pt-6Rh versus Pt-30Rh thermocouple, and errors caused by reasonable changes in cold-junction temperature are negligible.

Thermoelectric stability of the Pt versus Pt-10Rh thermocouple and that of the Pt-6Rh versus Pt-30Rh thermocouple are compared in Table III. The Pt-6Rh versus Pt-30Rh thermocouple is more stable with time than the Pt versus Pt-10Rh thermocouple. Acceptable stability is indicated for something over 200 hours for the Pt-6Rh versus Pt-30Rh alloy combination. Small changes in the rhodium content have been found to have a significant effect on thermal emf (Ref. 8). Contamination by iron and silicon (Ref. 9) causes drastic changes in thermoelectric and mechanical properties.

The Pt-6Rh versus Pt-30Rh thermocouple was best suited for use at the turbine inlet. The shield was also made of Pt-Rh alloy. A high rhodium content (up to 30 percent) was used for increased strength over pure platinum.

A multijunction thermocouple is shown in Figure 2 with its response to a step change in temperature and is compared to a single-junction thermocouple (Ref. 3 and 10). A single-junction thermocouple approaches steady state in an exponential manner (Equation 7). The multijunction thermocouple rises more rapidly, overshoots, and gradually returns to the steady-state value. A multijunction thermocouple is formed by three in-series junctions,  $A_1$ ,  $A_2$ , and B, placed so that they are isothermal during steady-state conditions. The resultant emf ( $E_T$ ) of the thermocouple is the sum of the emf of the three junctions:  $E_T = E_{A_1} + E_{A_2} + E_B$ .

At steady state,  $E_{A_1} = E_{A_2} - E_B$  and  $E_T$  is equal to the value for a single junction.

However, during transient temperature conditions, the junctions, being of unequal mass, respond at different rates ( $\tau_{A_1} = \tau_{A_2} > \tau_B$ ); the resultant emf responds



TABLE III. CHANGE OF THERMAL EMF WITH TIME AT 2822°F (1550°C)(Ref. 6)									
Time (hr)	Pt-6Rh Versus Pt-30Rh				Pt Versus Pt-10Rh				
	emf (μv)	Change in Output			emf (μv)	Change in Output			
		emf (μv)	Temperature			emf (μv)	emf (μv)	Temperature	
			(°F)	(°C)				(°F)	(°C)
0	9848	-	-	-	16460	-	-	-	
100	9763	85	13.8	7.7	16188	272	40.7	22.6	
200	9781	67	11.0	6.1	15974	486	73.3	40.6	
300	9662	186	30.5	16.9	-	-	-	-	
400	9422	426	69.2	38.4	15558	902	135.0	75.2	
500	9400	448	71.6	39.8	-	-	-	-	

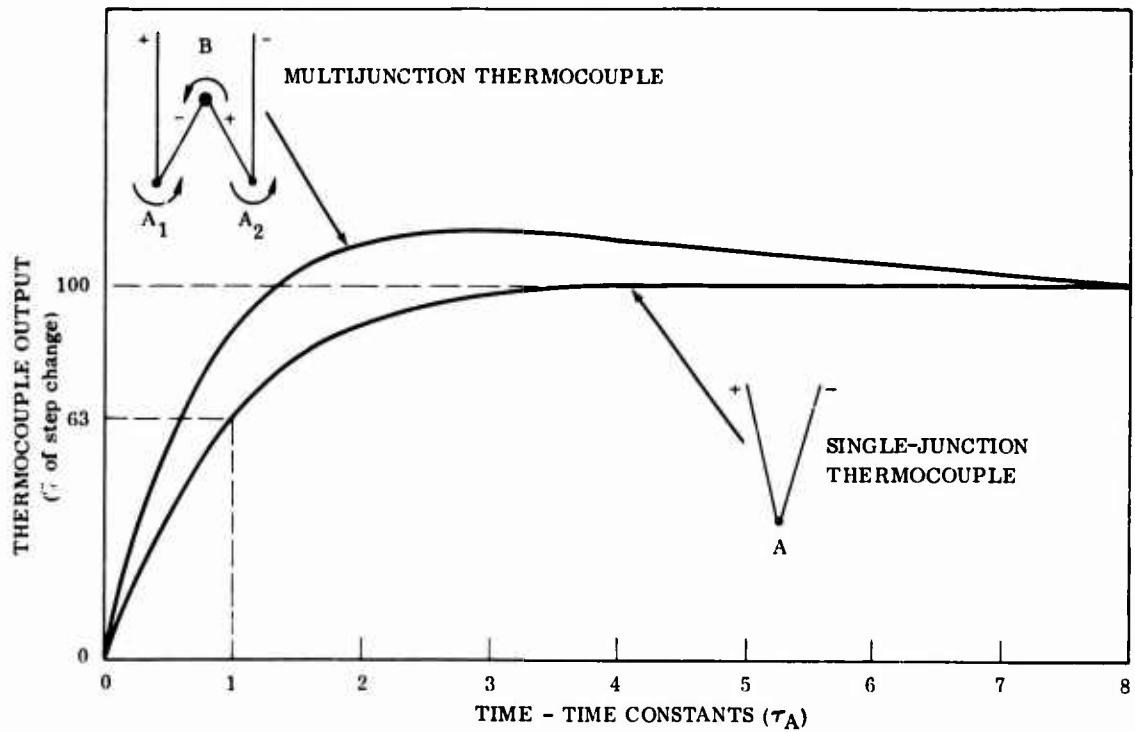


Figure 2. Thermocouple Response for Multijunction and Single-Junction Thermocouples. Times Are Shown as Multiples of the Time Constant  $\tau_A$ .

more rapidly than a single-junction thermocouple. The increased response and the magnitude of the overshoot are controlled by the ratio of  $\tau_A$  to  $\tau_B$ . A ratio of one to two results in a reduction of the thermocouple time constant by approximately 50 percent, with an overshoot of 12 percent.

Thermocouple junctions were formed by heliarc welding the respective wires together with a near-spherical bead. The bead was then paired to the proper size and tested experimentally to exhibit the desired response characteristics. High-purity alumina ( $\text{Al}_2\text{O}_3$ ), two-hole insulators were used. Plain copper wire is adequate as lead wire since the room temperature emf is very low.

The shield was formed from purchased Pt-Rh tubing. The end was closed by resistance welding a flat sheet over the end and trimming to size. The inlet and outlet ports were hand filed to size. Port shape and size determine internal gas velocity and were arrived at experimentally. The pressure differential between the upstream and downstream sides of the shield provides the driving force for flow through the probe. Pressure distribution around a cylinder perpendicular to flow is shown in Figure 3 (Ref. 11). To obtain the best advantage of the available pressure, the inlet port should be narrow to stay within the region of highest pressure ( $\pm 40$  degrees) while the outlet port can be considerably wider.

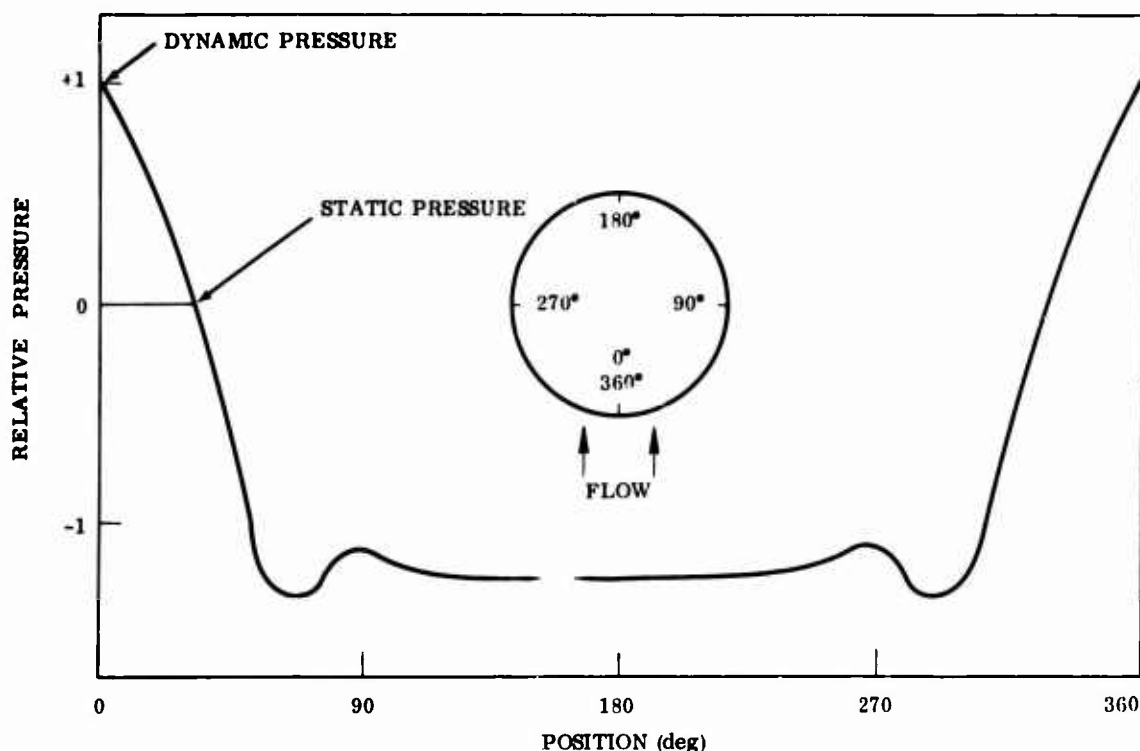


Figure 3. Variation of Normal Pressure Around Right Cylinder.

## Testing and Performance

The testing program for the fast-response thermocouple concentrated on three areas:

1. Defining the design variables
2. Thermocouple accuracy
3. Response rate

Design variables for the inlet and outlet port sizes and for the thermocouple wire diameter were established by testing and evaluation. Response rate, mechanical stability, and calibration stability were considered. Thermocouple accuracy was measured as a function of time in an atmosphere of moving hydrocarbon combustion products. Calibration changes with time; therefore, drift was measured for each thermoelement as well as for the thermocouple as a whole. The response rates of both single- and multijunction thermocouples were measured as a function of wire size, shield configuration (especially port size), junction size, and external gas velocity.

The resulting design was then tested for endurance by thermal cycling in moving combustion products.

### Calibration

Thermocouples were calibrated by comparison with a standard thermocouple. The techniques used complied with methods established by the American Society for Testing Materials (Ref. 12) and current practices as published in the literature (Ref. 13 through 17). Standard Pt-6Rh versus Pt-30Rh thermocouples manufactured in the United States have temperature-emf relationships that agree with the standard NBS calibration within  $\pm 0.5$  percent from 932°F (500°C) to 3272°F (1800°C), and within  $\pm 15 \mu v$  below 932°F. Calibration at three points (about 1000°, 1800°, and 2400°F) is sufficient to construct a deviation curve from the standard calibration that will be within  $\pm 6 \mu v$  up to 1960°F (Ref. 8). Therefore, the principal problem is defining the drift of the thermocouples with time during exposure to a turbine inlet environment. Drift and accuracy were measured by comparing the test thermocouples before and after exposure with a test standard made from the same spool of wire and in accordance with a NBS-traceable standard. The procedure was to join the test thermocouples with the test standard in a common bead hot junction. The NBS standard was placed in close thermal contact, and all were immersed in the hot zone. High-purity  $Al_2O_3$  insulation was used. The Pt-Rh wires went directly to an ice bath, where they were connected to copper leads by immersion in mercury. A Model K-3 Leeds & Northrup potentiometer measured

the emf. The test thermocouples, test standard, and NBS standard were compared at each temperature, and each leg of each thermocouple was compared to the leg of the test standard of like composition. There is no emf produced when two wires of equal composition are compared. However, if the test thermocouple becomes contaminated during exposure, a difference will appear. After the initial calibration was completed, the thermocouples were removed, the common bead was broken, and each thermocouple was remade. The test thermocouples were exposed in the same atmosphere and periodically checked by insertion of the test standard. After exposure, a common bead was again welded, including the test standard, and the complete calibration was repeated.

Baseline data were compiled in an atmosphere of still air in an electrically heated furnace (Table IV). The test standard and test thermocouples were found to be constantly 6 to 10 degrees (less than 0.5 percent) higher than the NBS standard. During the initial calibration, the difference between each test wire and the standard wire was insignificant (about one microvolt). After exposure for 175 hours at 2350°F, this difference increased to between 5 and 10 microvolts. This amount of drift is very low and indicates that the thermocouple is indeed stable in a clean oxidizing atmosphere.

TABLE IV. CALIBRATION DRIFT IN STILL AIR						
Thermocouple Reading						Sensitivity of Test Thermocouples at Temperature ( $\mu\text{V}/^{\circ}\text{F}$ )
NBS Standard ( $^{\circ}\text{F}$ )	Pt-6Rh Versus Pt-30Rh Test Standard		Differential*			
	$(^{\circ}\text{F})$	$(\mu\text{V})$	B4	B5	B6	
			$(\mu\text{V})$	$(\mu\text{V})$	$(\mu\text{V})$	
Initial Calibration						
1806	1812	4743	+1	-1	-1	5
2448	2458	8393	+1	0	-1	6
After 175 Hours of Exposure						
1819	1825	4808	+3	+1	0	5
2365	2375	7884	+6	+4	+2	6
* Difference between unexposed test standard and test thermocouples.						

### Drift in Moving Gas

Calibration drift of bare Pt-6Rh versus Pt-30Rh thermocouples was measured after exposure to moving hydrocarbon combustion products in the test rig (Figure 4). A natural-gas/oxygen flame is surrounded by secondary air ports. Adjustment of fuel, oxygen, and secondary air allows adjustment of the temperature and gas velocity over wide limits. The moving gas is directed through a 1.25-inch-inside-diameter ceramic tube and exhausted to the atmosphere. Ports that are cut at intervals through the ceramic tube allow insertion of test thermocouples into the gas stream. The thermocouples extended 0.75 inch into the gas stream, which was maintained at approximately 100 fps and at 2550°F (1440°C). Three test thermocouples of each wire size (0.010, 0.015, 0.020 inch in diameter) were assembled along with a laboratory standard made from the same wire stock. The four thermocouples were welded together to form a common bead. The group was then calibrated at three temperatures between 1500°F (816°C) and 2200°F (1204°C). Each test thermocouple was compared to the standard thermocouple, and each thermoelement of each test thermocouple was compared to the corresponding thermoelement of the standard. After initial calibration, the common bead was disassembled and the test thermocouples were exposed. At periodic intervals, the test thermocouples were rejoined to the test standard and calibrated.

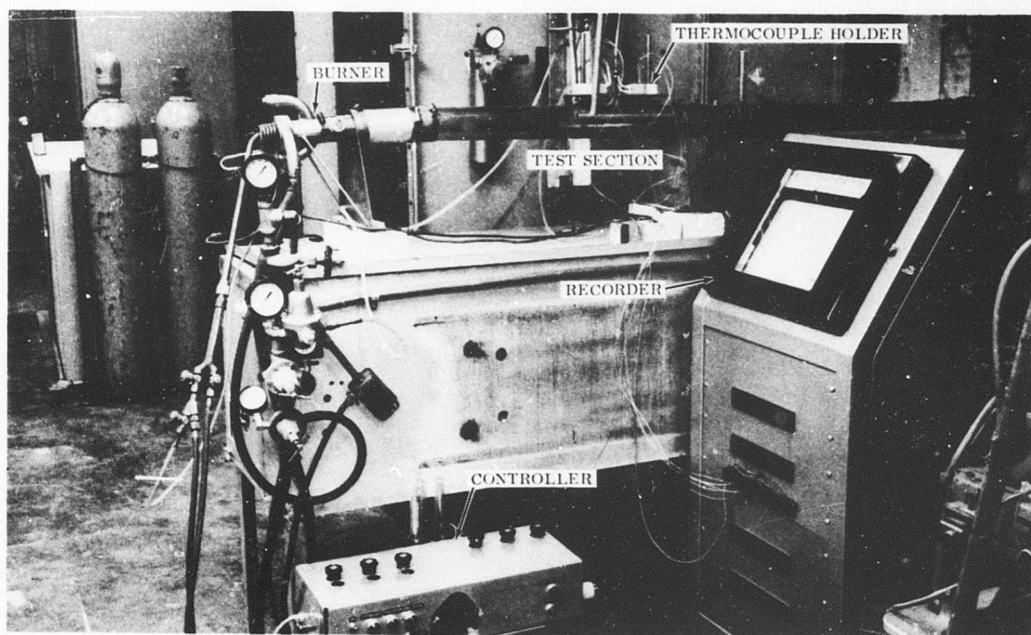


Figure 4. Moving Gas Test Rig.

A portion of the test standard was removed each time to ensure that uncontaminated wire was used as a standard. Fluctuations of the gas temperature limited the accuracy with which the thermocouples could be compared with the test standard. The calibration of the individual thermoelements was not affected, since the emf produced by a circuit of nominally homogeneous composition is only a slowly varying function of temperature. The calibration drift of thermoelements exposed at 2550°F was measured at 2200°F for each thermoelement as a function of time and is shown in Figure 5 for Pt-30Rh and in Figure 6 for Pt-6Rh. The low-alloy thermoelement (Pt-6Rh) is responsible for the largest part of the calibration drift. This drift would be expected since a given amount of compositional change caused by exposure would have a larger percentage effect on the composition of the lower alloyed element.

A 0.010-inch-diameter thermocouple was thermally cycled in the moving gas test rig. A 33-minute cycle of 15 minutes at 1800°F, 9 minutes at 2200°F, 6 minutes at 2500°F, and 3 minutes at room temperature (Figure 7) was imposed continuously on the shielded thermocouple. Neither the thermocouple nor the shield showed adverse effects from the thermal cycle. Grain growth was noted in the shield after several hundred hours.

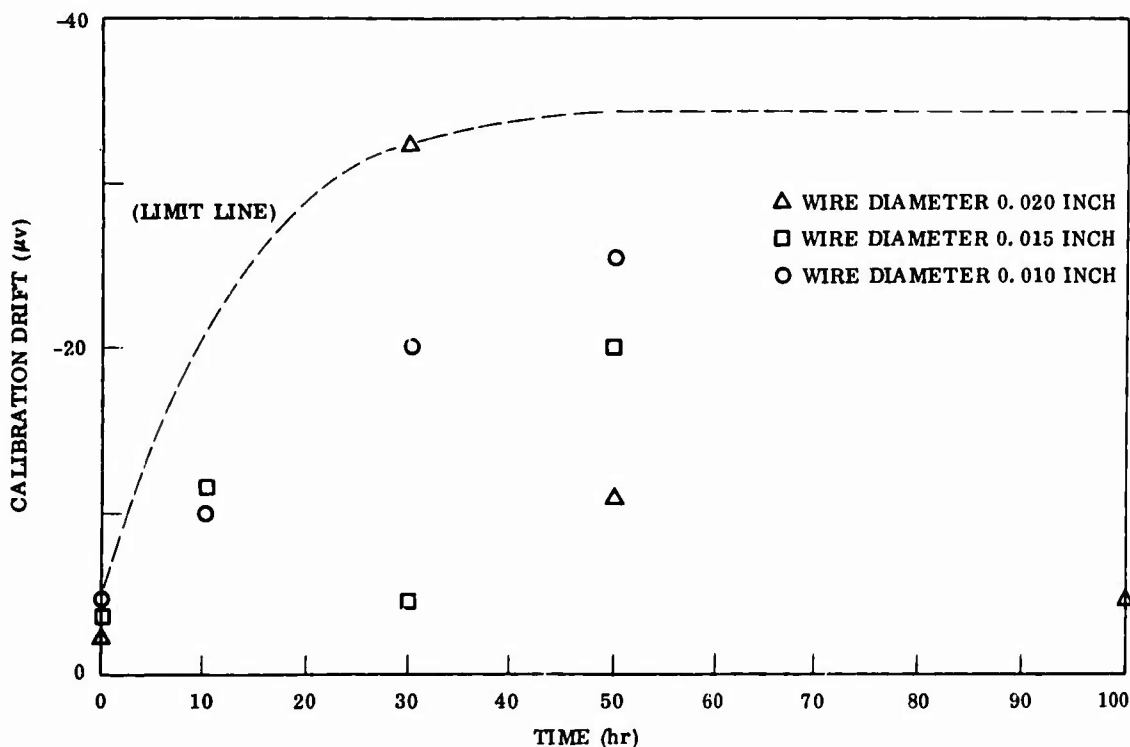


Figure 5. Drift of Pt-30Rh Thermoelement During Exposure at 2550°F.

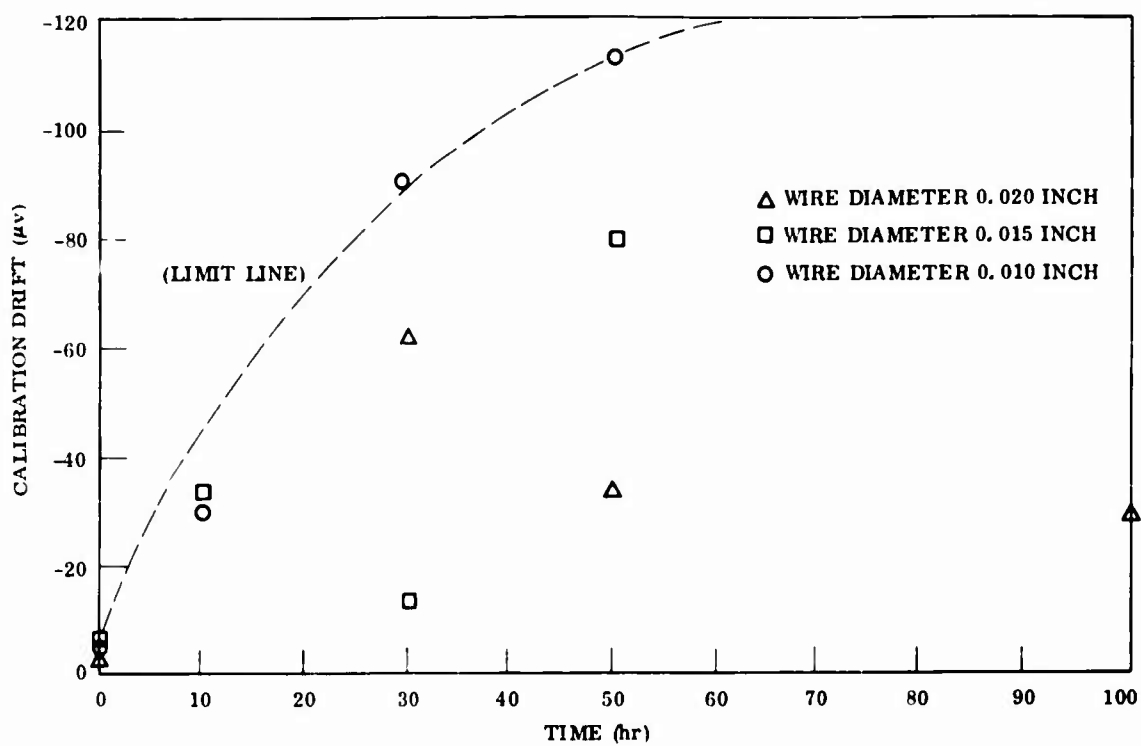


Figure 6. Drift of Pt-6Rh Thermoelement During Exposure at 2550°F.

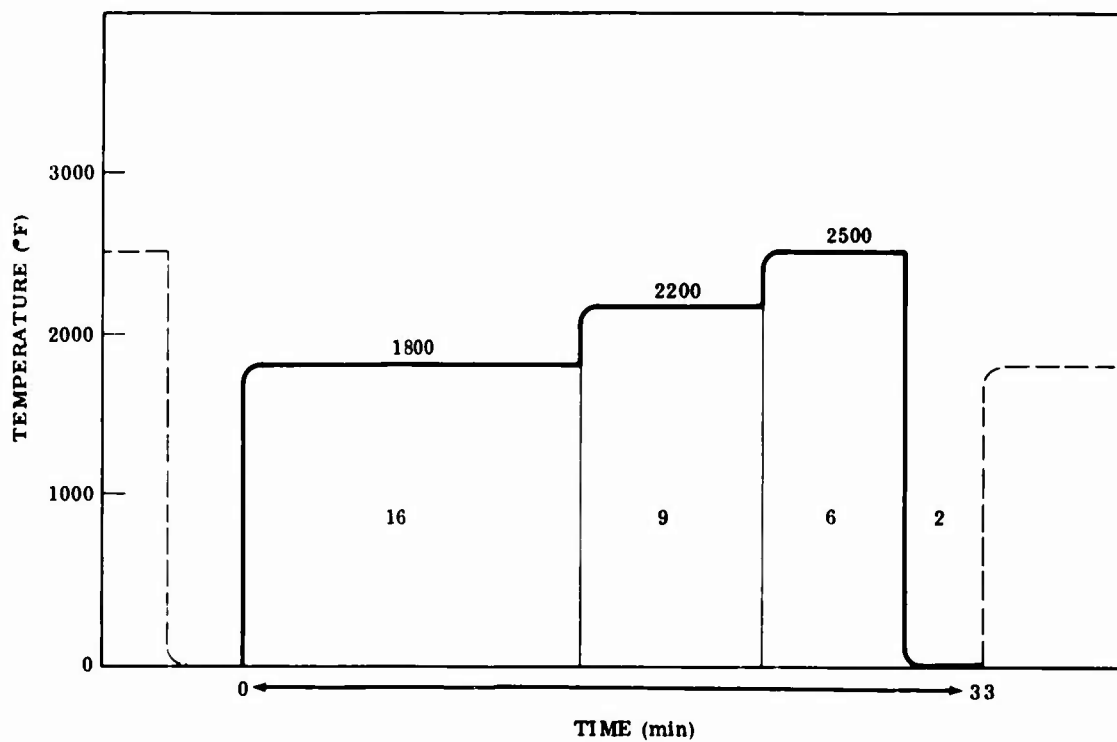


Figure 7. Temperature-Time Cycle.

Calibration drift after 50 hours was measured and is shown in Table V. The drift in each element is additive, so the total drift in millivolts and temperature is also indicated. The total drift is seen to be much smaller than that in the previous tests carried out at a constant temperature of 2550°F.

TABLE V. CALIBRATION DRIFT					
Temperature (°F)	Drift After 50-Hour Exposure		Total Change		
	Pt-6Rh Element (mv)	Pt-30Rh Element (mv)			
			(mv)	(°F)	(%°F)
1800	-0.013	-0.006	-0.019	3.7	0.21
2350	-0.021	-0.011	-0.032	5.3	0.23
2510	-0.029	-0.015	-0.04	7.1	0.28

#### Response Rate Measurements

Response to a step change in temperature was measured by recording the output of the thermocouple on an oscilloscope as a function of time after a step change in temperature. The step change was approximated by plunging the thermocouple from ambient conditions into the moving gas stream at 2000°F. The time consumed in transfer of the thermocouple through the temperature gradient zone was less than 10 milliseconds, better than an order of magnitude faster than the lowest time constant that was measured. Thus a step change in temperature was well approximated. Gas velocity was measured by a pitot tube immersed in the stream. The difference between ram and static pressure was measured by a water manometer. Typical oscilloscope traces of the response time tests are shown in Figure 8. A zero line was first recorded, then the output after the step change, and finally the steady-state signal after the temperature change. The time to record 63 percent of the total change was measured and was equated to the time constant for the thermocouple under the conditions present in the test.

The effect of port size on internal gas velocity and thus on thermocouple response was tested. Three 0.125-inch-diameter stainless steel probes were tested, each with a different port size. Outlet and inlet ports were of equal size on each probe. The thermocouple used for all tests was made of 0.010-inch-diameter Pt-Rh wire with a paired junction bead. The measured time constants are shown in Figure 9 as a function of gas velocity for the three shields. Response of the exposed thermocouple is shown for comparison.



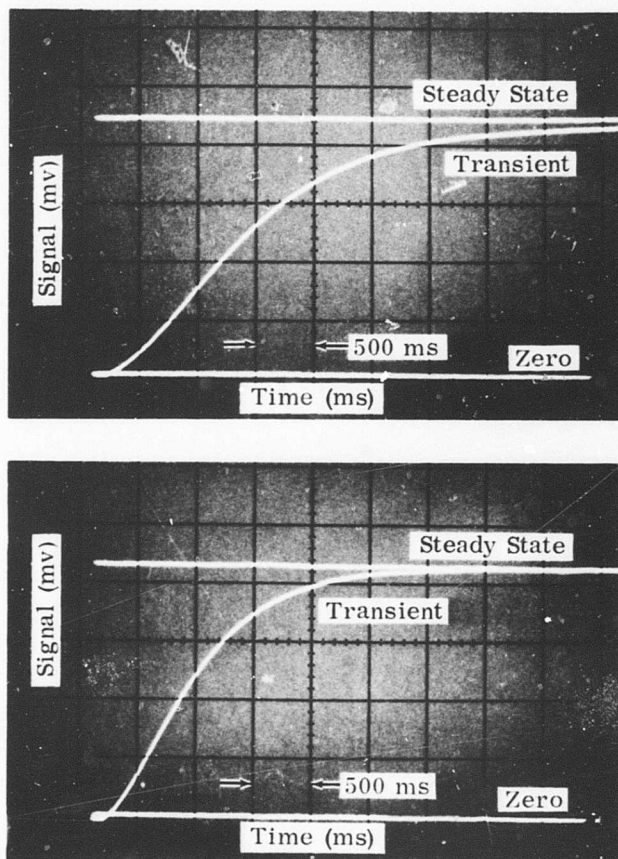


Figure 8. Typical Oscilloscope Traces of Response Tests.

The effect of wire size on response of shielded and exposed thermocouples was determined by testing fusion-welded thermocouples of three wire sizes: 0.005, 0.010, and 0.015 inch in diameter. Figure 10 shows the time constant as a function of gas velocity for each thermocouple. The comparison was also made in a 0.125-inch-diameter Pt-10Rh shield using the same thermocouple. The results are shown in Figure 11 as a function of external gas velocity. The decrease in response rate (increase in time constant) is attributed to the decreased gas velocity inside the probe and also to the thermal capacity of the shield itself.

Time constants may also be reduced by reducing the ratio of bead to wire size. The thermocouples tested with fusion-welded beads (Figure 10) were then modified to reduce the bead to approximately the size of the wire. These thermocouples were then response tested, and the data are shown in Figure 12. Time constants were reduced by about 50 percent.

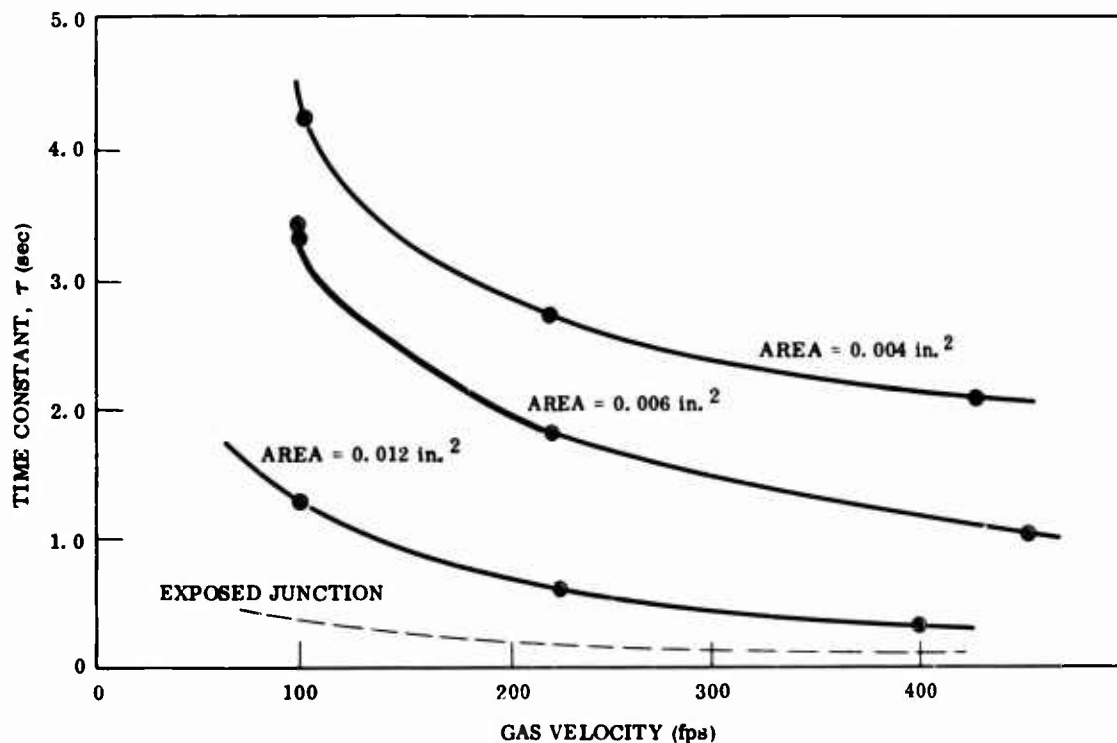


Figure 9. Time Constant as a Function of Gas Velocity and Port Area.

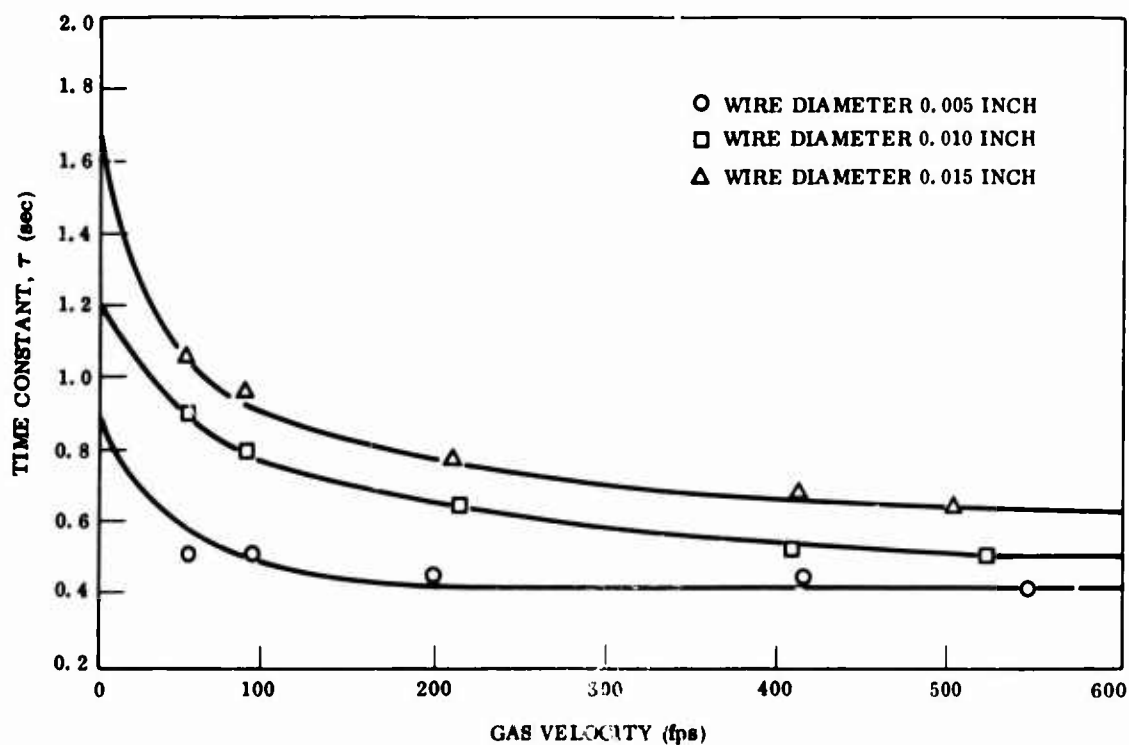


Figure 10. Time Constant of Exposed Junctions as a Function of Velocity and Wire Diameter.

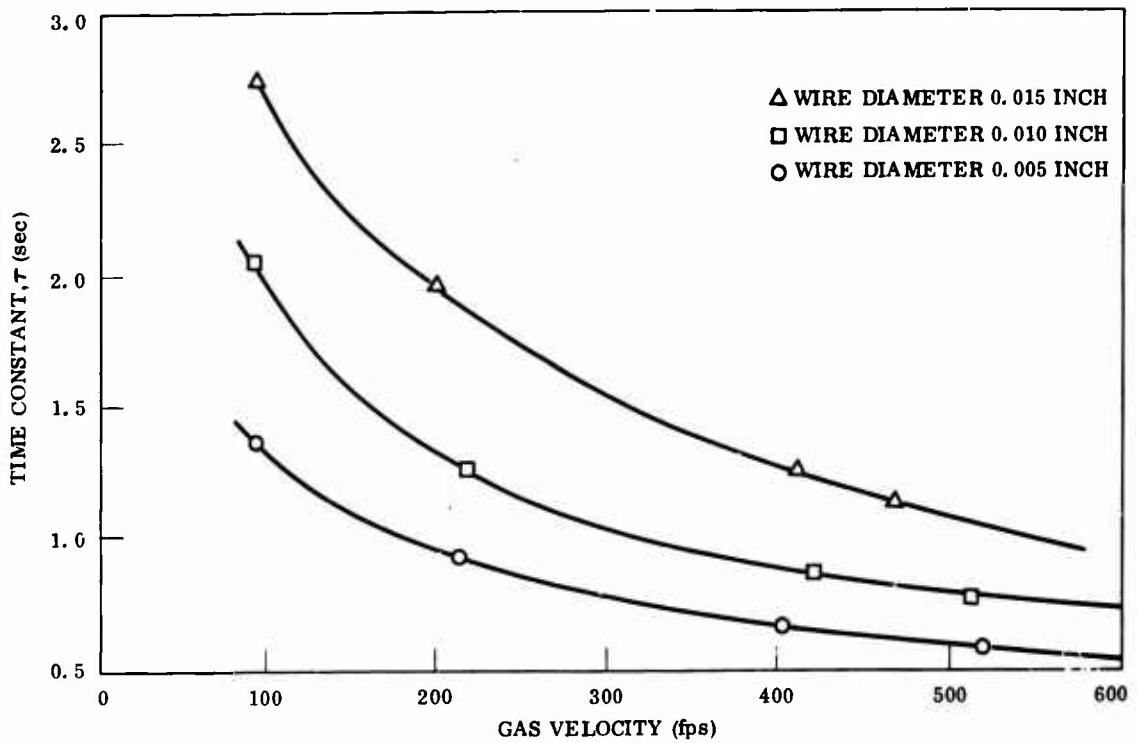


Figure 11. Time Constant for a Shielded Thermocouple as a Function of Gas Velocity and Wire Diameter.

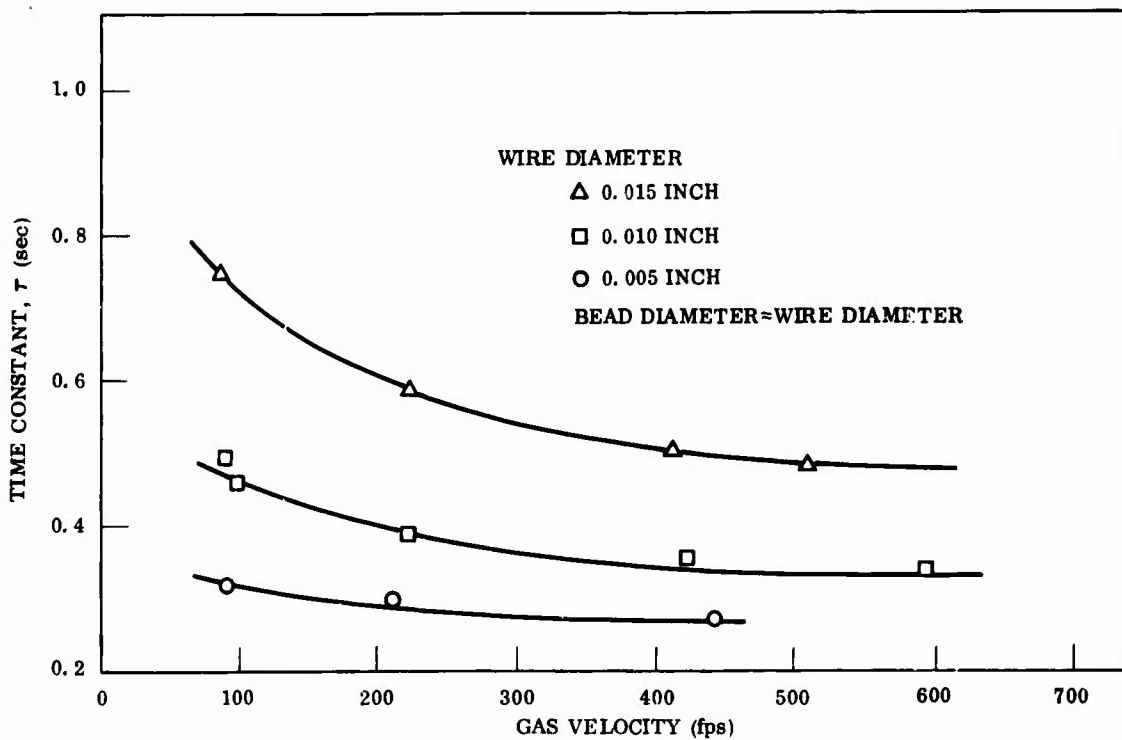


Figure 12. Time Constant Versus Gas Velocity for Exposed Thermocouples.

### Final Probe

A 0.125-inch diameter Pt-10Rh radiation shield was fabricated for final testing and is shown in Figure 13. The inlet port is 0.060 inch wide by 0.015 inch high with an area of 0.009 square inch. The outlet port is 0.105 inch wide by 0.125 inch long with an area of 0.013 square inch. The time constant of a paired 0.010-inch thermocouple inserted in the shield is shown in Figure 14.

The data reported above for tests conducted at atmospheric pressure and velocities up to 600 fps may be extrapolated to mass flow conditions by the use of equation (8). Figure 15 shows the time constant for two exposed fast-junction thermocouples extrapolated to high mass flows. Velocities of 100 to

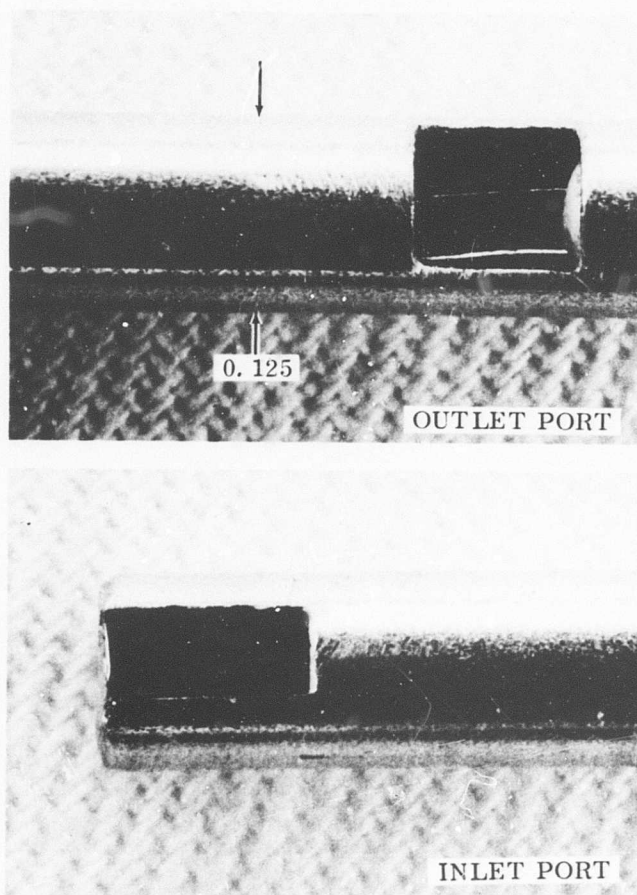


Figure 13. Radiation Shield of Pt-10Rh.

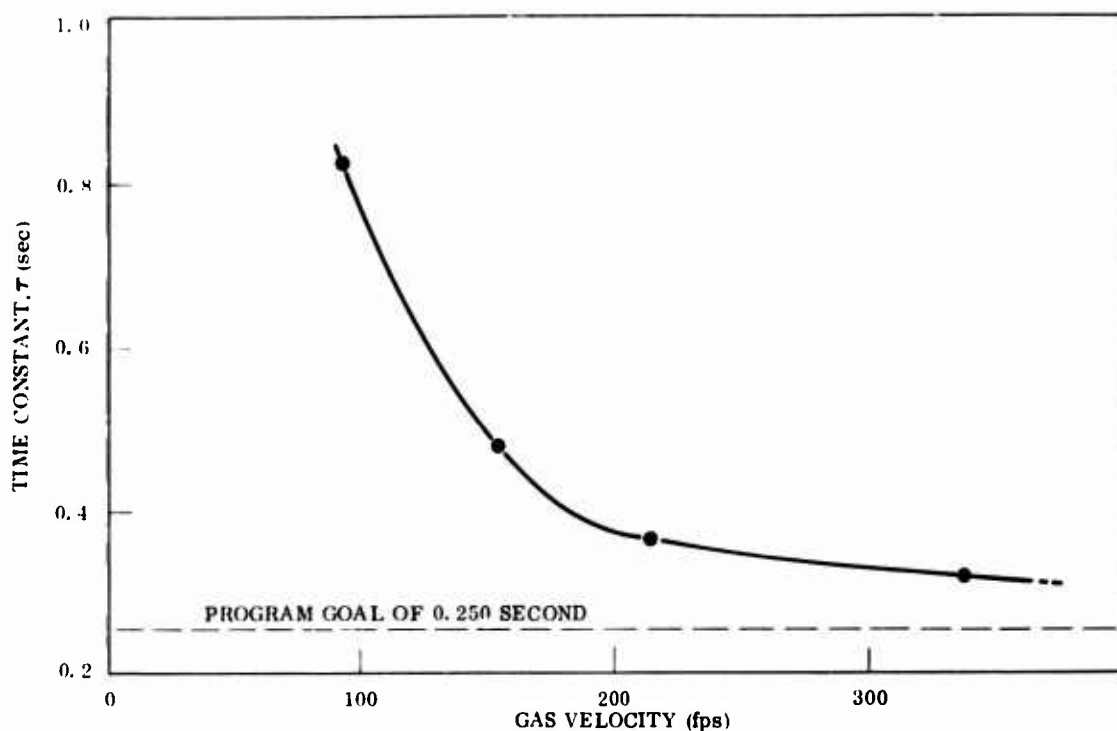


Figure 14. Time Constant Versus Gas Velocity for a Shielded Thermocouple.

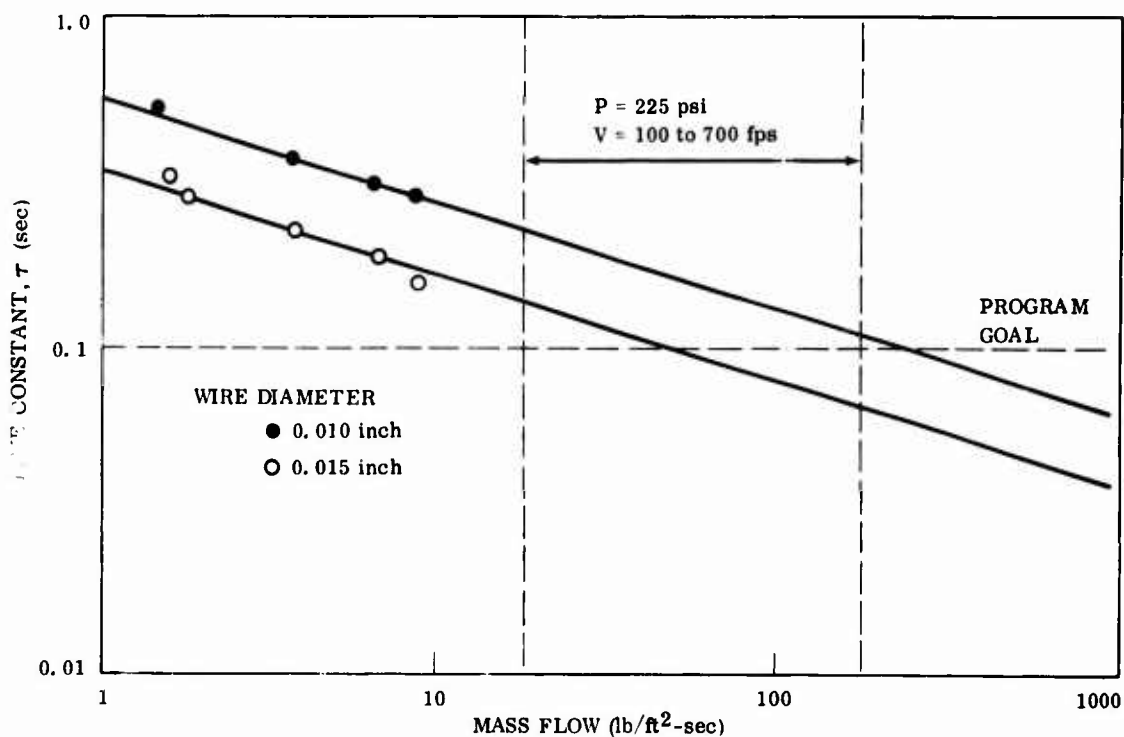


Figure 15. Time Constant Versus Mass Flow for an Exposed Single-Junction Thermocouple.

700 fps at 775 psia are indicated as typical for the specified program conditions. The slope of the experimental data agrees with the calculated slope quite well, although the absolute value was higher than calculated.

A multijunction of 0.010-inch-diameter wire was then tested in the same shield and compared to an exposed multijunction (Ref. 3, p. 62). The additive junctions were fusion welded and paired to reduce the bead size with respect to the bushing junction. The overall response shown in Figure 16 reaches the program goal for a shielded thermocouple at about 10 lb/ft<sup>2</sup>-sec mass flow.

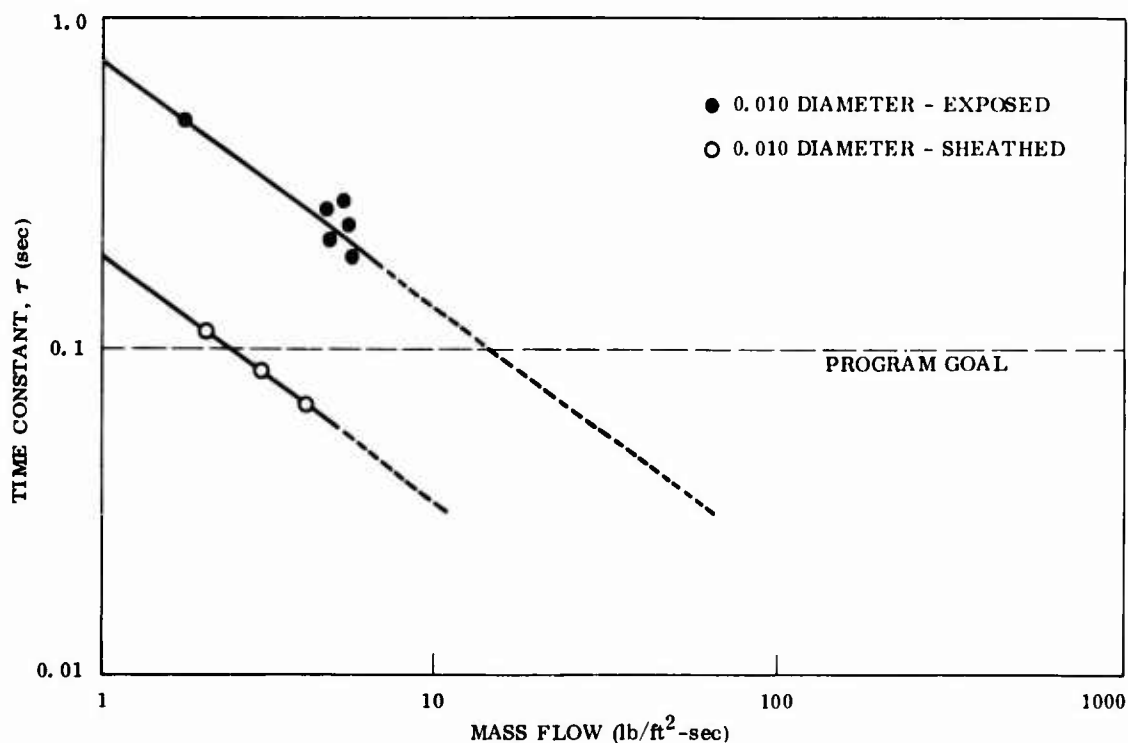


Figure 16. Time Constant Versus Mass Flow for a Multijunction Thermocouple.

## LONG-LIFE THERMOCOUPLE DESIGN AND FABRICATION

### Design and Materials Selection

The choice of materials for use at 2500°F (1371°C) with excursions as high as 2800°F (1538°C) is limited. In addition to high temperatures, the materials must withstand thermal shock, large thermal gradients, oxidation, a carburizing atmosphere, possible erosion, and vibrational and aerodynamic loadings. Design for thermocouple performance requires small sections, good heat transfer characteristics, and stable thermoelectric properties. The long-life thermocouple described in this report is designed to use advanced technology for fabrication of available

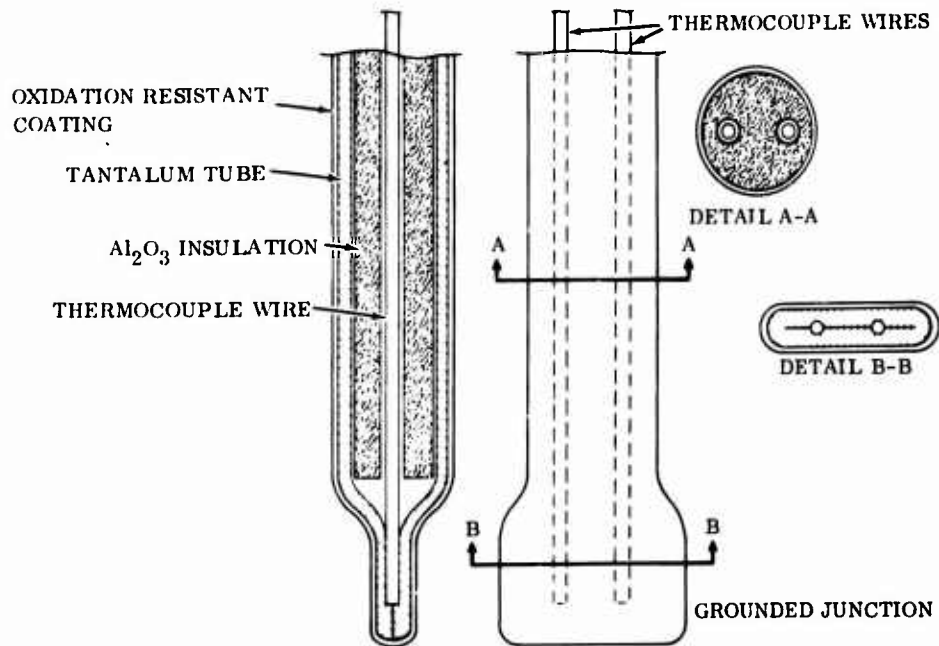


Figure 17. Design for a Long-Life Thermocouple.

materials into a system that provides an optimum combination of ruggedness, fast response, and long life.

To provide protection from contamination and mechanical damage, the thermocouple junction is enclosed inside a protection tube. To optimize response, the junction is grounded (connected electrically and thermally) to the tube. Grounding the junction minimizes the heat flow path from the gas to the junction, thus minimizing response rate (Figure 17). The protection tube culminates in a flattened tip into which the thermocouples are bonded. Minimum flow blockage and optimum heat transfer characteristics occur when the tip is oriented with its flat surface parallel to the flow (Figure 18A) rather than perpendicular (Figure 18B). The smooth flow around the tip (Figure 18A) reduces the thickness of the boundary layer to a minimum, and thus maximizes the heat transfer from the free-flowing gas to the thermocouple tip.

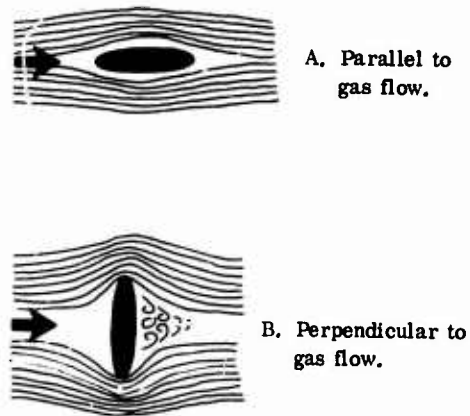


Figure 18. Probe Tip Parallel (A) and Perpendicular (B) to Gas Flow.

Tantalum was chosen for the protection tube because of its unusual combination of properties. It offers a high-temperature capability, a melting point of 5425°F (2996°C), excellent fabricability at room temperature, and availability of a coating for high-temperature oxidation resistance. The coating (Ref. 18) is a duplex silicide coating in which a modifier alloy is slurry applied and vacuum sintered onto the tantalum substrate preparatory to siliciding. Tungsten-rhenium alloys provide one of the most stable refractory metal systems for high-temperature measurement. The principal problem associated with use of this alloy system has been the recrystallization and embrittlement of the low-rhenium alloy during fabrication. This problem has been particularly true of thermocouples using pure tungsten as one element and has been partially overcome by the W-3Re alloy. This alloy is prepared by doping with alkaline earths during preparation of the wire (Ref. 19). The doping agents are volatile and are eliminated during processing. The resulting microstructure is preferentially oriented in the axial direction with grain boundaries at small angles to the wire axis. After recrystallization, the wire retains a much higher ductility than pure tungsten.

Tungsten-rhenium thermocouples have proven to be very stable in high-purity alumina,  $\text{Al}_2\text{O}_3$ , insulators up to 3272°F (1800°C) (Ref. 20). Alumina is also the most readily available insulator in a wide variety of shapes and sizes.

The cold end of the protection tube is sealed with epoxy to maintain the W-Re wires in an inert atmosphere. Lead wires (Engelhard Alloy 300P and 300N) are used which compensate for temperatures up to 626°F (330°C) within a tolerance of  $\pm 0.125$  millivolt (Ref. 21).

### Fabrication

Basic steps in fabricating the long-life thermocouple are:

1. Cold forming
2. Diffusion bonding
3. Coating
4. Sealing and finishing

The tubes and wires are first cut to size, the tubes are annealed in vacuum, and all parts are degreased and kept clean. The wires are then positioned in the tube, and the flattened tip is formed around the wires by pressing between two anvils. Figure 19 shows three views of the cold-formed tip. The tantalum flows around the much harder tungsten wires and completely envelopes them. The anvils are shaped to give a gradual transition from the flattened tip to the round shank. Cold-formed junctions are then diffusion bonded in an inert atmosphere. Bonding



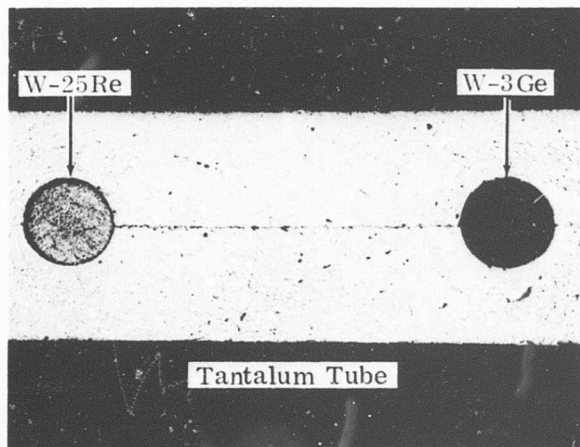
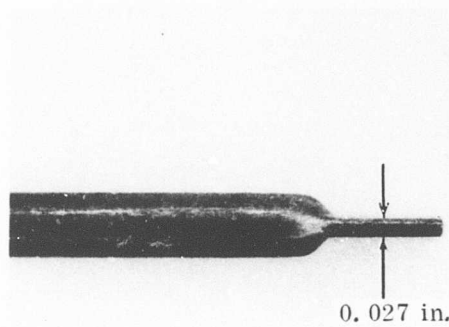
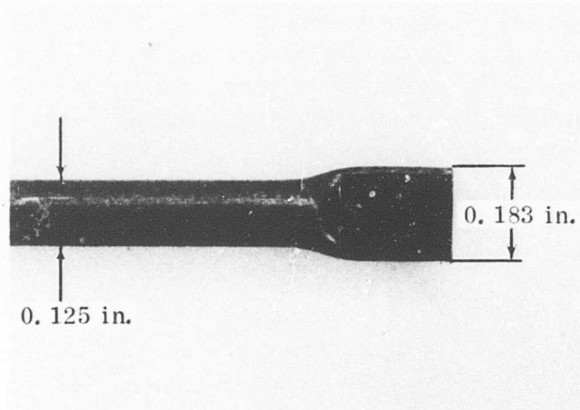


Figure 19. Cold-Formed Tip of Long-Life Probe.

consists of resistance heating the tip of the thermocouple under pressure between two anvils. Grain growth by diffusion across the bond line produces complete bonding (Figure 20). After bonding, the tip is radiused to eliminate high stress concentrations during thermal shock conditions. The opposite end of the probe is also sealed to protect the W-Re wires during the coating cycle. Approximately two inches of the tube is left uncoated and is removed after the coating cycle to allow the W-Re wires to project from the coated protection tube. Alumina insulation is inserted, and the end of the tube is sealed with epoxy in an inert atmosphere. Lead wires are welded to the thermoelements, and insulation is added around the probes to finish the assembly.

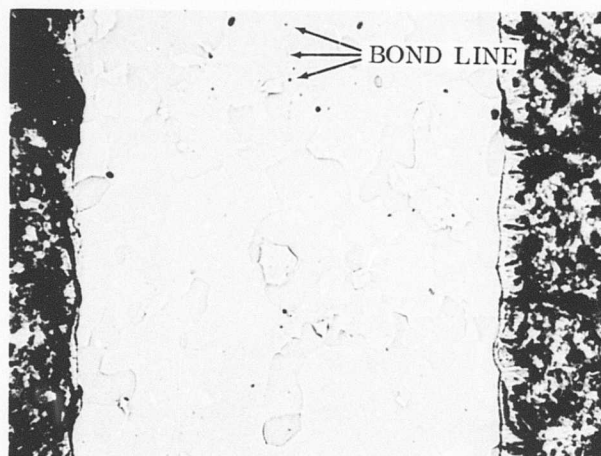


Figure 20. Bonded Long-Life Probe.

Early efforts to fabricate the long-life thermocouple were hampered by brittleness of the W-Re wires. This brittleness was overcome by careful attention to cleanliness and vacuum level. All parts were degreased and handled with white gloves. Slight oxygen contamination diminishes bend ductility considerably. As bonding methods improved, bend ductility improved and the wires could be bent around a 0.125-inch-diameter mandrel for several turns without breaking.

### Testing and Performance

#### Coating Durability

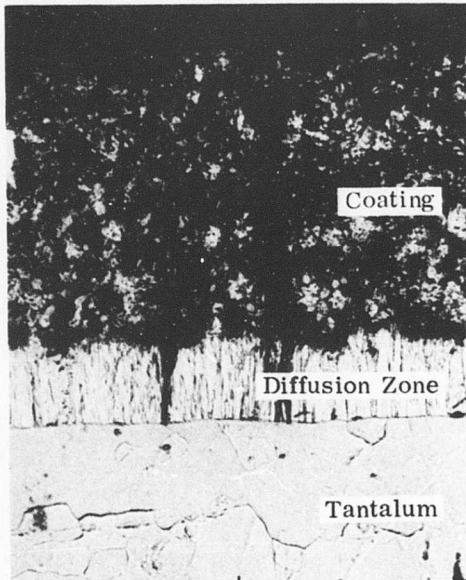
Samples of tantalum were coated and exposed to high temperatures in electrically heated furnaces in still air to test for oxidation resistance and the effect of substrate thickness and edge radius. Samples 1.0 inch long by 0.125 inch wide by 0.010, 0.020, 0.030, and 0.040 inch thick were coated with a

0.010-inch-thick coating of TNV-7. The ends of the samples were rounded and the edges were radiused. The samples were supported across dynaquartz triangles which were placed on high-temperature bricks in the furnace. The end of the furnace muffle was left partially open to allow air circulation. Samples were removed periodically for inspection. Ten samples of each thickness were exposed at each of the following temperatures: 1800°, 2100°, and 2550° F. Testing was terminated after 300 hours without a single failure. It was concluded that the thermocouple tip could be made as thin as 0.010 inch without causing a problem with the coating. Figure 21 shows a photomicrograph of an as-coated sample and an exposed sample at each of the three temperatures. The coating is porous and consists of metal disilicides. Under the coating is a diffusion layer of  $Ta_3Si_5$  and finally the base metal. The porosity allows for thermal expansion and contraction. As long as the cracks do not penetrate the diffusion layer, oxidation of the tantalum does not occur. Eight samples tested at 1800° F for 300 hours were placed in a holder (Figure 22) and immersed in moving hydrocarbon combustion products at 1800° F and 200 fps. A failure occurred after 36 additional hours at the cooler end of one of the samples. Photomicrographs at the failed end (Figure 23A) show that penetration of the diffusion layer by cracks and oxidation is occurring in the tantalum substrate. Figure 23B shows the hot, unfailed end of the same sample. The cracks stop at the diffusion layer. This phase of the oxidation testing was discontinued in favor of actual thermal cycling of complete thermocouple probes.

#### Temperature Cycle Testing

A temperature cycle control was combined with the moving gas tester shown in Figure 4. The controller consisted of a cam timer and solenoid valves in the gas and oxygen lines. The timer also operated an air cylinder (Figure 24) which inserted and retracted the probes from the moving gas stream. Cool air was directed at the probes for rapid cooling when they were retracted from the hot gas stream. Each cycle (Figure 7) consisted of the probe's being inserted into the moving gas stream at 1800° F and remaining there for 16 minutes; then the gas temperature was raised to 2200° F and maintained for 9 minutes; then it was raised again to 2500° F for 6 minutes. The probe was then removed and cooled while the gas temperature returned to 1800° F for the next cycle. Up to four probes were cycled at a time.

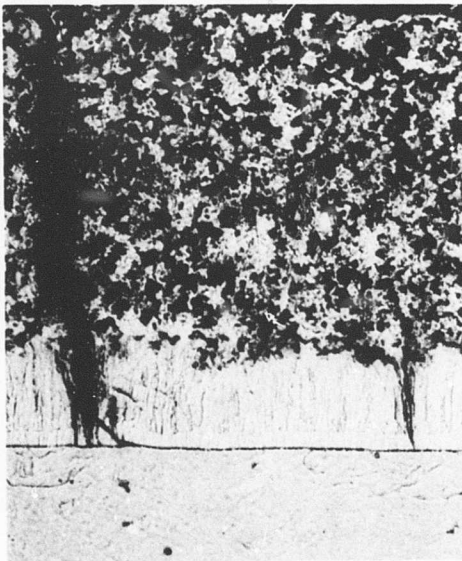
Effect of fabrication and cycling on the microstructure of the tantalum tip and W-Re wires is shown in Figure 25. Large amounts of grain growth have occurred in the W-25Re wire and some in W-3Re wire; however, the W-25Re wire still retains superior ductility. The bond line is marked with a series of voids, but bonding is complete.



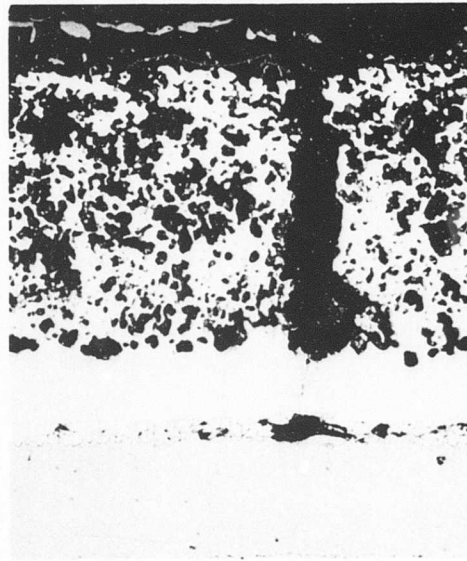
As Coated  
Magnification: 250X



1800°F  
300 Hours  
Magnification: 250X



2100°F  
307 Hours  
Magnification: 250X



2550°F  
300 Hours  
Magnification: 200X

Figure 21. Microstructure of the TNV-7 Coating.

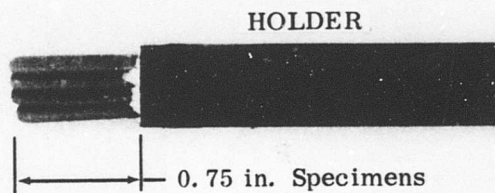
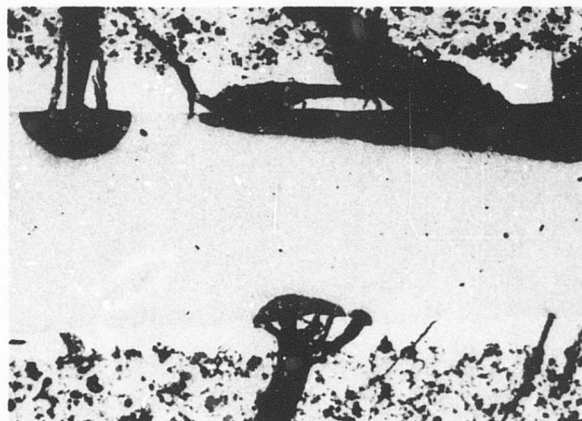


Figure 22. Test Specimens for Oxidation Tests in Moving Gas.



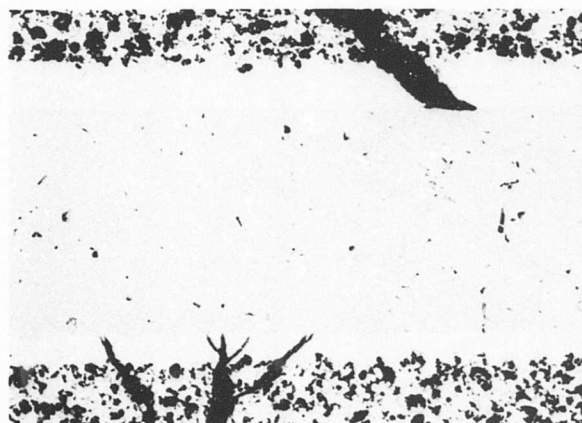
A. Failed End

Tantalum

Diffusion Zone

Coating

Magnification: 150X



B. Non-Failed End

Tantalum

Diffusion Zone

Coating

Magnification: 150X

Figure 23. Cross Section of Failed Test Specimen.



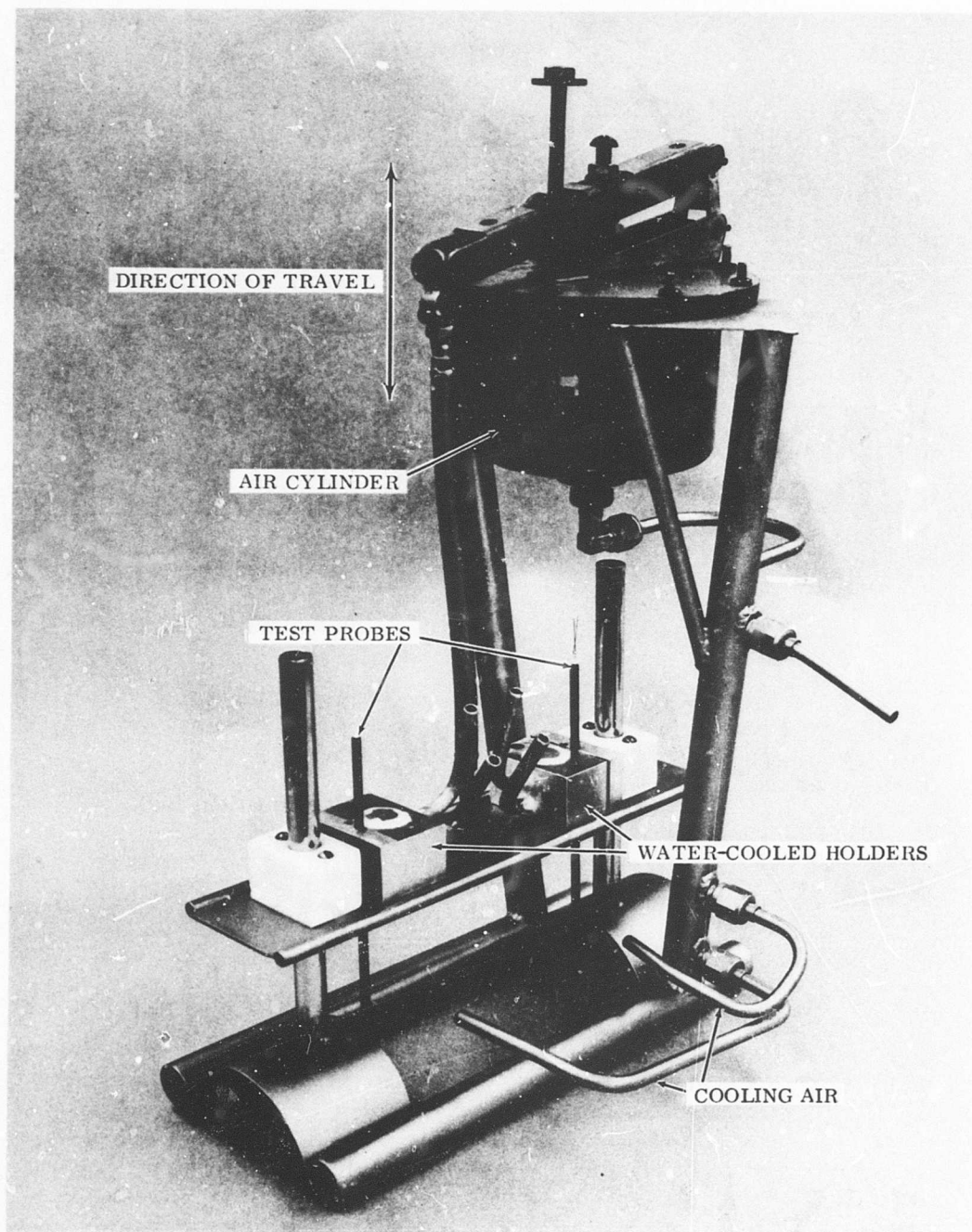


Figure 24. Apparatus To Cycle Probes Into Moving Gas Streams.

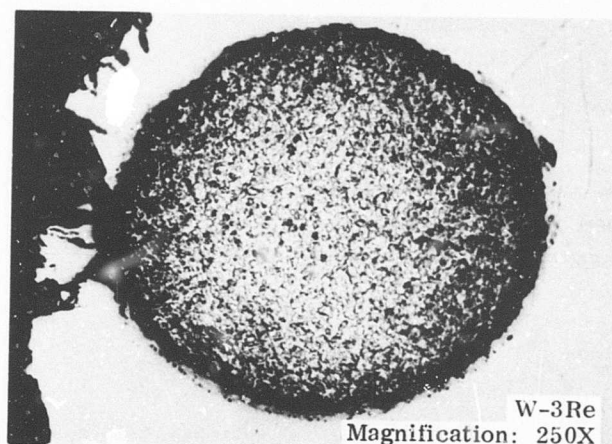
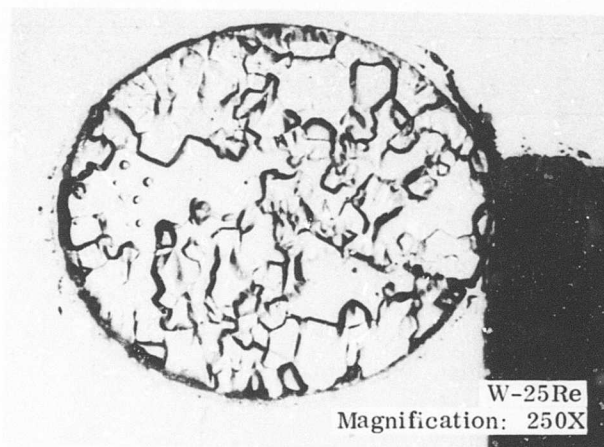


Figure 25. W-Re Wires After 47 Hours of Exposure.

Sixteen probes were tested for endurance in the thermal cycle environment. Table VI shows the hours to failure for each probe. Coating thickness is also indicated. The limiting mechanism was coating life. A typical failure is shown in Figure 26. In all cases where thermocouple output was recorded, the reading remained steady until failure occurred. The short-term failures were attributed to quality control problems, especially with the thick coatings. Slight modifications of the coating will probably extend the life of the coating by an order of magnitude or more. The most severe environmental condition is imposed by the thermal shock caused by very rapid heating and cooling during each cycle.

TABLE VI. THERMAL CYCLE TESTING			
Probe Number	Coating Thickness	Hours to Failure	Cycles to Failure
1	Thin (0.0035 in.)	31	57
2	Thin	47	85
3	-	62	113
4	-	118	212
5	Medium (0.005 in.)	4	7.3
6	Medium	35	64
7	-	69	118
8	Thick (0.007 in.)	5	9
9	Thick	10	18
10	Thick	2	3.6
11	Thin	109	198
12	Medium	115	209
13	Medium	68	124
14	Medium	81	147
15	Medium	62*	113
16	Thin	15*	27

\* Testing stopped before failure.

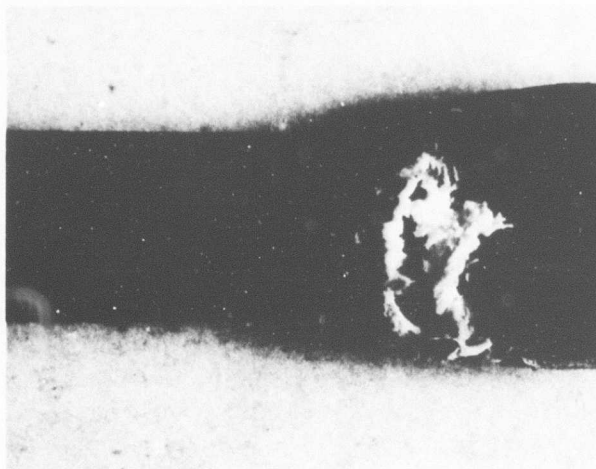


Figure 26. Typical Coating Failure.



## Response

The response rate of the long-life thermocouple was tested in moving gas at various velocities in the same manner as the fast-response thermocouple. The time constant for typical tests on a medium-thickness coating (0.005 inch) is shown as a function of gas velocity in Figure 27. Data are shown in Figure 28 for all three coatings extended to high mass flows by the use of equation (9). Response was measured at a gas temperature of 2000° F. The time constants approach the program goal of 750 milliseconds at mass flows of approximately 20 lb/ft<sup>2</sup>-sec, well within the ranges of flow typical of a small, high-performance gas turbine engine. While coating thickness has a definite effect on response time, this difference assumes less importance when the data are extended to high flow rate. The coating can be optimized for endurance within the range of thickness tested without overly affecting response rates.

The time constant of thin and thick probes was tested as a function of tip orientation and gas velocity (Figure 29). The probes responded faster when they were parallel than when they were at 45 and 90 degrees to the flow. The difference was of the order of 150 milliseconds. The stagnant area built up in front of a plate immersed perpendicular to the flow would impede heat transfer from the gas to the probe and raise the time constant compared to the parallel orientation.

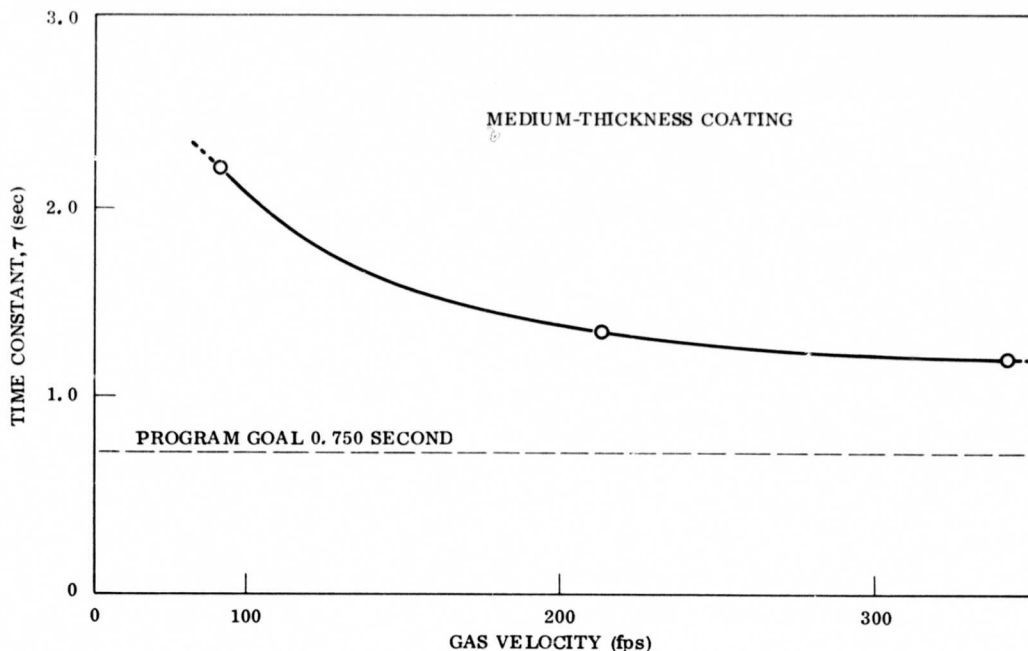


Figure 27. Time Constant of a Long-Life Thermocouple Versus Gas Velocity.

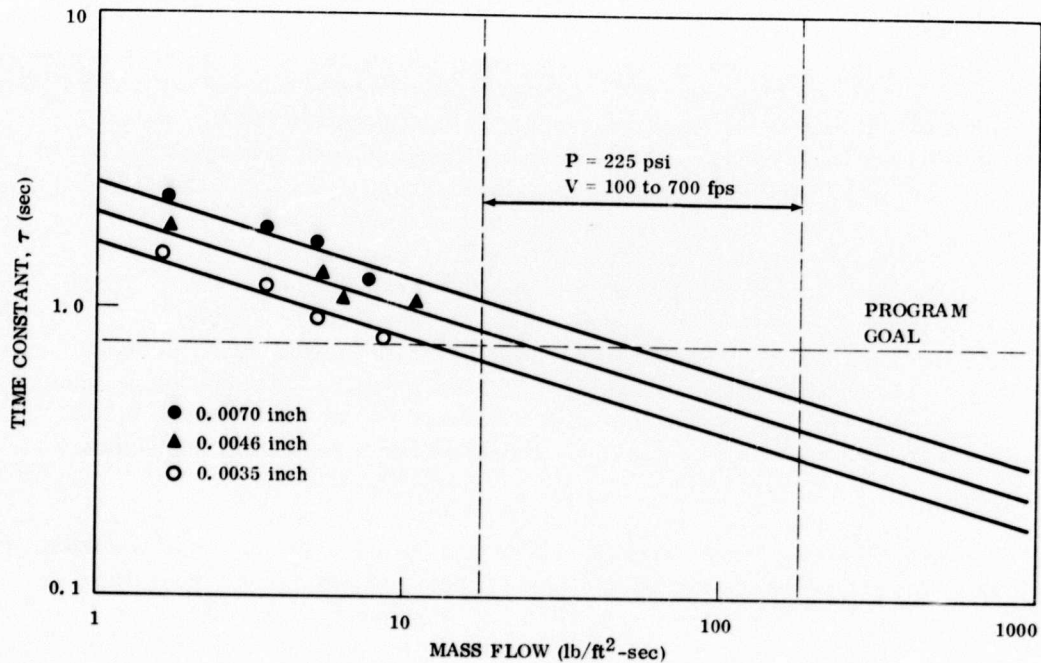


Figure 28. Time Constant of a Long-Life Thermocouple Versus Mass Flow.

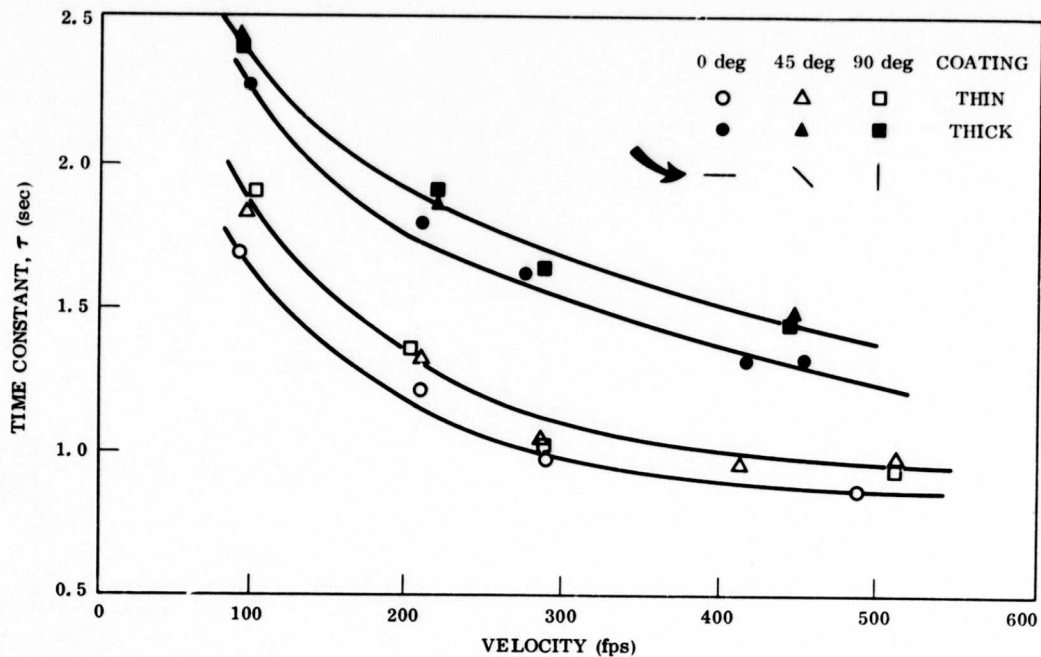


Figure 29. Time Constants for Three Tip Orientations.

### Calibration and Accuracy

A long-life probe was calibrated in an electric furnace against a Pt versus Pt-13Rh thermocouple. The bare Pt-Rh thermocouple was in contact with the spade of the probe. The readings were compared at temperatures between 1800° and 2100°F. Table VII contains the results of the test.

TABLE VII. CALIBRATION OF A LONG-LIFE PROBE		
Temperature (°F)		Temperature Difference (°F) (Pt-Rh)-(W-Re)
Pt-Rh	W-Re	
1753	1751	-2
1794	1793	-1
1911	1912	+1
1916	1917	+1
2004	2003	+1
2098	2102	+4
2104	2107	+3

No degradation of the thermocouple accuracy during fabrication was detected. The probe failed as a result of contact with the platinum thermocouple. Platinum forms a low melting eutectic (1526°F, 830°C) with the silicon in the coating causing failure.

### CONCLUSIONS AND RECOMMENDATIONS

#### Fast-Response Thermocouple

Platinum-rhodium has been shown to be the only thermoelectric alloy system able to function as an exposed thermocouple in a high-temperature oxidizing environment. The Pt-6Rh versus Pt-30Rh thermocouple is the most stable of the several Pt-Rh alloys available. Alumina,  $\text{Al}_2\text{O}_3$ , is the most satisfactory insulator for temperature less than 2500°F. A shield to reduce the radiation error and to control the local velocity at the thermocouple junction is necessary for accurate performance at the turbine inlet. A multiple in-series junction was used to lower the time constant of the thermocouple to less than 100 milliseconds. More than 100 hours were accumulated in a severe thermal cycle environment without failure. This

thermocouple is judged to be suitable for accurate temperature measurement in engine development and testing programs. Two fast-response multiple-junction probes were fabricated to the dimensions shown in Figure 30 and delivered to the U. S. Army for further evaluation and study.

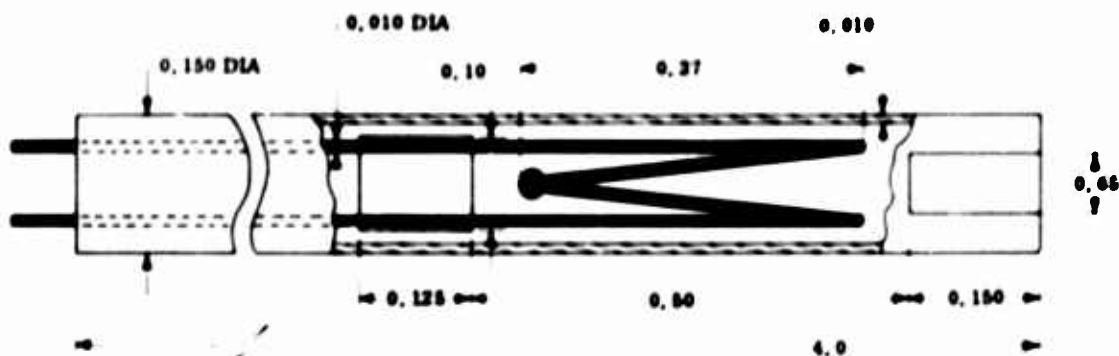


Figure 30. Fast-Response Thermocouple.

#### Long-Life Thermocouple

The long-life design demonstrated that a protected thermocouple can also provide fast response and ruggedness compatible with gas turbine requirements. The program goal of time constant was reached at mass flows typical of a gas turbine inlet. Diffusion bonding and a Solar-developed coating for refractory metals allow the W-Re thermoelements to be grounded to a flattened-tip, tantalum protection tube by diffusion bonding techniques.

Development of this thermocouple design is in progress to reach the materials system capability of 2000 hours at 2500°F. This goal represents an improvement over the verified 300 hours at 2500°F. Extension of the engine stop-start thermal transient from the tested 200 cycles to the goal of 600 stop-start cycles is also in progress. Continued evaluation of this design is in order to define its performance and reliability in turbine engine environments as well as development of the design from the experimental to the prototype and production stages. Four probes were fabricated to the dimensions shown in Figure 31 and shipped to the U. S. Army for evaluation.

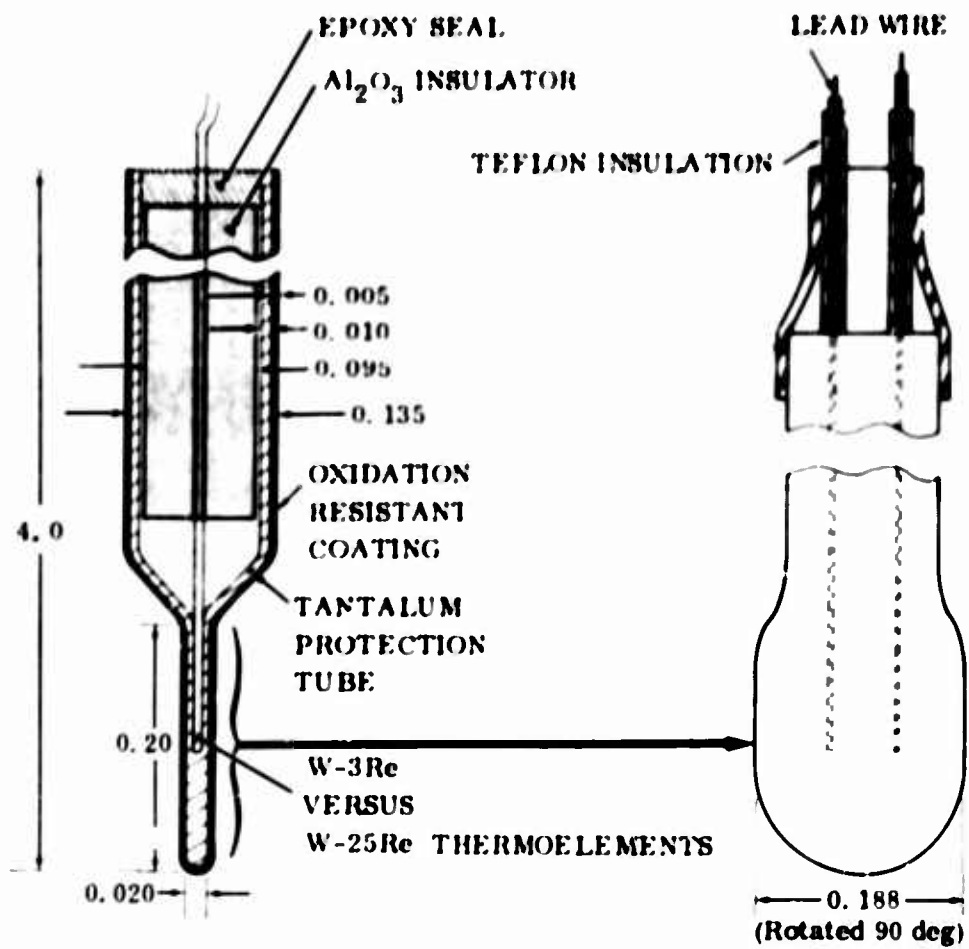


Figure 31. Long-Life Thermocouple.

## RADIATION SENSOR

### DESIGN OF A RADIATION SENSOR FOR A TURBINE ENGINE

#### Radiation Equations

All matter emits radiant energy to its surroundings as a function of temperature. This radiation may come from solids, liquids, or gases. Solids and liquids radiate at all wavelengths; the amount of power radiated at each wavelength is a function of temperature and the surface conditions of the emitting body. A perfect emitter, called a blackbody, absorbs all radiation incident upon its surface. All real surfaces radiate a lesser amount of energy at all wavelengths. The ratio between blackbody radiation, for which mathematical treatment is available, and the radiation from a real surface is called the emittance.

Radiance (watts/cm<sup>2</sup>) from a blackbody,  $N_{b\lambda}$ , is given by the Planck function.

$$N_{b\lambda} = C_1 \lambda^{-5} \left( \exp(C_2 / \lambda T) - 1 \right)^{-1} \quad (10)$$

where  $N_{b\lambda}$  = blackbody radiance (radiant power) emitted at wavelength  $\lambda$

$T$  = temperature of a solid body (°K)

$\lambda$  = wavelength (cm)

$C_1$  = constant =  $3.7412 \times 10^{-12}$  watt cm<sup>2</sup>

$C_2$  = constant = 1.4388 cm °K

Radiance from a real surface  $N_\lambda$  is found by multiplying  $N_{b\lambda}$  by the emittance,  $\epsilon_\lambda$ , which is a function of wavelength and is less than one. For the purposes of this report, emissivity is considered a property of the material from which the radiating body is made, while emittance is a property of the material, surface roughness, and degree of oxidation. A plot of the dependence of radiant power on wavelength for a blackbody ( $\epsilon_\lambda = 1$  for all  $\lambda$ ) is shown in Figure 32 for several temperatures. The radiant power emitted at all wavelengths increases with increasing



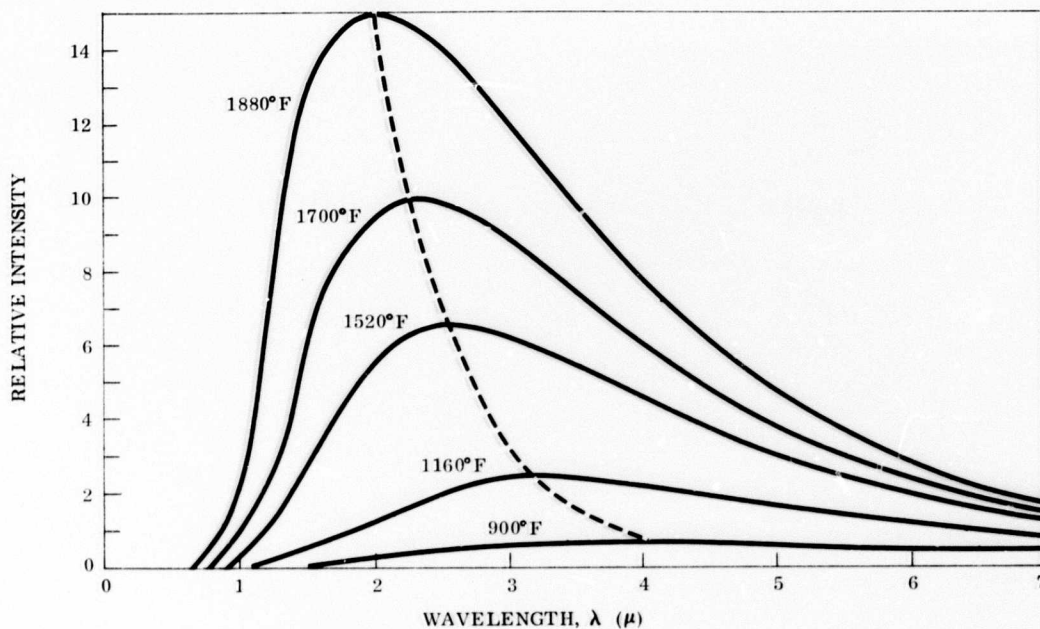


Figure 32. Blackbody Radiation.

temperature. There is a wavelength at which the radiant power is a maximum, and this maximum occurs at lower wavelengths as the temperature increases, according to Wien's displacement law

$$\lambda_{\max} T = 2897 \text{ microns } ^\circ\text{K} \quad (11)$$

where  $\lambda_{\max}$  = wavelength for maximum radiance (microns)

$T$  = temperature ( $^\circ\text{K}$ )

The total amount of energy radiated at all wavelengths increases as the fourth power of temperature according to the Stefan-Boltzmann law:

$$N_{\text{total}} = \epsilon_{0-\infty} \sigma T^4 \quad (12)$$

where  $\sigma$  = Stefan-Boltzmann constant =  $5.699 \times 10^{-12} \text{ watts cm}^{-2} \text{ } ^\circ\text{K}^{-1}$

$\epsilon_{0-\infty}$  = total emittance

The Planck function is difficult to handle mathematically, and Wien's equation is within one percent of the Planck function for all conditions where  $\lambda T \leq 3000$  microns  $^\circ\text{K}$ .

Wein's equation is given by

$$N_{b\lambda} = C_1 \lambda^{-5} (\exp C_2/\lambda T)^{-1} \quad (13)$$

The spectral radiation  $N_{b\lambda_1 - \lambda_2}$  emitted over a range of wavelengths from  $\lambda_1$  to  $\lambda_2$  is given by

$$N_{b\lambda_1 - \lambda_2} = \int_{\lambda_1}^{\lambda_2} N_{b\lambda} d\lambda \quad (14)$$

where  $N_{b\lambda}$  is given by Planck's equation.

This integral is laborious, but reference to tables, nomographs, and calculators is possible.  $N_{b0-\lambda}$  and  $N_{b0-\infty}$  are available for all  $\lambda$ , and the equation may be written

$$N_{b\lambda_1 - \lambda_2} = \left( \frac{N_{b0-\lambda_2}}{N_{b0-\infty}} - \frac{N_{b0-\lambda_1}}{N_{b0-\infty}} \right) \left( \frac{N_{b0-\infty}}{1} \right) \quad (15)$$

With  $\lambda_2$  and  $\lambda_1$  as the upper and lower limits of the spectral sensitivity of a detector,  $N_{b\lambda_1 - \lambda_2}$  gives the total hemispherical radiation/unit area leaving the target within its spectral sensitivity.

Performance of the optical system can be partially described by the transfer factor (Ref. 22) ( $F_t$ ), which is the ratio of radiant power ( $\phi$ ) arriving at the detector surface to the radiant power, within the range  $\lambda_1$  to  $\lambda_2$ , leaving the target.

$$F_t = \phi / \epsilon_\lambda N_{b\lambda_1 - \lambda_2} \quad (16)$$

$\epsilon_\lambda$  = emittance of the target

For a schematic optical system (Figure 33), the transfer factor is given by

$$F_t = A_o A (1 - \beta)^\nu (\gamma_j) / \pi D^2 \quad (17)$$



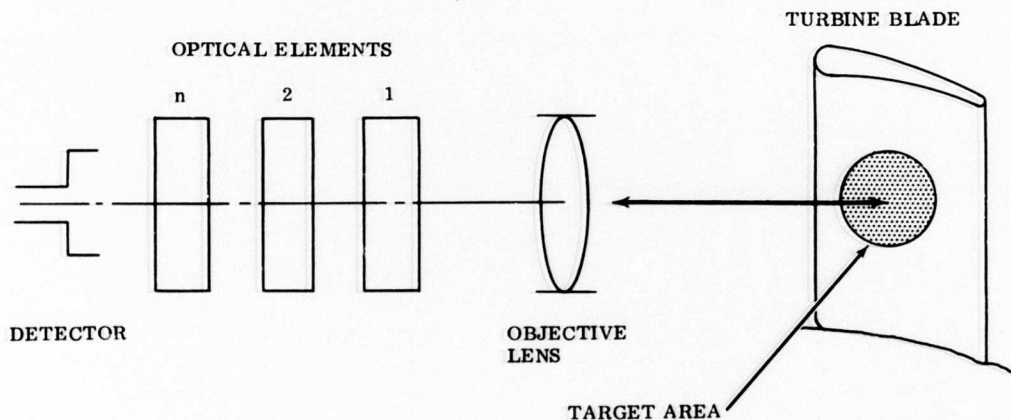


Figure 33. Schematic Optical System.

where  $A_o$  = area of objective lens (in.<sup>2</sup>)

$A$  = area of the target (in.<sup>2</sup>)

$\beta$  = coefficient of reflection

$\nu$  = total number of air-glass interfaces

$\gamma_j$  = fraction of signal transmitted by optical element,  $j$

$D$  = distance from objective lens to target (in.)

The optical axis is assumed to be perpendicular to the target surface.

The signal produced by the detector is proportional to the radiance arriving at its surface within its spectral range. The proportionality constant,  $R_\lambda$  (amps watts<sup>-1</sup>), is called responsivity and the detector signal,  $S$  (amps), is then given by

$$S = R_\lambda \epsilon_\lambda F_t N_b \lambda_1 - \lambda_2 \quad (18)$$

for a detector sensitive from  $\lambda_1$  to  $\lambda_2$ .

Total radiation pyrometers are ideally responsive to all wavelengths. Brightness or spectral pyrometers are responsive to a single or narrow band of wavelengths.

Solid-state photovoltaic and photoconductive diodes, photo-transistors, and photo-multiplier tubes provide brightness pyrometers sensitive to a wide range of wavelengths.

Silicon is the most adaptable detector material currently available to form the basis for a radiation sensor for turbine engine application (Ref. 3). Silicon has a peak responsivity near 0.85 micron and accepts radiation to a lesser degree from approximately 0.4 to 1.1 microns. The approximate radiant power available to a silicon detector is listed in Table VIII for a range of temperatures.

TABLE VIII. APPROXIMATE RADIANT POWER/UNIT AREA			
Temperature		Total Radiation (watts/in. <sup>2</sup> )	Spectral Radiation 0.4 to 1.1 Microns (watts/in. <sup>2</sup> )
(°F)	(°C)		
1000	538	16	1.3 x 10 <sup>-3</sup>
1200	649	27	1.1 x 10 <sup>-4</sup>
1400	760	42	4.6 x 10 <sup>-2</sup>
1600	871	65	2.1 x 10 <sup>-1</sup>
1800	982	92	7.3 x 10 <sup>-1</sup>
2000	1093	130	1.8
2500	1371	270	11.0
3000	1649	300	45.0

The spectral radiation shown in Table VIII can be used in equation (16) to find the power incident at the detector. This spectral radiation, in turn, may be used to predict the signal out of the detector for a given target, temperature, and optical system.

Many properties of radiation pyrometers may be more easily analyzed by an exponential equation of the type (Ref. 23)

$$N_{b\lambda} = KT^{n(\lambda T)} \tag{19}$$

where K is a constant.

Using the Wien equation,  $n$  is found to be equal to

$$n = C_2/\lambda T \quad (20)$$

The exponent,  $n$ , is plotted against temperature in Figure 34 for several wavelengths. Over the range of temperatures of interest, the temperature exponent is very high. This property produces a sensor with high inherent accuracy and sensitivity and with little error resulting from unknown or changing emittance.

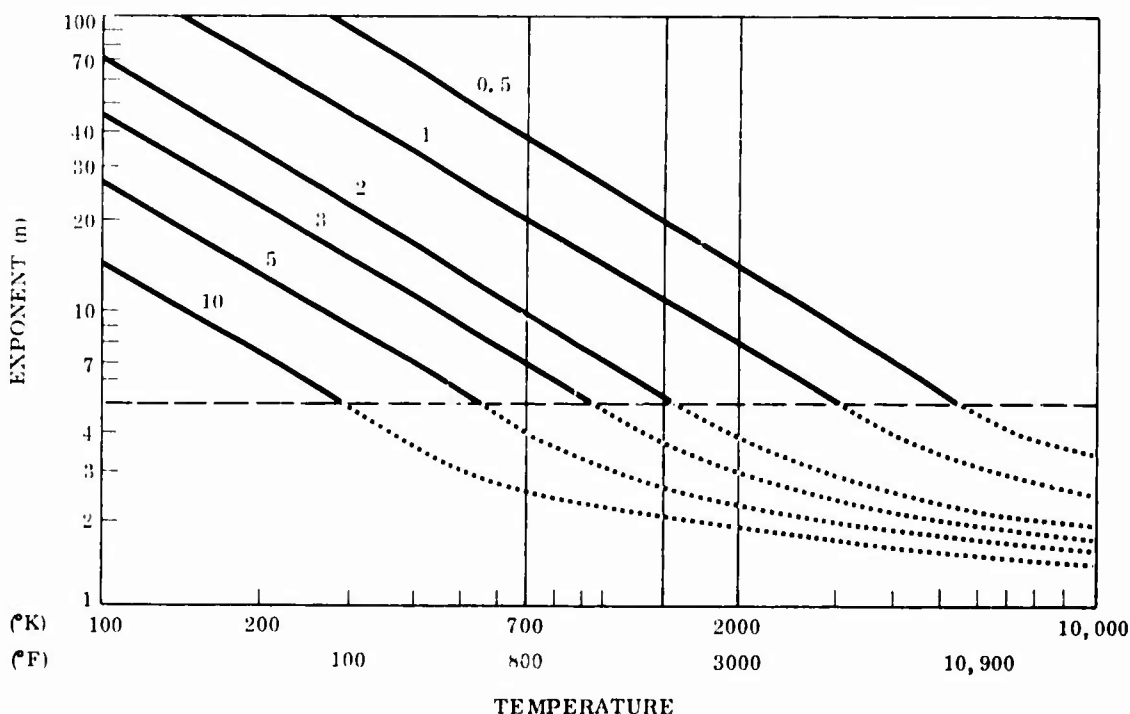


Figure 34. Temperature Exponent.

Sensitivity is a measure of how small a variation in temperature can be measured by a pyrometer. Differentiating equations (18) and (19) with respect to temperature will derive an equation for the fractional change in signal/unit change in temperature.

$$\frac{dS/dT}{S} = nT^{-1} = \frac{C_2}{\lambda T^2} \quad (21)$$

Sensitivity is directly proportional to the value of  $n$ . For detectors that are responsive to a narrow band of wavelengths, an effective wavelength may be calculated to allow the use of the formulas derived for monochromatic radiation (Ref. 24). Table IX shows the effective wavelength for silicon (Ref. 25), the temperature exponent,  $n$ , and the calculated sensitivity for silicon detectors.

TABLE IX. DATA FOR SILICON DETECTORS				
Temperature		Effective Wavelength (micron)	Temperature Exponent (T in °K)	Sensitivity (%/°F)
(°F)	(°C)			
932	500	0.98	19.0	2.5
1832	1000	0.91	12.4	1.0
2732	1500	0.86	9.6	0.5

Detectors with high values of n are also insensitive to changes or uncertainties in emittance or optical transfer factor. A pyrometer is calibrated at certain conditions, namely,  $\epsilon_c$  and  $F_{tc}$ . If in use the emittance,  $\epsilon$ , and transfer factor,  $F_t$ , are not equal to their calibration values, then there will be a temperature error. The true temperature, T, is related to the indicated temperature,  $T_i$ , by

$$T = \left(\frac{\epsilon_c}{\epsilon}\right)^{1/n} \left(\frac{F_{tc}}{F_t}\right)^{1/n} T_i \tag{22}$$

If  $\epsilon = \epsilon_c$  and  $F_t = F_{tc}$ , the true temperature will equal the indicated temperature and there is no error. If, for example, the ratio  $\epsilon_c/\epsilon \neq 1$ , then  $T_i$  will be in error by a factor of  $(\sqrt[n]{\epsilon_c/\epsilon} - 1)$ . Table X gives values of the temperature error for several ratios and exponents.

TABLE X. EMISSIVITY ERRORS FOR SPECTRAL RADIATION SENSORS				
$\epsilon_c/\epsilon$	Temperature Error (% of $T_i$ )			Remarks
	n = 4	n = 10	n = 20	
0.8	5.4	2.2	1.2	$T < T_i$
0.9	2.6	1.1	0.6	$T < T_i$
1.0	0	0	0	$T = T_i$
1.1	2.4	1.0	0.5	$T > T_i$
1.2	4.7	1.8	0.9	$T > T_i$
1.3	6.8	2.7	1.3	$T > T_i$

For a given ratio (emissivity error), the temperature error decreases as  $n$  decreases. For a total radiation pyrometer,  $n$  is equal to 4. Ten is a typical exponent for silicon, and 20 is typical for an ultraviolet detector. The column for  $n = 10$  shows that a 10-percent change in emittance causes a 1.1-percent temperature error.

### Turbine Environment

The temperature of the first-stage turbine blades is measured by the radiation sensor. First-stage blades were chosen as the target because of their critical nature, high temperature, and high stress. A portion of the blade is selected and its surface temperature is measured. The shape of the blade, geometrical relationship between blade and sensor, ambient conditions surrounding the blade, and ambient conditions of the sensor all affect the design and performance of the transducer. To be effective, the sensor must be insensitive to changes in environment and be able to function over the entire range of conditions encountered in a military application.

The target blades are immersed in hydrocarbon combustion products at temperatures up to 2800°F as well as radiation from the flame and other hot parts. A silicon detector avoids radiation and adsorption directly by the gas because its spectral range is at lower wavelengths than those for the various constituents of the gas. The relative magnitude of the radiation from the gas and a blackbody are shown as a function of wavelength in Figure 35 and are compared to the spectral sensitivity of silicon. However, radiation from the flame is continuous, and there is no spectral range that can be chosen to avoid it. Radiation from the flame is reflected from the blades and other hardware, and when detected by the sensor, it will produce an extraneous signal. Incandescent soot particles entrained in the moving gas also emit energy that will be picked up by the sensor while the particles are in the sensor's field of view.

The shape of the target also affects performance, as does the angle of the optical axis with the target surface. The emittance of the target surface is a function of the material, its state of oxidation, its surface roughness, and the direction in which it is measured. After initial oxidation, the emittance of common blade materials is relatively high and will not change appreciably during use. The direction must be considered, especially if it is at a large angle from the surface normal. The sensor must interface with an environment of hydrocarbon combustion products and maintain a clear optical path between the target and the detector. The turbine case upon which the sensor is mounted may be at a temperature as high as 1200°F. The sensor optics must be protected from contamination, and the detector must be

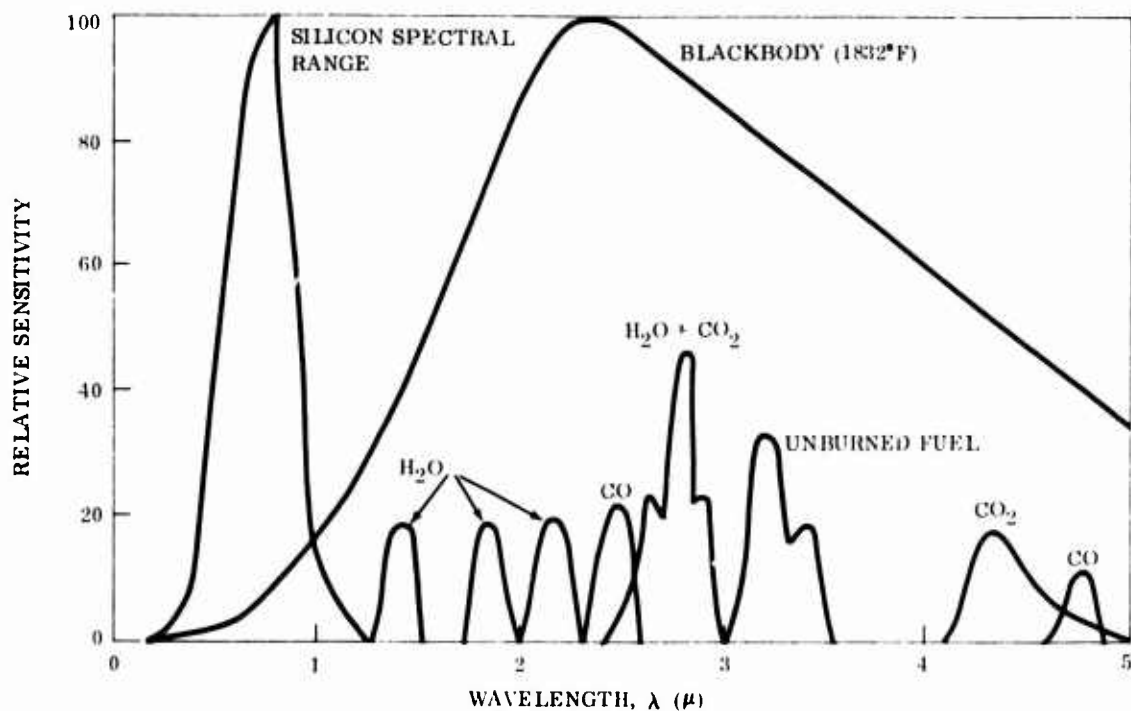


Figure 35. Spectral Radiation.

shielded from high temperatures and excessive vibration. Design to allow reliable performance in this environment occupied a major portion of the development effort invested in a radiation sensor for turbine blade temperature measurement.

#### Sensor Design

A schematic view of a radiation sensor designed for turbine blade temperature measurement is shown in Figure 36. The lens in combination with a field aperture defines the target area, receives the emitted radiation, and focuses the radiation on the fiber optic bundle. Fiber optics transmit the radiation from the hot turbine case to the detector located at some more remote, cooler, and more hospitable position on the turbine engine. The signal from the detector is processed electronically to produce meaningful and useful information. Processing may include linearization, averaging, or other functions designed to extract the desired information from the raw signal. The interface device protects the lens from the hot moving gas while allowing radiation from the target to pass.

#### Detector

Silicon photovoltaic detectors produce current proportional to the intensity of radiation incident upon their surfaces. Silicon is sensitive only to a narrow range of

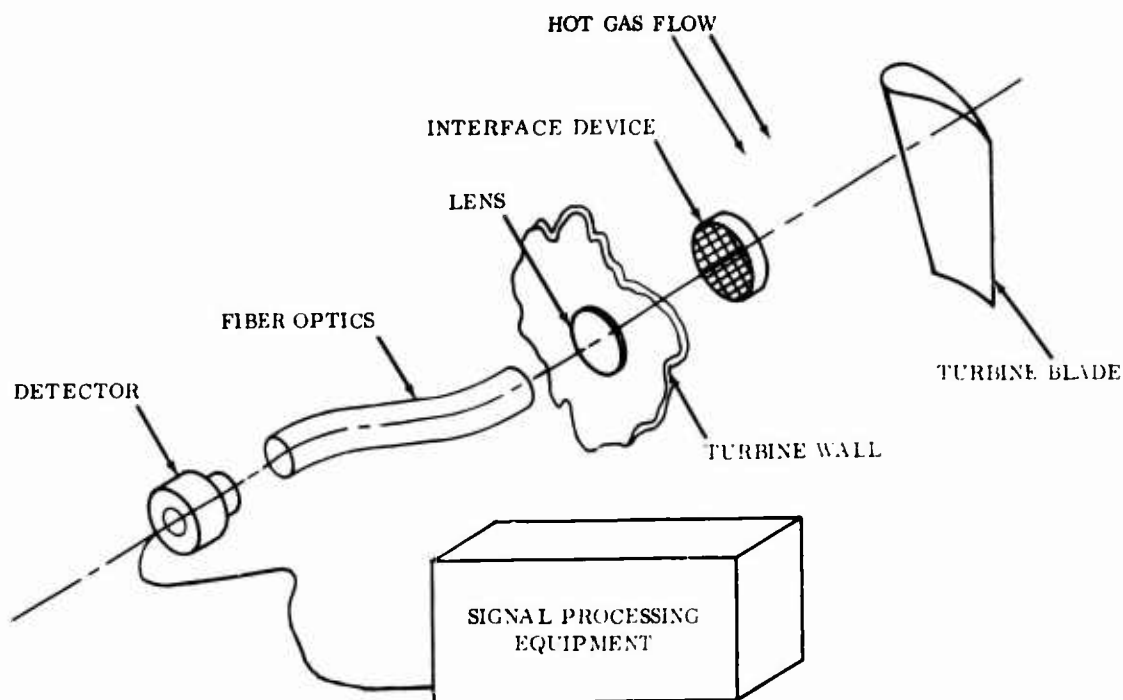


Figure 36. Schematic Radiation Sensor Design.

wavelengths between 0.4 and 1.12 microns (Figure 37) for a typical diode. Peak sensitivity is at 0.85 micron and is typically 0.3 to 0.5 ampere/watt. Sensitivity at a given wavelength is found by measuring the current produced by the detector, in amperes, for a given incident light power in watts. The active area may vary from less than 0.01 cm<sup>2</sup> to larger than 1.0 cm<sup>2</sup>. Noise equivalent power is used to describe the noise level of the diode and is equal to the incident radiant power needed to produce a signal-to-noise ratio of 1. Table XI lists two diodes investigated during the program with values of the important parameters.

TABLE XI. CHARACTERISTICS OF TWO SILICON PHOTODIODES					
Diode	Spectral Response (20% cutoff)	Sensitivity ( $\mu\text{A}/\mu\text{W}$ )	Area (cm <sup>2</sup> )	Diameter (mm)	Noise Equivalent Power (watts)
A	0.40 to 1.12 $\mu$	0.5	0.051	2.5	1 x 10 <sup>-10</sup>
B	0.45 to 1.05 $\mu$	0.3	0.196	5.0	3 x 10 <sup>-12</sup>

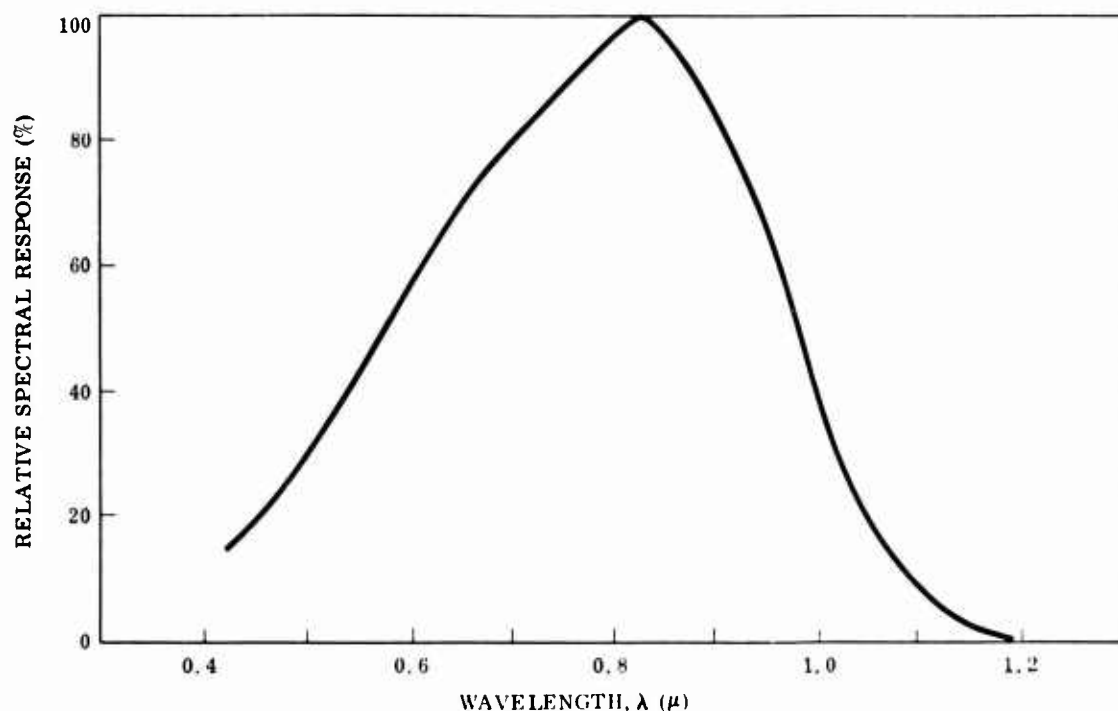


Figure 37. Silicon Spectral Sensitivity.

Diode B, shown in Figure 38, was used for most testing because its large active area and open configuration allowed a wide variety of tests and adaptations to be performed on a single diode. The photocurrent produced by the diode is passed through a resistor or operational amplifier circuit, and the output is measured as a voltage. Figure 39 shows a schematic op-amp circuit, where  $i_p$  is the photocurrent produced by the diode,  $v_o$  is the output voltage, and  $R_f$  and  $C_f$  are the feedback resistance and capacitance. The gain is controlled by the value of  $R_f$ .

### Optical System

The optical system consists of an objective lens, field aperture, and fiber optic bundle. The objective lens is made of quartz to resist high temperatures and to allow maximum transmission of the near-infrared radiation. Quartz has excellent thermal shock resistance and very low thermal expansion.

The fiber optic is a non-ordered bundle of clad glass fibers with an acceptance half angle of 30 degrees. Stainless steel fittings and flexible sheathing and a high-temperature binder allow the bundle to be used to 1000°F. Transmission losses are typically on the order of 40 percent on the ends and about 7 percent/foot of length. The field aperture is in the focal plane of the objective lens and defines



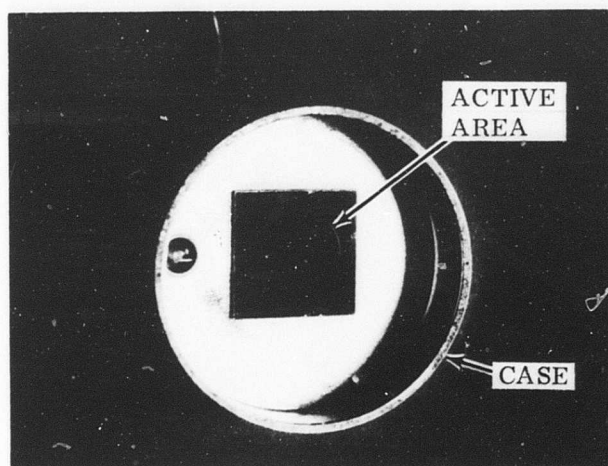


Figure 38. Silicon Detector.

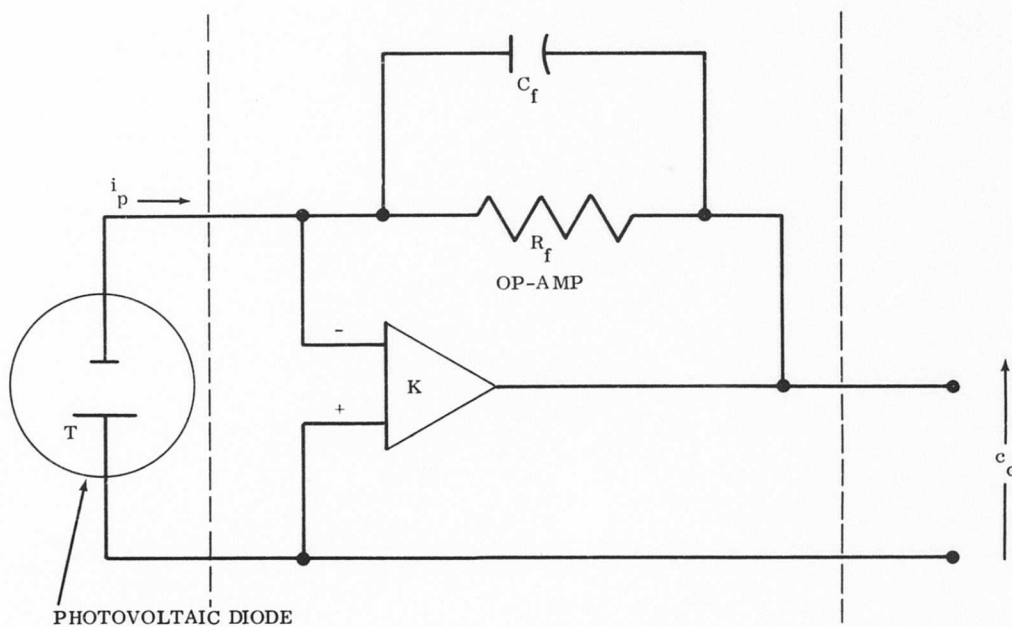


Figure 39. Operational Amplifier Circuit.

the size and shape of the target. Circular shapes were used in all cases during this program, but other shapes such as a rectangular slit can be used. On an operational design, the target would be shaped to provide the maximum information for a given blade shape and configuration.

The interface protects the lens from contamination and optical blockage. Compressor discharge air is used to purge the front of the lens. The simplest approach is to stand the lens away from the hot gas stream with a purge tube far enough to keep soot or other particles from reaching the lens. However, radiation is dissipated as the square of the target to lens distance, so it is advantageous to bring the lens as close to the target as possible. The interface device directs the purge air to prevent backstreaming of soot particles and to minimize lens-to-target distance. Two designs were tested during the program and are shown in Figure 40. The gas collimator is made up of many parallel passages that tend to cause laminar flow and reduce backstreaming. Passage size is determined by the amount of air available and the geometry of application. The disadvantage of this design is that it blocks part of the optical path. The multinozzle interface is made up of concentric annular nozzles that direct air both toward and away from the lens, causing a flow pattern that restricts backflow.

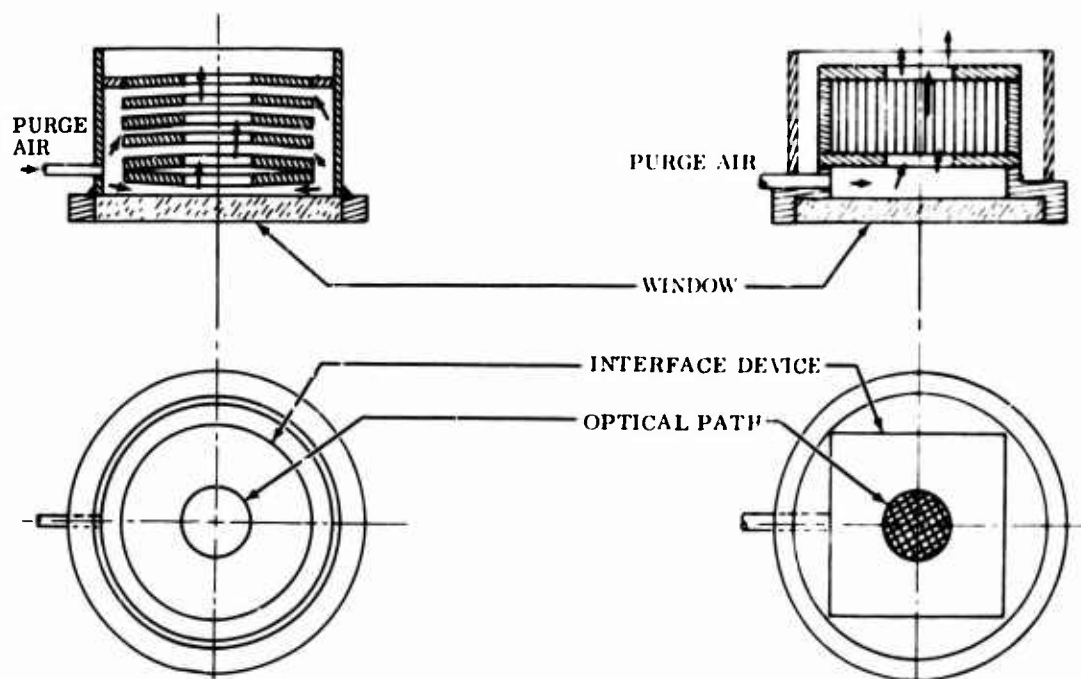


Figure 40. Interface Devices.

### Signal Processing System

The main function of a signal processing system is to convert the highly exponential output signal of the silicon detector to a linear voltage directly proportional to blade temperature in °F. A secondary function is to amplify the signal sufficiently to operate any type of temperature meter or controls that might be used. The signal strength is a function of the target temperature raised to the tenth or greater power for the range of temperature of interest (at 1800°F the exponent is 12). Although this creates a highly nonlinear output voltage, it also produces the significant advantage of high sensitivity and accuracy. Errors in the electronic system are included in the factors reduced to the  $n$ th root when temperature error is calculated (equation 13). An inaccuracy of 10 percent in the electronics corresponds to a temperature error of 1 percent. Based on the foregoing information, it is seen that the error in the electronic components is added at a greatly reduced factor when the temperature is determined.

A factor that is not reduced in establishing temperature accuracy is linearization. Derivations of the linearization equation from the calibration curve are temperature errors. Thus, accurate linearization becomes the most important factor when overall electronic system error is being considered.

### Linearization System

The choice of a linearization system depends upon overall system accuracy objectives and the range over which a linear electrical output signal is desired. For the demonstration laboratory system, it appears desirable to establish a  $\pm 15$ -degree accuracy objective over a 1500° to 2100°F range. This choice was established by a preliminary evaluation of three methods, with program cost and scope limitations as the main constraints. In all cases, available off-the-shelf components or subsystems were used for the system design. For specially designed components, it is expected that considerably greater improvements in production unit cost and equation matching can be achieved; however, this is beyond the scope of the present program.

### Digital System

The most accurate method would be to use a digital system. In this system, the filtered signal goes through a peak detection circuit and then to a microvoltmeter. The analog input is converted to a digital signal which then goes to a linearizer. From the linearizer, the signal is used to operate a digital temperature display in °F. This basic system has an input voltage measuring capability within  $\pm 0.01$  percent. Thus, virtually the entire system accuracy allowance is established by the linearization circuit. This has been calculated to be better than 3°F. Cost

is the main disadvantage of this system. It would cost several thousand dollars to assemble one system as described above. Analog circuits are less accurate but considerably lower in price, and will be considered in more detail.

### Analog Systems

#### Log Amplifier

Figure 41 shows the simplest approach using a logarithmic amplifier. The circuit is designed for use in a laboratory research program; thus all gains and equation constants are made adjustable. An actual production unit would probably not need variable adjustments and could use a simple single-stage amplifier. The basic function of the circuit is to solve the approximate linearization equation of the silicon detector sensor. The output of the sensor developed for this program is approximately logarithmic with respect to temperature. Analysis of the curve for a 1000Ω load (Figure 42) yields an approximate linearization equation.

$$T = 100 V_o = 1650 + 370 \log_{10} (100 V_{in})$$

where  $V_o$  is the output voltage of the linearization circuit and  $V_{in}$  is the input to the circuit from the sensor.

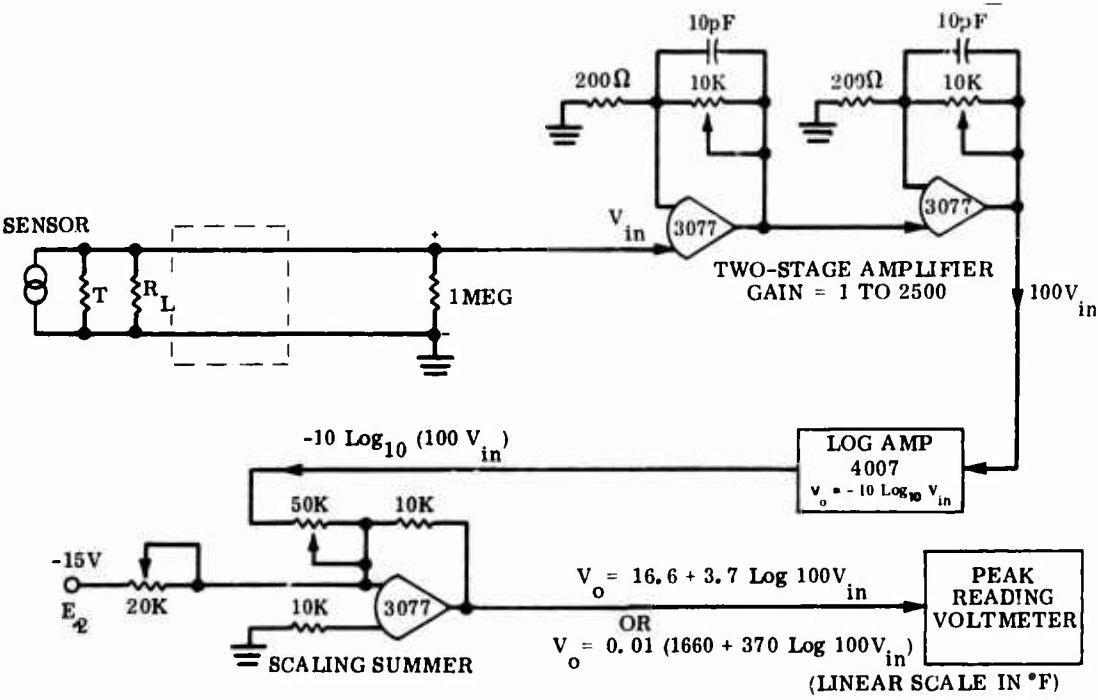


Figure 41. Logarithmic Amplifier Linearization System.

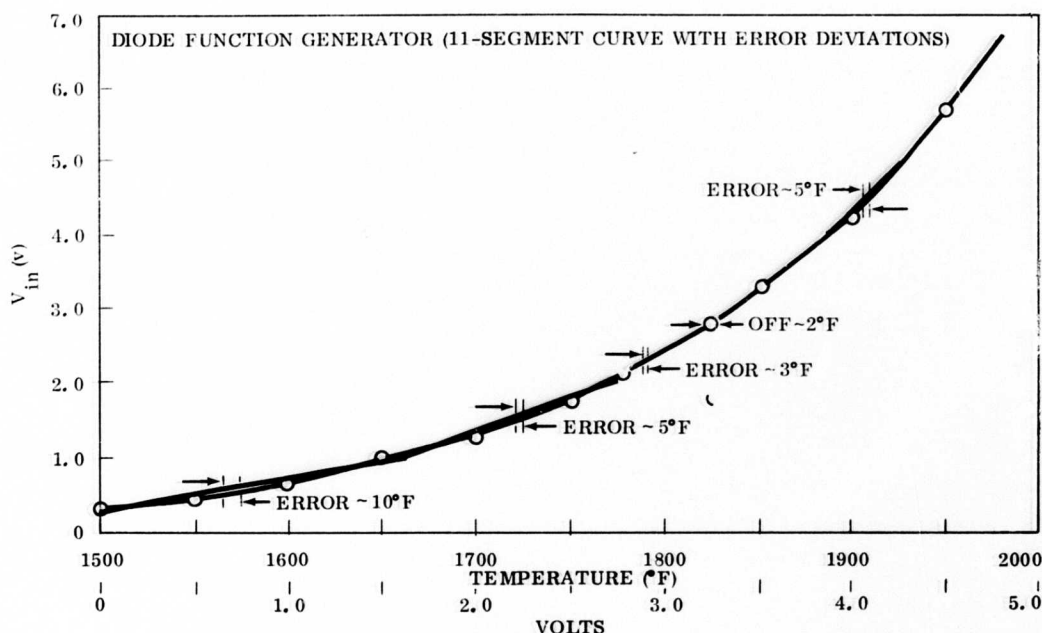


Figure 42. Detector Output Showing 11-Segment Linearization.

Table XII shows how the temperature calculated by this equation deviates from the actual temperature calibration of the sensor. The error is zero at 1600° and 1800°F. Thus, if 1600°F were the normal operating point, no linearization error would be associated with its reading. Minor adjustments of the equation could be made to move the zero error points to the normal operating temperature.

The logarithmic equation can be solved with the electronic system shown in Figure 41. The input (output from the sensor) signal is amplified by a factor of 100 in a two-stage adjustable gain amplifier section. With the values of resistances selected, this gain is adjustable from 1 to 2500. The adjustable feature and the two-stage amplification capability have been selected to allow sufficient flexibility for the research testing program now planned. They would not normally be required for a production unit, and a single-stage amplifier with limited adjustment would be adequate. The amplified signal is then operated on by a standard logarithmic amplifier that yields an output of  $-10 \log_{10} (100 V_{in})$ . Accuracies of  $\pm 2$  percent of full scale are typical with a bandwidth ( $\pm 1$  db) of 6 kHz and an output drift of  $\pm 5$  mv/°C. The output from the log amplifier is then added to the remainder of the equation by an adjustable equation adder amplifier.

TABLE XII. CALCULATED LOGARITHMIC LINEARIZATION ERRORS			
Actual Temperature (°F)	Indicated (Calculated) Temperature (°F)	Error	
		(deg)	(%)
1400	1375	-25	-1.8
1500	1487	-13	-0.0
1600	1600	0	0
1700	1702	+ 2	+0.1
1800	1800	0	0
1900	1873	-17	-0.9
2000	1978	-12	-0.6
2100	2066	-34	-1.6

Although this system is the least expensive, its total accuracy suffers since the output of the sensor departs from a true log curve. The best equation accuracy adjustments will result in errors of approximately  $\pm 20^{\circ}\text{F}$ . These errors could be greatly reduced by reducing the range, but for  $1500^{\circ}$  to  $2100^{\circ}\text{F}$  a more accurate linearization system is required.

#### Function Generator System

Figure 43 shows the system selected for this program. It is similar to the previously discussed system except that the linearization is accomplished by a diode function generator. The nonlinear relationship can be more accurately approximated by an 11-segment function generator. A Burr-Brown diode function generator (Model 4062) shapes the functional relationship between temperature and input voltage with 11 equally spaced straight line segments. Figure 42 graphically displays the deviations between the straight-line diode curves and the curve representing the output of the sensor. Estimates from this curve show a maximum temperature error of approximately  $10^{\circ}\text{F}$  when solving the equation

$$T = 100 V_o = 1500 + 50 f (100 V_{in})$$

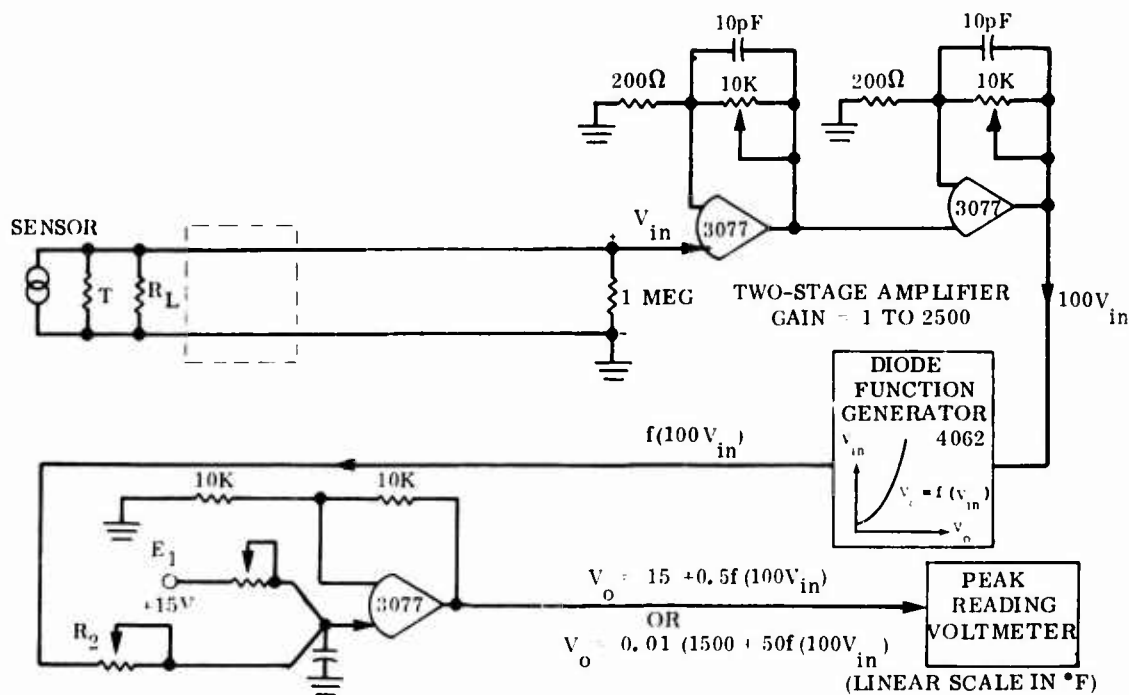


Figure 43. Diode Function Generator Linearization System.

The other circuit elements and their signal flow are identical or similar to the system previously described for the logarithmic system and are detailed in Figure 43. The output voltage from the circuit will be displayed on a voltmeter. All the components for this system are standard. Specially designed components can be tailored to the curve, making them less expensive and more accurate for production units.

## COMPONENT TESTING

### Detector

A series of calibrations with a wide range of load resistances was compiled to define the silicon diode characteristics and the temperature calibration of the silicon detector. A quartz lens with an effective diameter of 0.84 inch and a 1.0-inch focal length projected a 0.39-inch target diameter onto the detector. A transfer factor of  $2.18 \times 10^{-3}$  was calculated for a lens to target distance of 3 inches.

A 0.4375-inch-diameter graphite cavity 1.25 inches long provided an approximate black target. The cavity was heated by a small, wire-wound, electric furnace. The temperature of the target was measured by a Pt-Rh thermocouple inserted through the back wall of the cavity. The calibration test equipment is shown in Figure 44. The furnace was stabilized at the test temperature, and the detector output was read as a millivolt drop across the load resistance ( $R_L$ ) for each of the

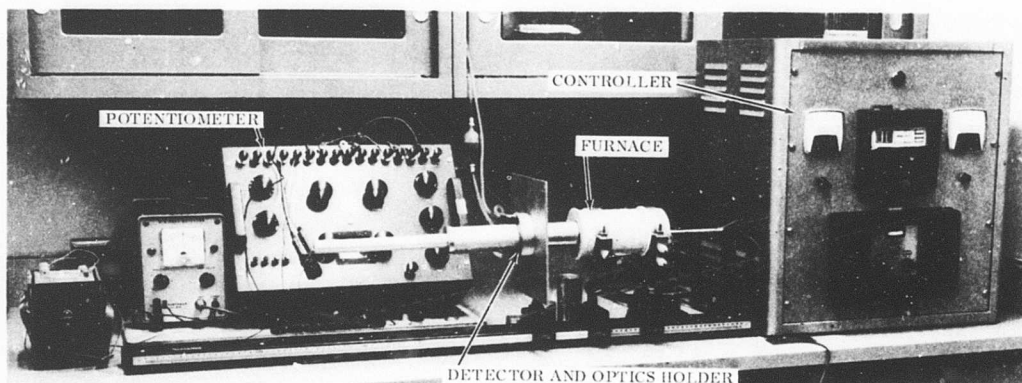


Figure 44. Calibration Test Equipment.

five test conditions. Load resistances of 100, 500, 1000, and 10,000 ohms were used. A Leeds and Northrup K-3 Potentiometer was used to measure the voltage drop across the resistor. The detector output signal is shown in Figure 45 as a function of temperature for four different load resistances. The current-voltage characteristics of the diode are shown in Figure 46. The current produced by a given level of illumination (target temperature) is seen to be a function of the voltage across the diode. The saturation observed in Figure 45 at high temperature corresponds to the nonlinear behavior at high voltage shown in Figure 46. Each value of load resistance imposes a current voltage characteristic shown as a straight line for each resistance. Short-circuit conditions provide a linear relationship between illumination and current which at higher voltage becomes logarithmic.

An operational amplifier circuit (Figure 39) allows short-circuit behavior by the diode and the most optimum characteristics for use as a detector. Figure 47 is a circuit diagram of the amplifier that converts the photocurrent to a voltage and then amplifies it. The adjustable feedback resistance allows variable gain in each stage.

Detector current is also a function of its own ambient temperature. Silicon diodes are limited to approximately 250°F maximum temperature. Within this limit, the current produced by the detector for a given target temperature is linearly proportional to the diode temperature. The increase in detector current with increasing temperature is caused by increased sensitivity to the longer wavelengths. Therefore, to maintain an accurate calibration, the detector signal must be compensated for changes in diode temperature. This may be accomplished in two ways:

- Add a temperature-sensitive resistance in the feedback loop of the amplifier to adjust the gain to counteract changes in current.
- Filter out longer wavelength radiation so that changes in sensitivity are unimportant.



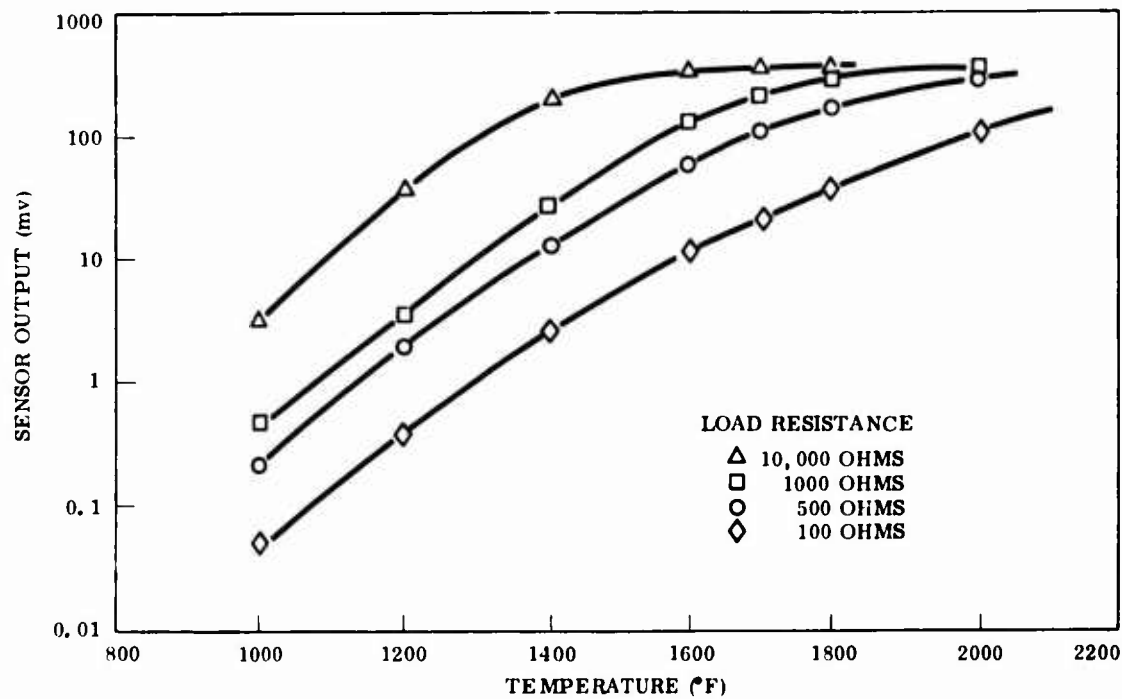


Figure 45. Diode Calibration.

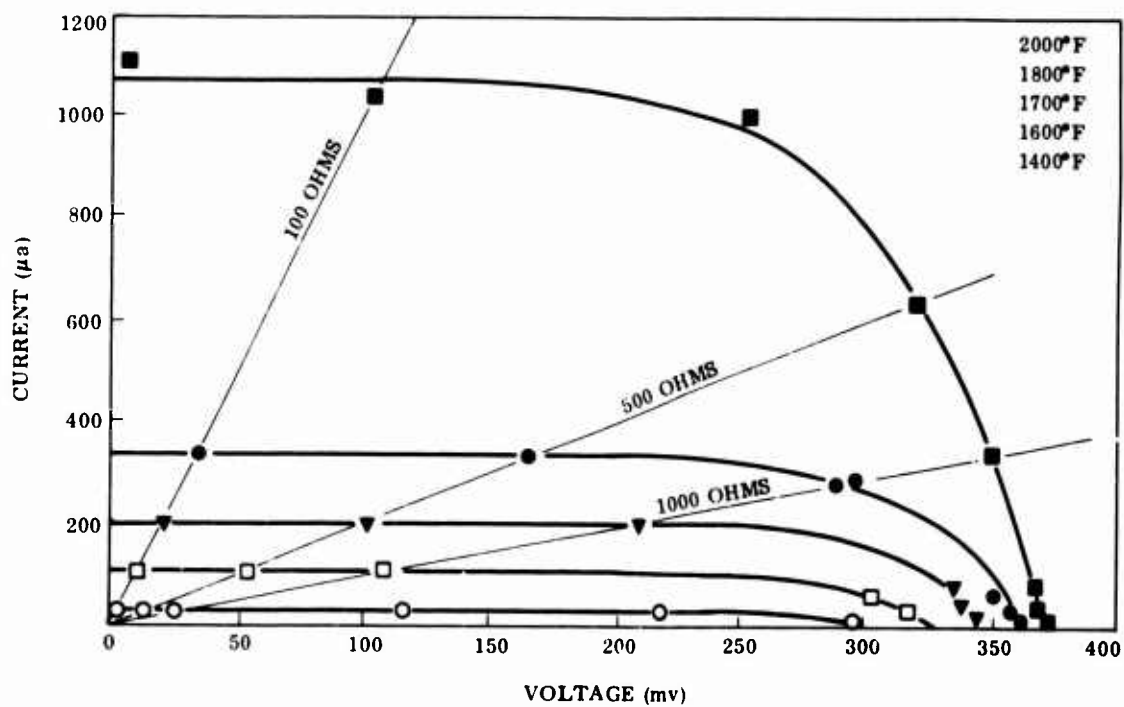


Figure 46. Diode Characteristics.

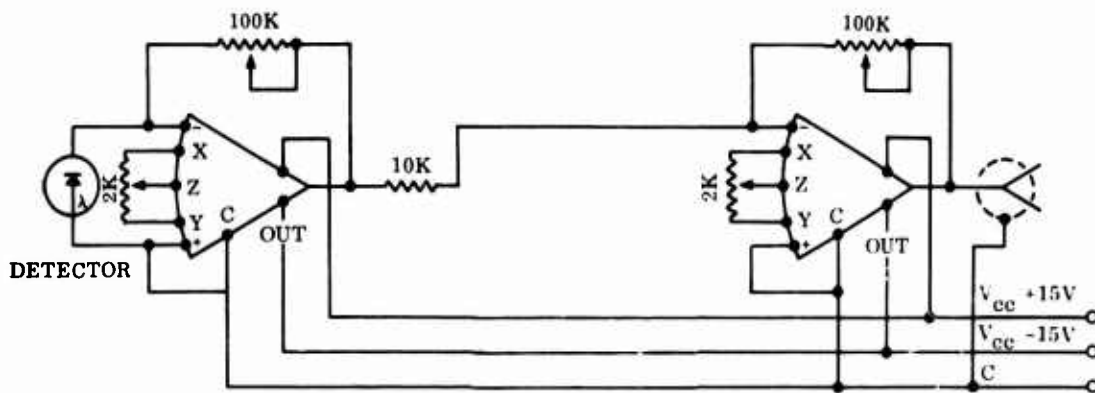


Figure 47. Amplifier Circuit Diagram.

The second approach using a dichroic filter with a 9.0-micron cutoff wavelength was tested. The filter passed approximately 70 percent of the radiation between 4.5 and 9.0 microns and reflected greater than 99 percent of the radiation outside this band. The filter was placed between the target and the detector, and the detector signal was recorded as a function of detector temperature between 70° and 200°F. Figure 48 shows the detector signal with and without a filter for two diodes. Without a filter, the signal change was linear with temperature. There was little change in output with the filter in place. The principal disadvantage in using a filter is the overall reduction in signal strength. Filters with a longer cutoff wavelength would cause less overall reduction in signal strength.

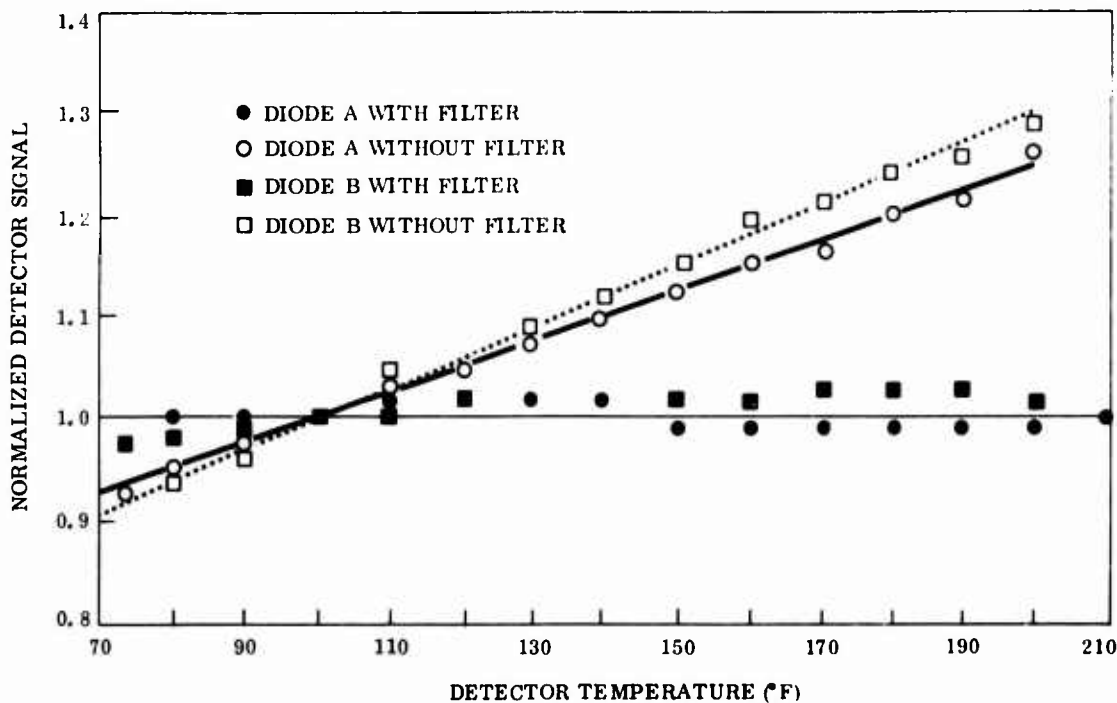


Figure 48. Ambient Temperature Compensation.

### Optical System

The thermal capabilities of a high-temperature fiber optic bundle purchased from Dyonic, Inc., were measured. The fiber bundle was composed of glass fibers bonded with a ceramic potting compound at each end. The fibers were encased in a metal mesh sheath with stainless steel end fittings (Figure 49). A silicon diode was placed at the cold end of the fiber bundle, and the other end was placed in the cylindrical muffle of an electrically heated furnace approximately one inch from a graphite target. The test setup is shown schematically in Figure 50. A chromel-alumel thermocouple measured temperature at the end of the fiber bundle. The bundle, at ambient temperature, was placed into position in the furnace with the target already at temperature, and its transmission was measured as it increased in temperature. The maximum ambient temperature capability of the fiber optic bundle was established as approximately 1000°F. Long-term effects of high temperatures or thermal cycling were not established. Data for several tests are shown in Table XIII.

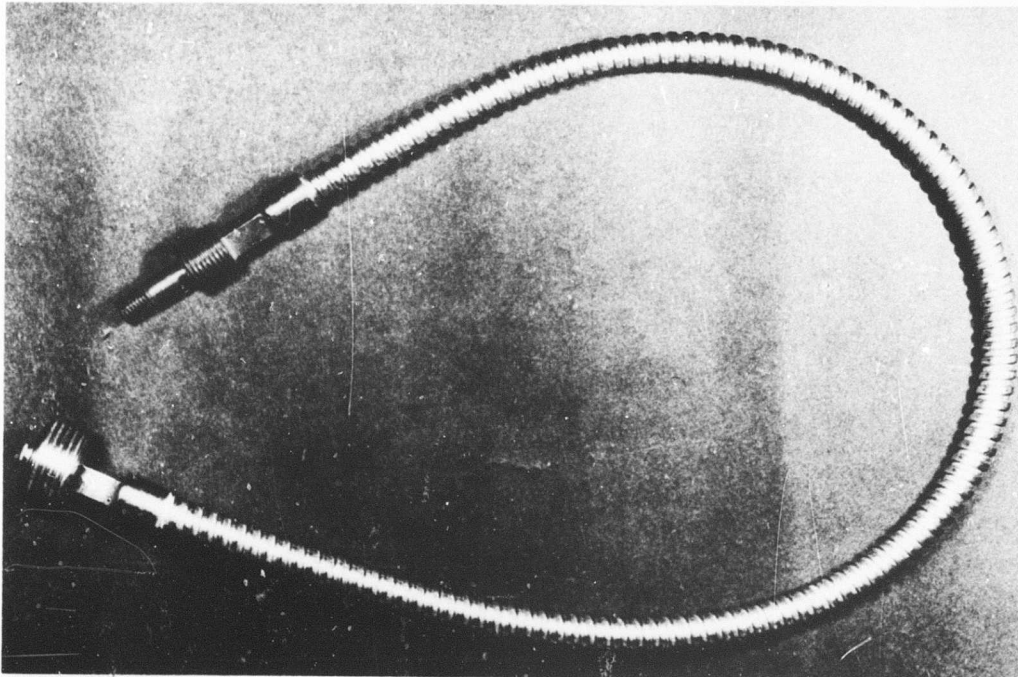


Figure 49. Fiber Optic Bundle.

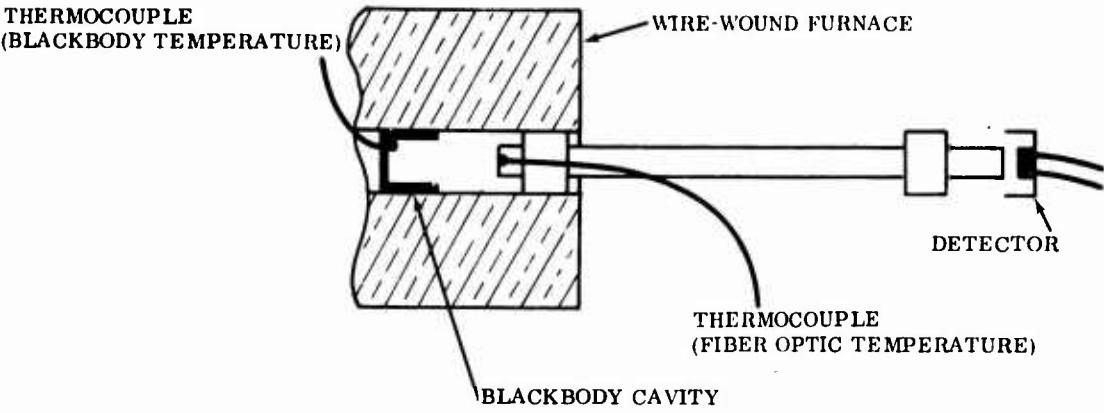


Figure 50. Fiber Optic Temperature Test.

TABLE XIII. FIBER OPTIC TEMPERATURE DATA				
Fiber Optic Temperature (°F)	Detector Output (v)			
	Test No. 6 BB = 1600°F (mv)	Test No. 7 BB = 1600°F (mv)	Test No. 8 BB = 1700°F (mv)	Test No. 9 BB = 1700°F (mv)
200	53 ± 0.05	53 ± 0.05	99	-
400	53	53	99	-
600	53	53	99	87
800	53	52	99	86
900	53	52	98	86
950	53	52	98	-
1000	52	52	98	86
1050	-	-	98	86
1100	-	-	88	82
1120	-	-	-	70
1130	-	-	-	55

Test Number 6 maintained a blackbody temperature of 1600°F. The detector output was measured for fiber optic temperatures from 200° to 1000°F. Transmission remained constant up to 950°F and then dropped two percent and remained constant at 1000°F. The test was repeated (Test Number 7) with essentially the same results except that the reduction in transmission began near 800°F. The 1000°F temperature was maintained for approximately one hour with no further loss in transmission. The blackbody temperature was raised to 1700°F and the test was repeated (Test Number 8). Transmission again remained constant (detector output = 99 millivolts) up to a fiber optic temperature of approximately 900°F, where it dropped one percent (= 98 millivolts) and remained constant up to 1050°F and then dropped 10 percent (= 88 millivolts) at 1100°F. The bundle was removed and cooled to room temperature. It was reheated again (Test Number 9), but the transmission remained at the level to which it had fallen in the previous test even at low fiber temperatures. This test indicates that the transmission does not recover after a certain temperature is surpassed. The smaller reductions around 850° to 900°F are probably caused by changes in the transmission characteristics of the glass.

The detector output was also measured as a function of fiber optic temperature with no target in the optical field of view. The purpose was to measure the amount of error caused by radiation reaching the detector that originated not from the target but in the hot end of the fiber bundle. Table XIV shows the detector reading and fiber temperature ( $R_L = 500 \text{ ohms}$ ).

TABLE XIV. EXTRANEOUS SIGNAL FROM HOT FIBER OPTICS	
Fiber Optic Temperature (°F)	Detector Signal (mv)
750	0.0
800	0.1
1000	1.0
1100	2.0
1200	3.0

At most temperatures, the extraneous signal produced by radiation from the hot fibers will not be significant. However, at temperatures above 800°F it must be considered, especially at low target temperatures. The effect of an offset due to a hot fiber bundle will depend strongly on the target temperature. One millivolt might be 1 percent of the signal from a 1700°F target, 2 percent of the signal from a 1600°F target, and 50 percent or more from a 1200°F target. Testing must be done on specific sensor designs and target configuration and temperatures to be evaluated in terms of the temperature error caused by hot fiber optics.

The interface devices were tested for optical blockage and their effectiveness in keeping a window clear from soot. Collimators were made from corrugated 0.002-inch-thick Hastelloy foil. The convoluted foils were stacked alternately with straight foils and laid up in a rectangular box. Figure 51 shows a typical test collimator. Some optical blockage occurs due to the foil cross-section and misalignment of the passages. Table XV shows the percentage of the total light transmitted for several passage sizes.

TABLE XV. OPTICAL BLOCKAGE			
Collimator	Passage Area (in. <sup>2</sup> )	Passage Length (in. )	Signal Transmitted (%)
1	0.0015	0.5	46
2	0.005	0.5	68
3	0.012	0.5	79
4	0.032	0.5	86

The multinozzle interface (Figure 40) was fabricated from conical-shaped washers spaced by wires. The optical path diameter was 0.5 inch and the overall diameter was 1.0 inch. No optical blockage was caused by the multinozzle.

The effectiveness of the various interfaces was qualitatively tested by using the devices to protect a window interfaced with soot-laden air at ambient temperature and pressure (Figure 52). A powder feeder was used to meter carbon black into the air stream. This test apparatus provides a comparison of a nonprotected window and windows protected by various interface devices under similar geometric conditions. The direction normal to the window (optical axis) is perpendicular

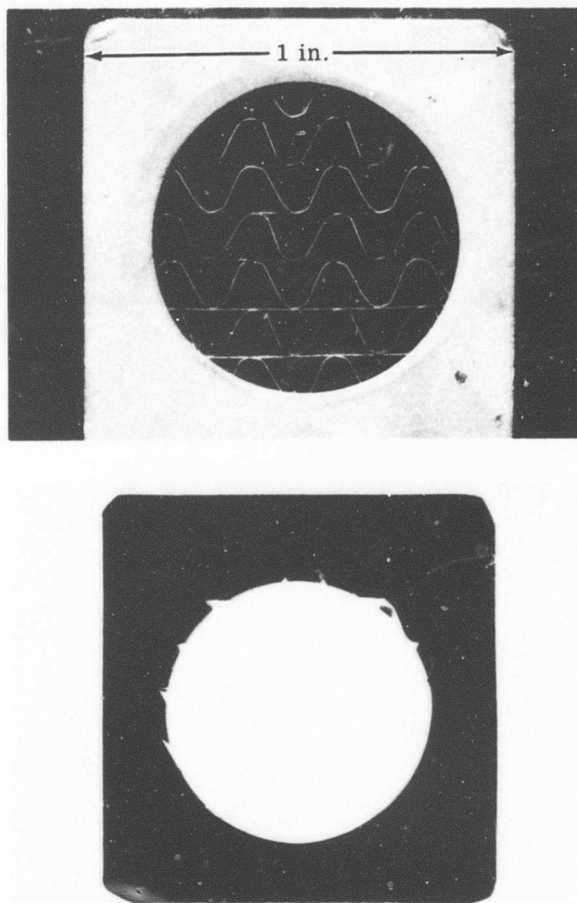


Figure 51. Collimator Interface.

to the direction of soot flow. This condition is more severe than most projected applications, which would place the optical axis at an acute angle to the direction of flow.

A window protected only by purge air with no interface device was included in each test for comparison. The available literature (Ref. 26 and 27) indicates that the typical soot content of a turbine engine exhaust stream is on the order of 0.1 to 1.0 mg/ft<sup>3</sup> of air. Typical test conditions are outlined in Table XVI.

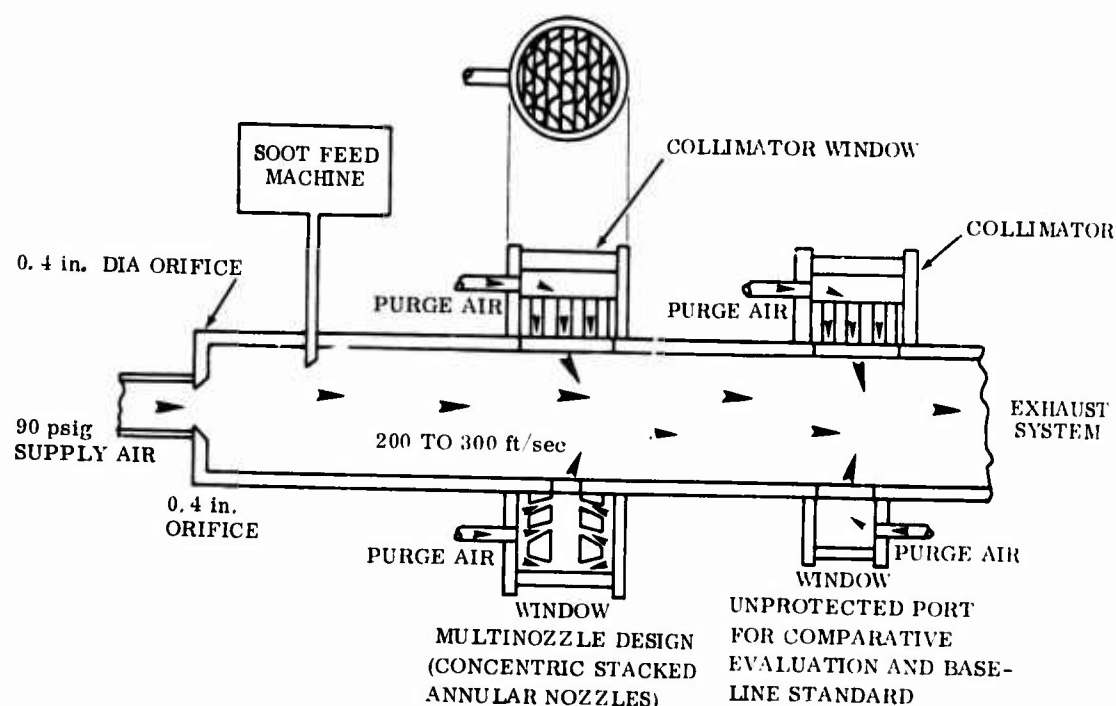
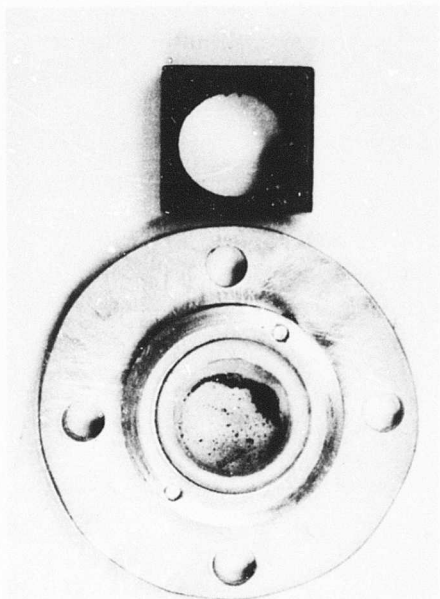


Figure 52. Soot Tester.

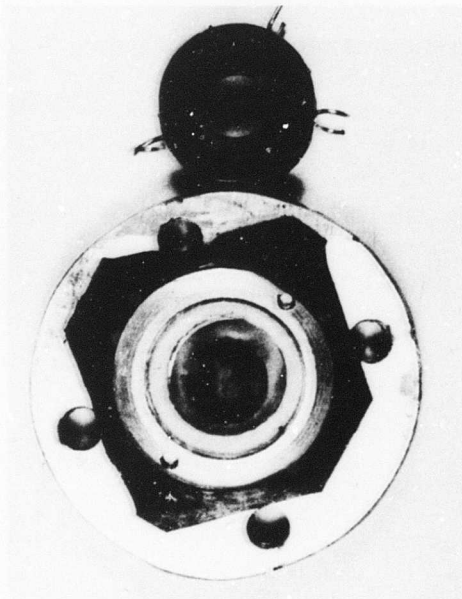
TABLE XVI. INTERFACE TESTS	
Function	Value
Main airflow	2.0 ft <sup>3</sup> /sec
Main air velocity	230 ft/sec
Soot flow	1.4 mg/sec 0.7 mg/ft <sup>3</sup>
Purge airflow	0.0024 lb/sec
Total time	75 hours

Figure 53 shows each window and its corresponding interface device after the exposure was completed. Figure 53A shows the unprotected window. The heavy accumulation of soot is on the downstream side of the window. The multinozzle (Figure 53B) allowed a film of soot to be deposited over most of the window surface. Figure 53C shows a 0.5-inch-deep collimator (passage area of 0.0015 in.<sup>2</sup>) with

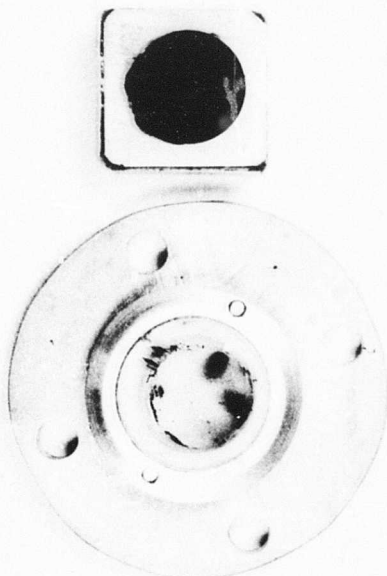




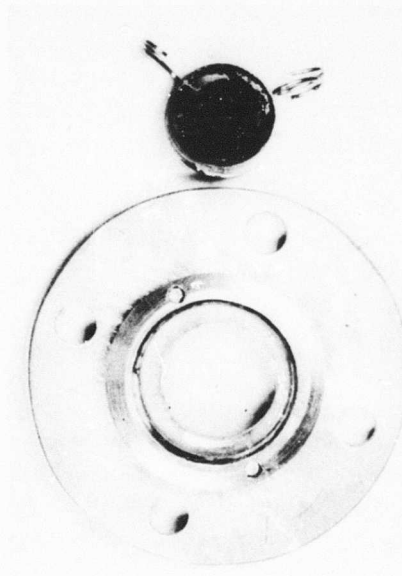
A. Standard



B. Multinozzle



C. Collimator



D. Collimator

Figure 53. Windows and Interface After Exposure.

some sooting evident. A 0.25-inch-deep ( $0.0015 \text{ in.}^2$  passage) collimator (Figure 53D) with a 0.4-inch-diameter optical path kept the window clean for the 75 hours of the test. Considerable testing was only able to yield comparative data for a particular set of geometrical conditions. The tests did allow some conclusions to be drawn. Soot built up on some of the smaller passages, tending to block transmission. The collimators with larger size passages need more purge air to maintain a clean window. The effectiveness of the multinozzle varied considerably with geometry and airflow, and further development of the design is needed to provide adequate effectiveness. The multinozzle has the considerable advantage over the collimator of having a clear optical path.

### Signal Linearizer

A signal linearizer was breadboarded to the circuit shown in Figure 43 and is shown in Figure 54. Overall dimensions are 17 by 5 inches. The system consists of a power supply, three operational amplifiers, a 10-segment diode function generator, and various minor components. The amplifier gains and segments of the diode function generator were adjusted to fit an input curve (output from a diode with a 500-ohm load resistance), shown in Figure 55. Detector sensitivity is indicated at three points on the curve. Target-to-lens distance was 3.0 inches, with a 0.5-inch-diameter lens and a 0.394-inch-diameter target. The linearizer was adjusted by using a known input from a voltage source and adjusting the output to fit the desired curve. Table XVII shows the differential between the final output and the expected output for a given input signal. The error equivalent to the voltage difference is also shown and is less than  $3.5 \pm 3^\circ \text{ F}$  over the entire range.

The linearizer was then tested with an input signal from a silicon detector focused on a blackbody target. The temperature of the blackbody was measured with a Pt-Rh thermocouple. The output signal was measured directly from the function generator without further amplification. Table XVIII and Figure 56 show the calculated and experimental values.

Over the range of temperature between  $1550^\circ$  and  $2000^\circ \text{ F}$ , the linearizer detector circuit produced a linear signal accurate to within  $\pm 10^\circ \text{ F}$ . The linearizer demonstrated the feasibility of processing the highly logarithmic current produced by the detector into a useful, linear signal. No attempt was made to design a system that could function at high frequencies typical of a turbine blade target.

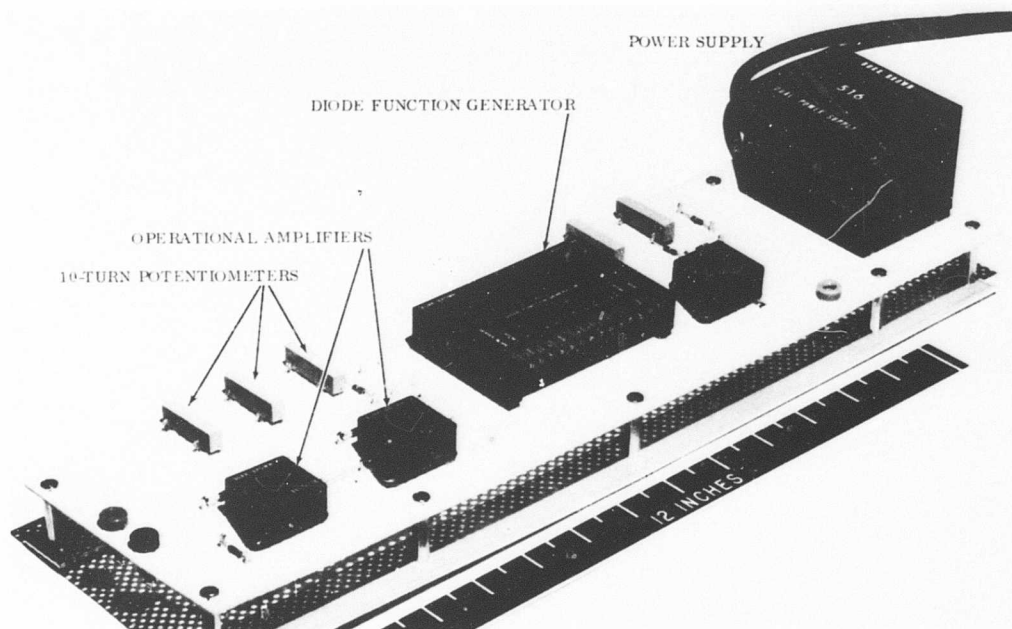


Figure 54. Signal Linearizer.

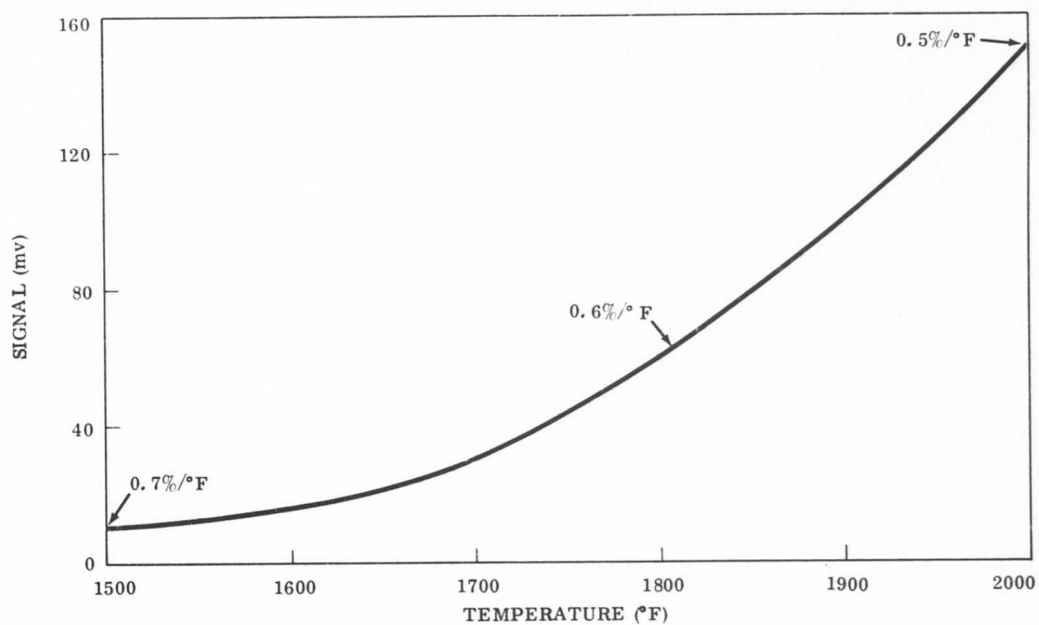


Figure 55. Detector Input to Linearizer.

TABLE XVII. ADJUSTMENT OF THE SIGNAL LINEARIZER				
Input (mv)	Output (v)	Expected Output (v)	Error	
			(v)	(°F)
20	2.45 ± 0.02	2.40 ± 0.04	+0.06 ± 0.06	3.0 ± 3
40	4.65	4.63	+0.02	1.0
60	6.12	6.10	+0.02	1.0
80	7.15	7.17	-0.02	1.0
100	8.00	8.00	0	0
120	8.63	8.67	+0.05	2.5
140	9.20	9.27	-0.07	3.5
160	9.70	9.73	-0.03	1.5

TABLE XVIII. SIGNAL LINEARIZER			
Temperature (°F)	Calculated Signal (v)	Experimental Signal (v)	Temperature Error (°F)
1500	0	-	-
1550	1	0.85	7.5
1600	2	1.80	10.0
1650	3	2.85	7.5
1700	4	3.90	5.0
1750	5	5.00	0
1800	6	6.00	0
1850	7	7.00	0
1900	8	8.00	0
1950	9	9.00	0
2000	10	10.00	0

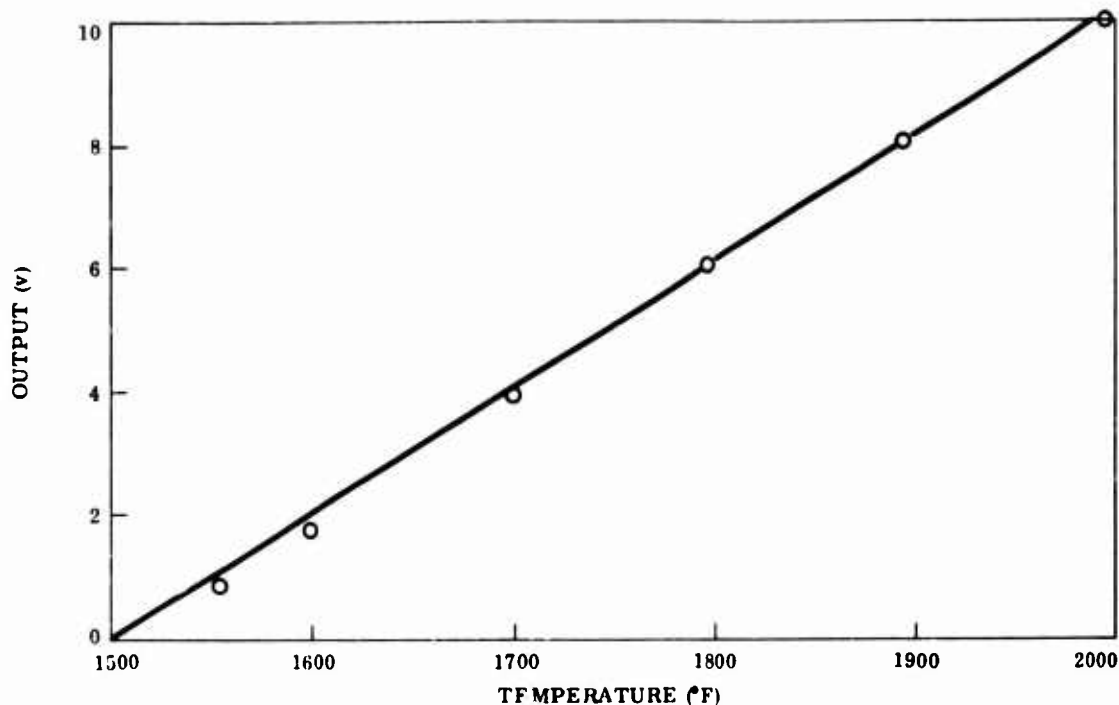


Figure 56. Linearized Signal.

#### SIMULATED ATMOSPHERE TESTING

Test blades in a high-temperature engine simulator were viewed by a silicon detector radiation sensor developed on a preceding contract (Ref. 3). The purpose of the test was to determine the effect of hot luminous gas on the sensor signal in preparation for actual turbine engine testing. An overall view of the test cell is shown in Figure 57. A constant airflow is supplied to the combustor, and the fuel flow is regulated by a thermocouple inserted in the target blades and connected to a controller through a slip-ring system on the rotating shaft. Target temperature is also monitored by optical pyrometry. Each of the two rigs can be run independently of the other. Gas temperatures up to 2800°F are obtainable at near sonic velocities. Figure 58 shows the target holder and blades. Two silicon detector pyrometers were sighted on target blades rotating at approximately 1800 rpm in a 2500°F gas stream. Gas velocity was approximately 200 fps. Figure 59 is a schematic diagram of the rotating targets and their spacial relationship to the two sensors, and a photograph of a sensor in place during a test. The detector was coupled with a 10,000-ohm load resistance, and the voltage was recorded on an oscilloscope adjusted to a four kHz bandwidth. The target diameter of 0.3125 inch was completely filled for the top pyrometer, but not for the side pyrometer, which looked at an angle across the tips of the blades. Since the intensity of the

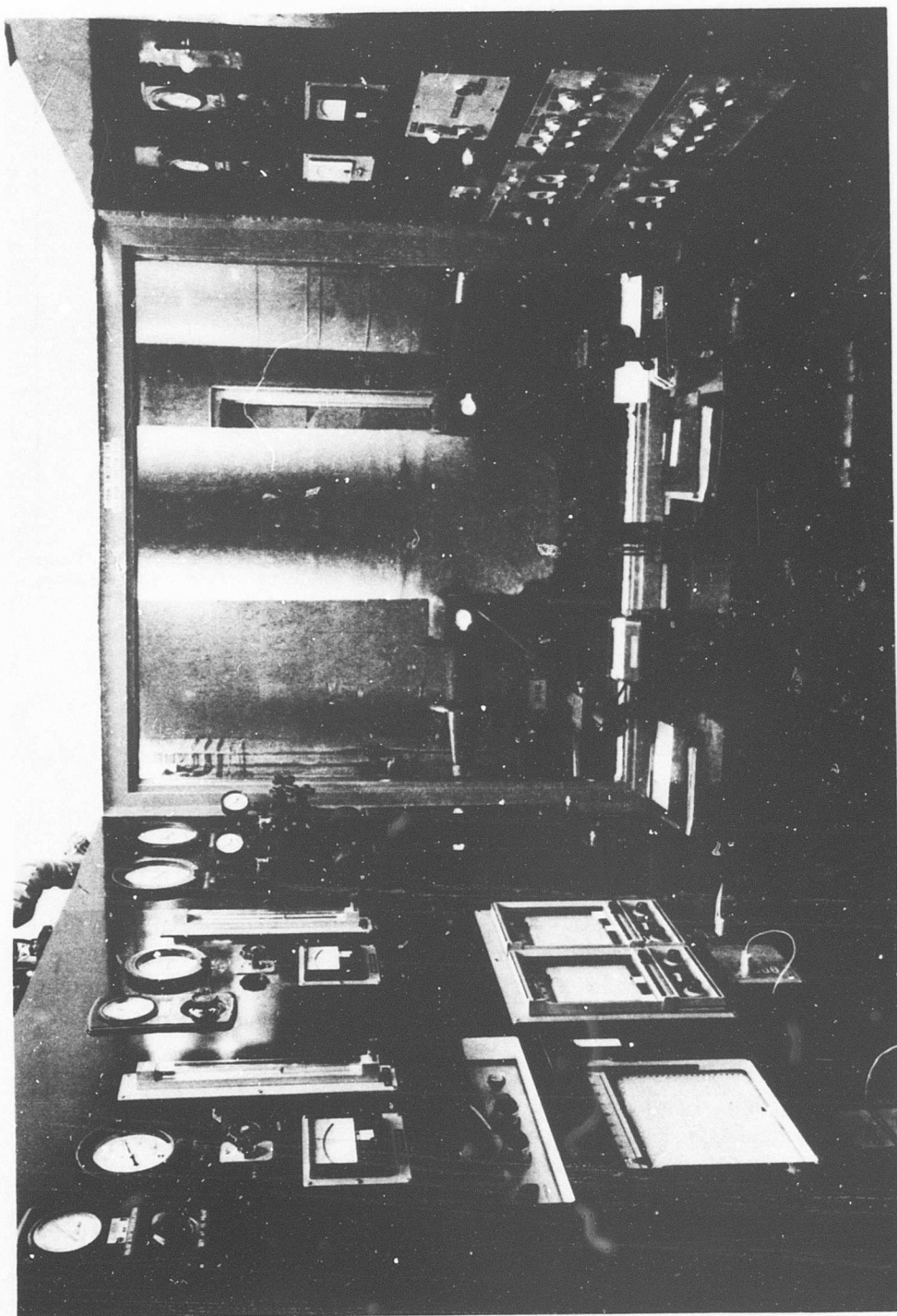


Figure 57. High-Temperature Engine Simulator.

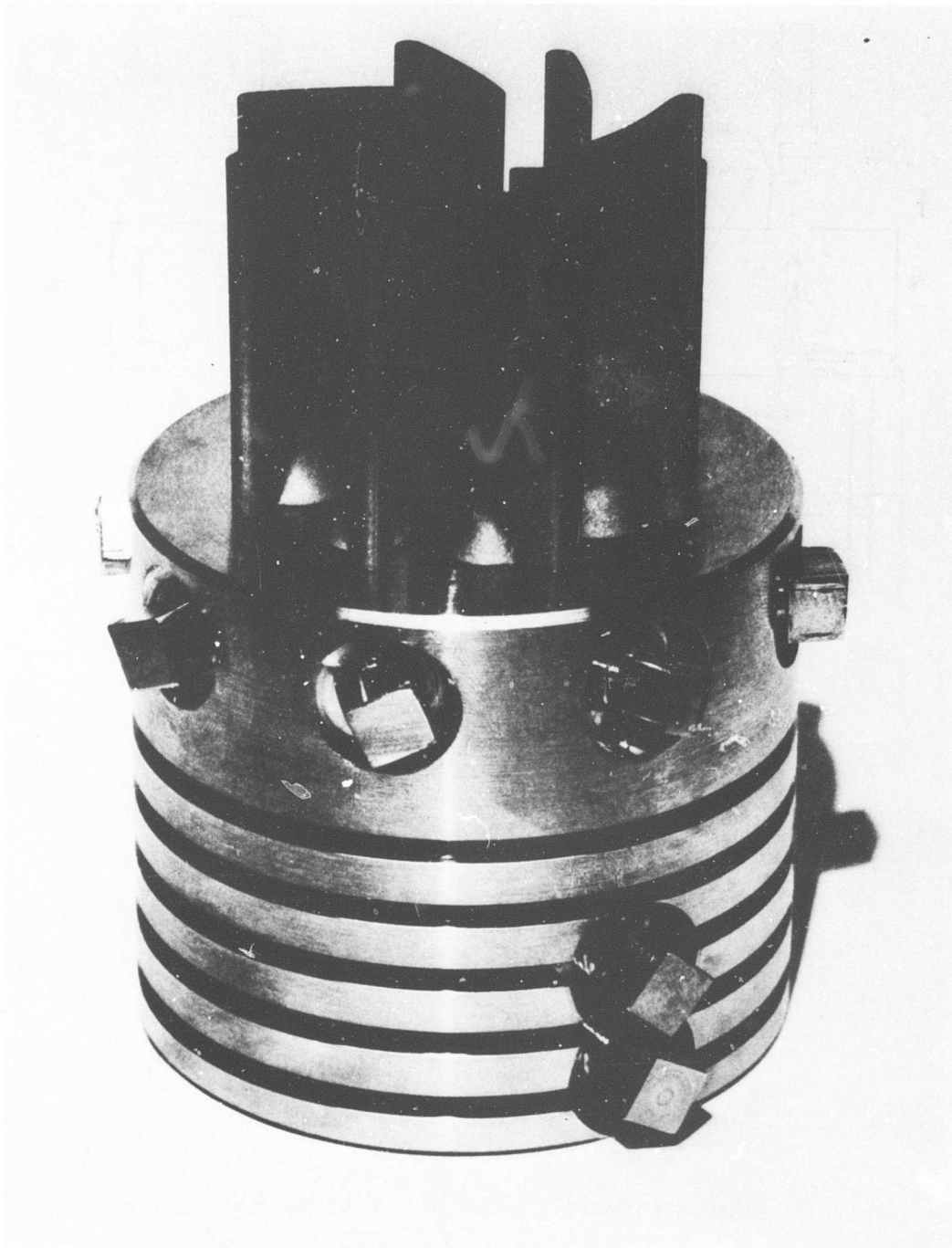


Figure 58. Target Holder and Blades.



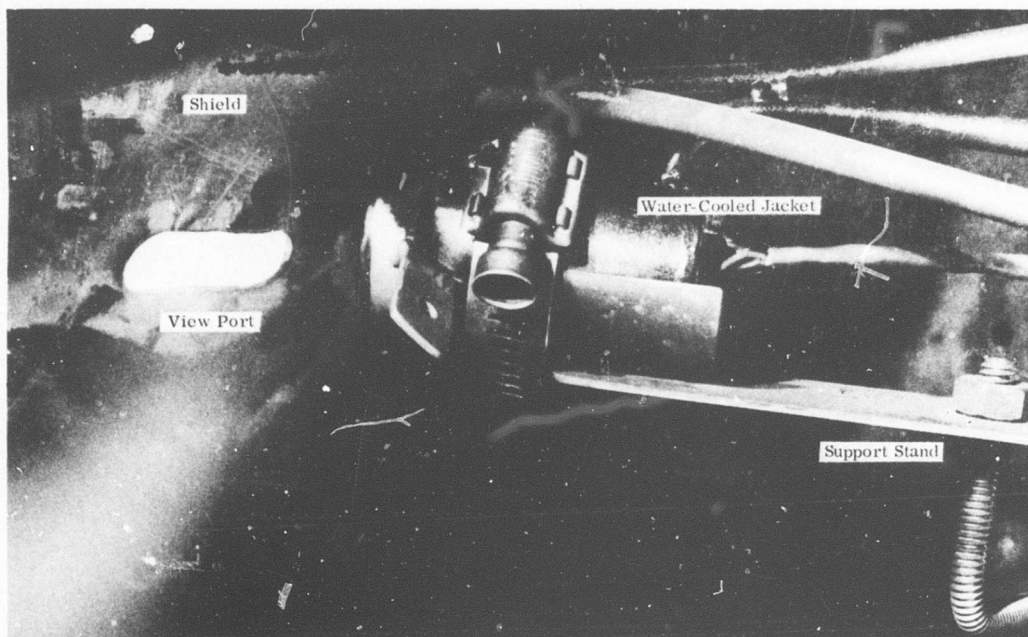
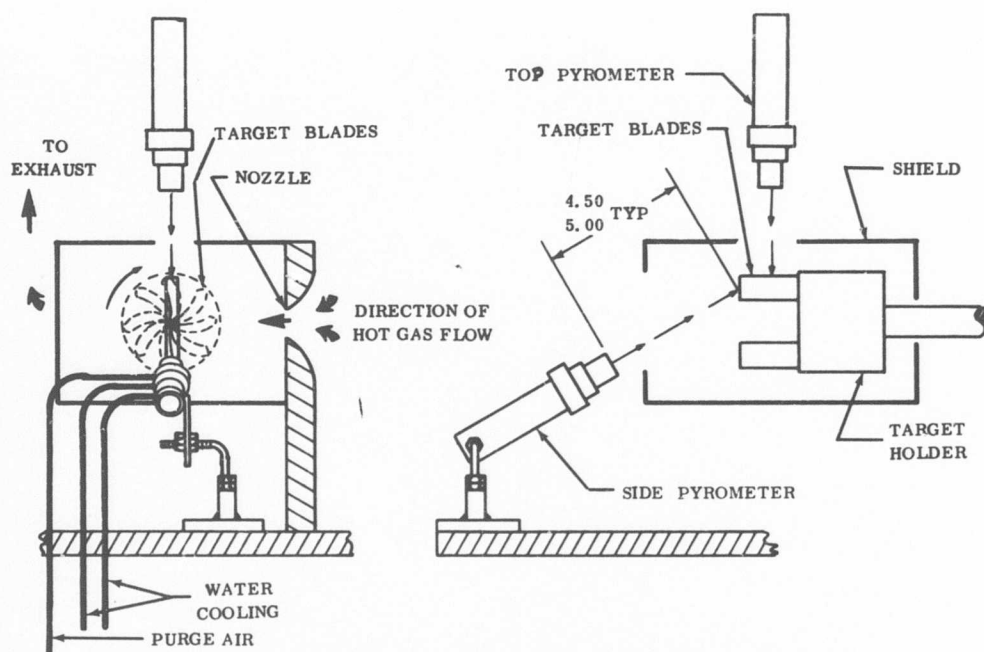


Figure 59. Simulated Atmosphere Test.



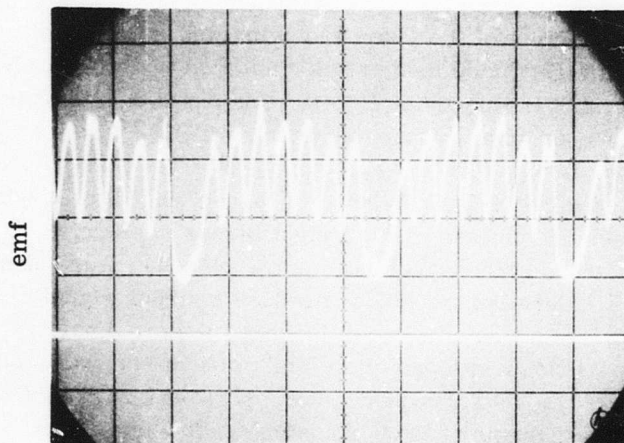
signal is proportional to area, the output of the side pyrometer was lower than that of the top-mounted one. The eight-blade holder was rotated at approximately 1725 rpm, producing a blade-passing frequency of 245 Hz. Internal blade temperature was measured with a chromel-alumel thermocouple at 1640°F.

Typical oscilloscope traces for several tests are shown in Figure 60. Figures 60A and 60B show the output of the side pyrometer with all eight blades in place. Figure 60A is an expanded view showing the waveform for two blades; Figure 60B shows three cycles of the holder. Three of the blades produce a higher signal than the other five, corresponding to a temperature difference of approximately 25°F. Figures 60C and 60D show traces with one of the eight blades removed. The side pyrometer viewing the tips of the blades recorded a missing peak with each revolution of the holder. The signal from the top pyrometer was completely different. When the empty position comes into view, the pyrometer views the back side of the blades opposite to the position of the missing blade. The trailing edge of the blade immediately in front of the missing position comes into view first, producing the highest peak of the cycle. As it disappears, the trailing edge of the blade opposite the empty position comes into view and a secondary peak is observed. The leading edge of the blade following the missing blade is seen next, and then the normal cycle is observed until the missing blade again appears. The missing blade disturbs the normal temperature symmetry, and each blade is at a distinct temperature depending on its relationship to the position of the missing blade.

The simulated atmosphere tests produced a clear signal corresponding to each target blade. Noise resulting from soot or the hot gas was not apparent even when the burner was adjusted to high fuel-to-air ratios. Noise from these sources is reported to increase with increasing pressure (Ref. 28), so atmospheric pressure tests only partially show that operation in high-pressure engines will be free from noise.

#### ENGINE TESTING

A radiation sensor was mounted on a Solar gas turbine engine to measure first-stage turbine blade temperature. This engine is a 1100-horsepower, single-shaft industrial engine with a nominal turbine inlet gas temperature of 1450°F. The basic test objective was to demonstrate the ability of the radiation sensor concept developed by this program to produce a clean, usable signal proportional to the temperature of the first-stage turbine blades. The sensor included a collimator interface, quartz objective lens, high-temperature fiber optic, silicon detector, and signal amplifier. The output from the sensor was displayed on an oscilloscope and a strip chart recorder. Selected events were also recorded on a high-speed Visicorder. Sixteen 1/2-hour tests were performed. The sensor was calibrated before and after most tests, and the sensor components were examined.



A.

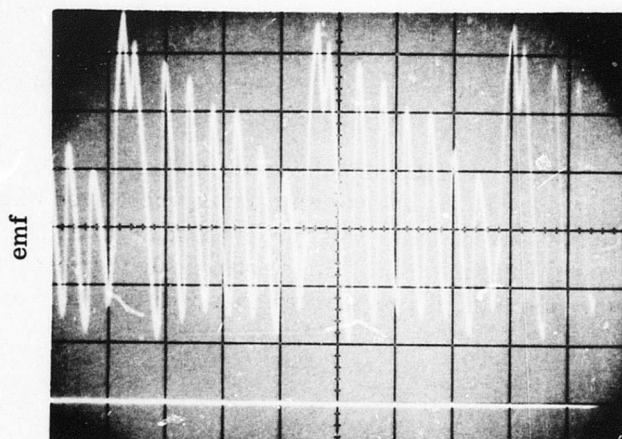
1.0 Millisecond/Division

0.1 Millivolt/Division

1000-Ohm Load

8 Blades

Time



B.

10 Milliseconds/Division

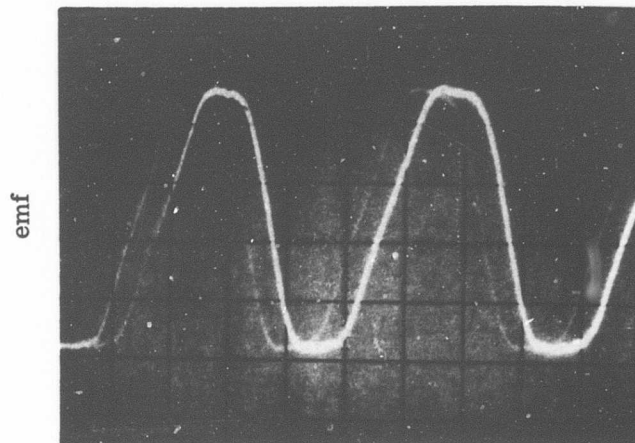
1 Millivolt/Division

10,000-Ohm Load

8 Blades

Time

Figure 60. Signal From Rotating Target Blades (Sheet 1 of 2).



C.

10 Milliseconds/Division

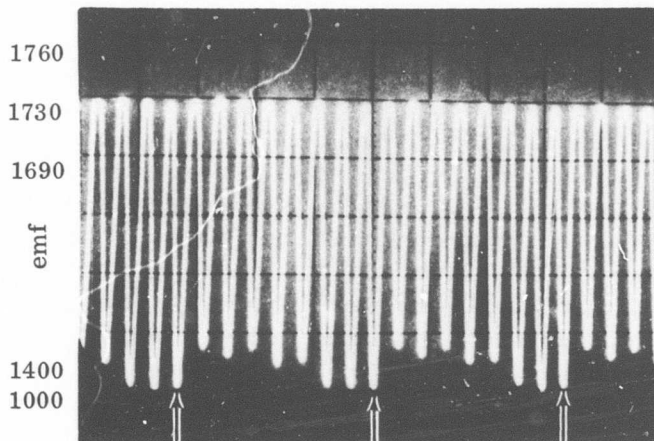
1 Millivolt/Division

10,000-Ohm Load

7 Blades

Zero emf

Time



D.

10 Milliseconds/Division

2 Millivolts/Division

10,000-Ohm Load

7 Blades

Zero emf

Time

Figure 60. Signal From Rotating Target Blades (Sheet 2 of 2).

First-stage turbine blade temperature was not measured independently, so no direct measurement of component or system accuracy was made. The engine testing demonstrated the feasibility and usefulness of direct turbine blade temperature measurement and delineated further work needed to advance the concept for application as a test cell diagnostic instrument and as a component of the control system for an advanced engine.

### Design and Fabrication

An experimental sensor was designed to fit the Saturn engine and to allow the maximum freedom of adjustment. A schematic diagram of the sensor is shown in Figure 61. A mounting boss, which positioned the optical housing containing the objective lens, fiber optic, and field aperture, was welded to the turbine case. A spherical seat on the mount allows adjustment of the direction of the optical axis by six bolts. The axial distance from lens to target is adjusted by spacers under the spherical seat. Purge air flows through the housing in front of the lens and through the collimator. Collimator passage size was 0.01 square inch. The detector was held at the end of the 2-foot fiber optic in a water-cooled housing (Figure 62). The detector was connected to the amplifier by approximately 40 feet of shielded cable. Figure 63 shows the sensor mount and optical housing.

The target-to-lens distance varied from 1.5 to approximately 2.1 inches as a given blade passed the field of view. A field aperture diameter of 0.150 inch produces a target diameter of 0.375 inch at the focal plane. The effective lens diameter is 0.4 inch. The sensor was calibrated using a resistance-heated strip of a high-temperature nickel-base alloy (Figure 64) as the target. The emittance was estimated to be approximately equal to the emittance of the turbine blades. Four calibrations are shown in Figure 65. Signals from both the first- and second-stage amplifiers were used. The temperature of the target was measured by three thermocouples tack welded to the back of the strip. This measurement was also compared to the reading from a disappearing filament pyrometer. The photocurrents produced at various temperatures with and without the collimator in place are listed in Table XIX.

The collimator transmitted an average of 79 percent of the incident radiation.

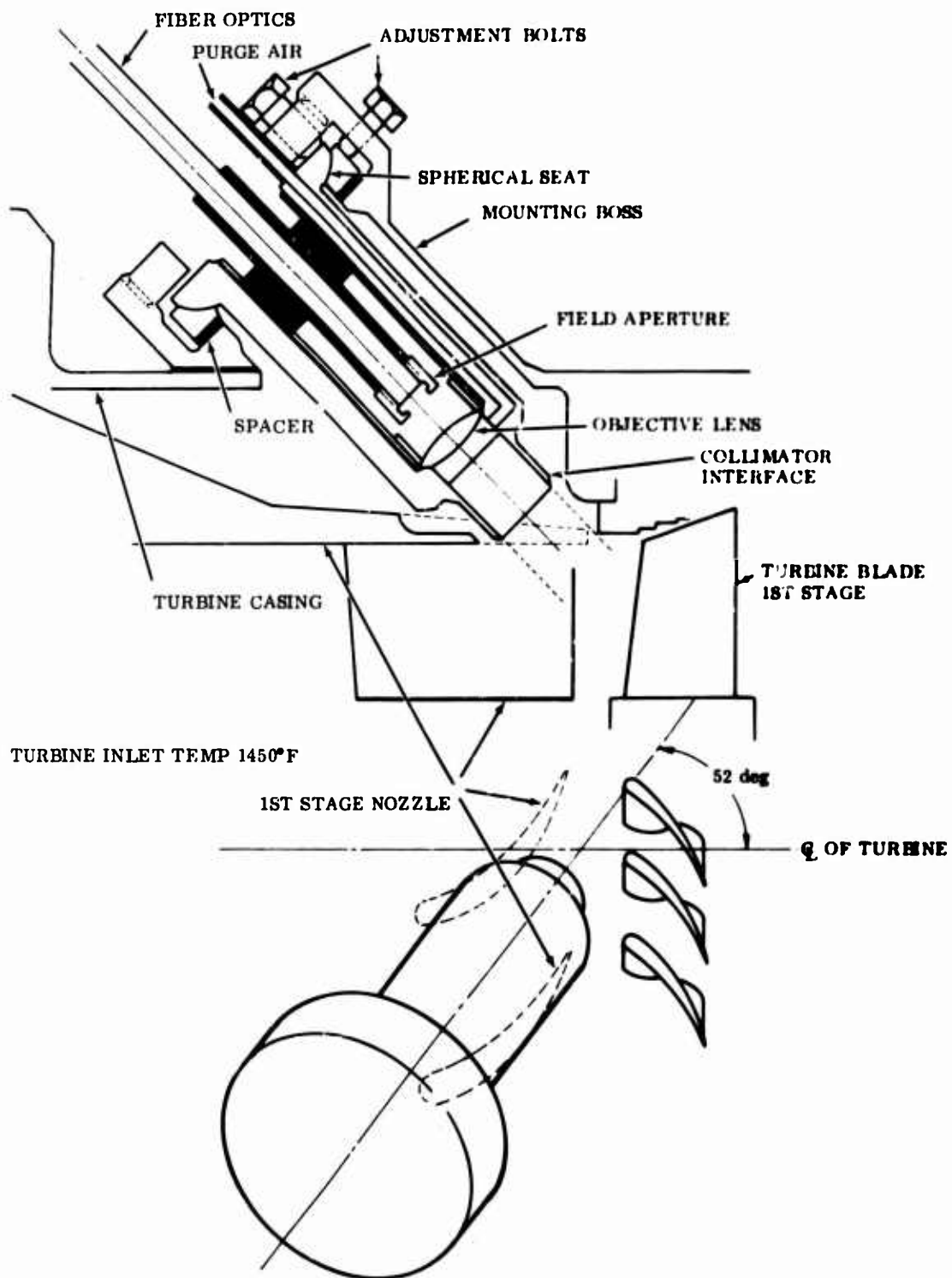
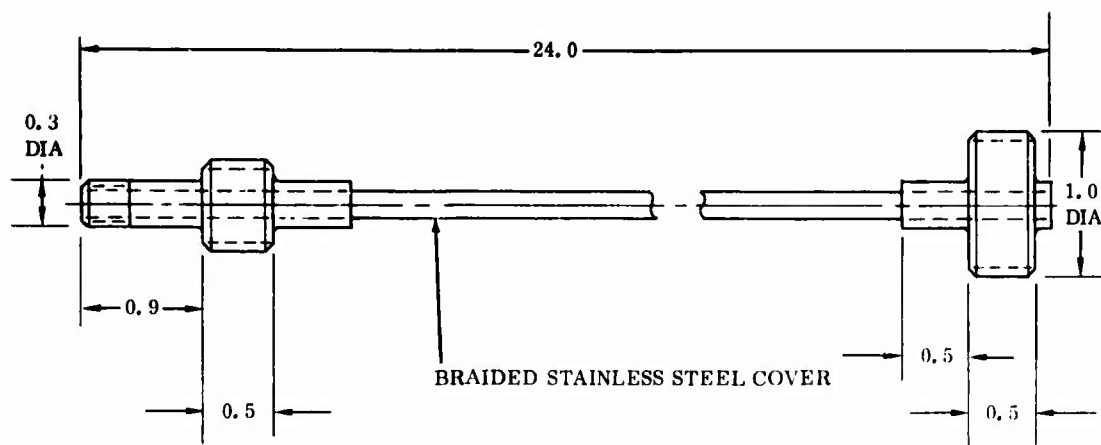


Figure 61. Radiation Sensor Mounted on the Test Engine.



NOTE: OPTIC BUNDLE DIAMETER TO BE 0.187 (3/16)

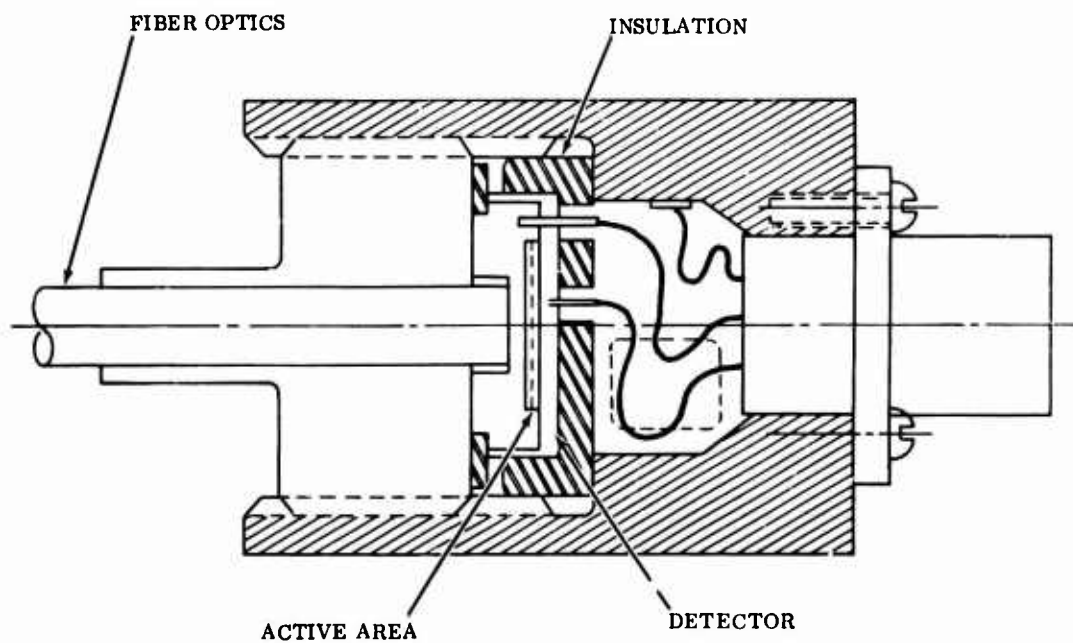


Figure 62. Detector Housing and Fiber Optic.

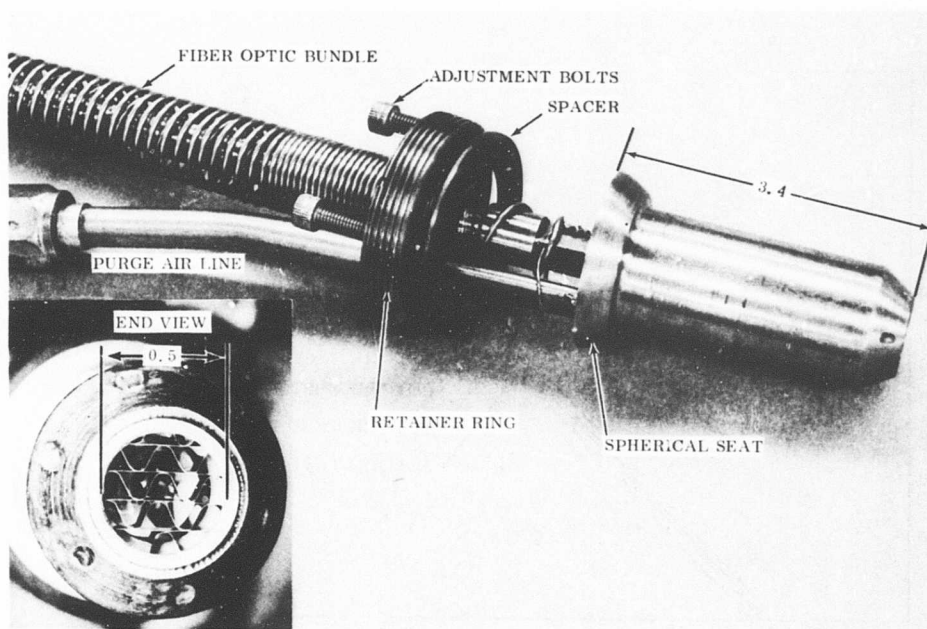
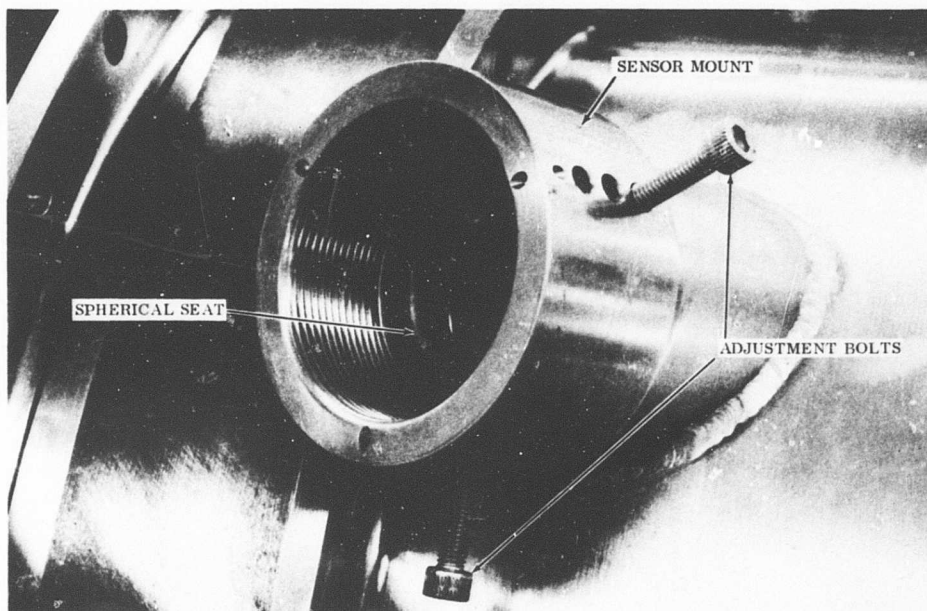


Figure 63. Sensor Mount and Optical Housing.



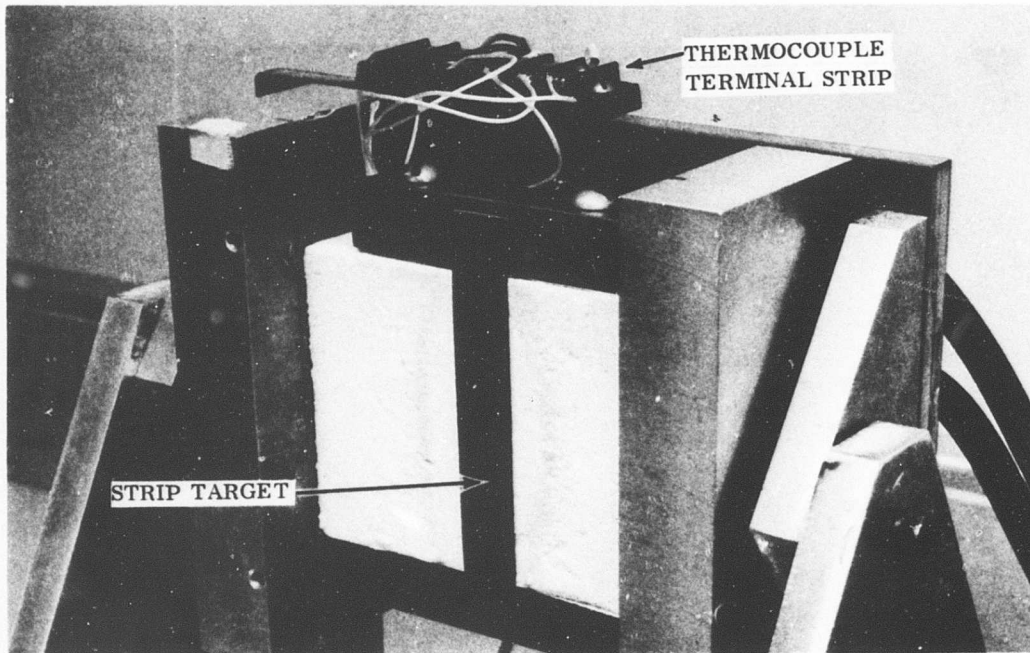


Figure 64. Calibration Target.

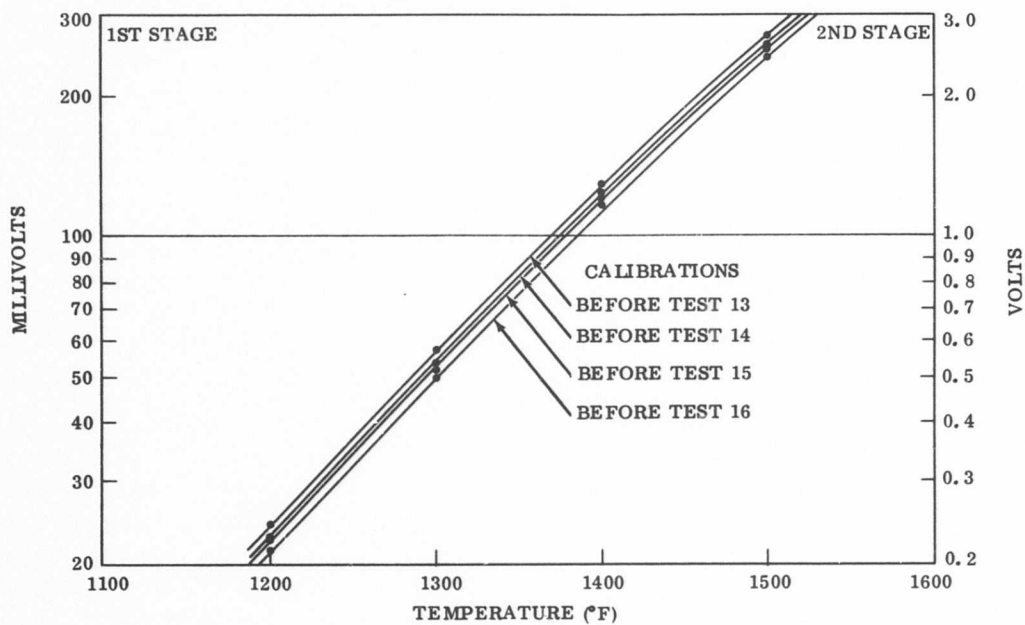


Figure 65. Saturn Sensor Calibration.



TABLE XIX. TRANSMISSION OF AIR COLLIMATOR			
Temperature (°F)	Current		Transmission (%)
	No Collimator (μa)	Collimator (μa)	
1100	0.27	0.21	78
1200	0.76	0.57	75
1300	1.9	1.4	75
1400	3.7	3.2	85
1500	8.7	7.3	83
Average Transmission			79

The transfer factor,  $F_t$  (equation 17), for the Saturn sensor was calculated using the following values:

$A_o$ 
= area of the objective lens
= 0.125 in.<sup>2</sup>

$A$ 
= area of the target
= 0.110 in.<sup>2</sup>

$\beta$ 
= coefficient of reflection
= 0.05

$\nu$ 
= number of lens faces
= 2

$\gamma_1$ 
= transmission by interface device
= 0.8

$\gamma_2$ 
= transmission by fiber optics
= 0.6

$D$ 
= distance from objective lens to target
= 1.75 in.

$F_t$ 
=  $6.2 \times 10^{-4}$  in.<sup>2</sup>

The signal current generated by the detector is given by equation (18).

The calculated current is compared to the experimental values in Table XX for several temperatures.

TABLE XX. DETECTOR CURRENT		
Temperature (°F)	Current	
	Calculated ( $\mu$ a)	Experimental ( $\mu$ a)
1100	0. 187	0. 200
1200	0. 602	0. 560
1300	1. 26	1. 40
1400	3. 12	3. 19
1500	6. 20	7. 24

The experimental sensor was installed on the test engine as shown in Figure 66. Thermocouples were attached to the sensor mount and to the turbine case to measure the thermal cycle history imposed on the sensor by each test run. A bracket held the detector housing independent of the engine.

**Test Results**

Each test was recorded continuously on a strip chart recorder. A typical example, the start of Test Number 15, is shown in Figure 67. First-stage amplifier output was recorded on the vertical scale. Chart speed was 2 inches/minute. The thermal cycle experienced by the blades during each engine start is clearly demonstrated by these results. During turbine acceleration, excess fuel is consumed and blade temperature rises at the rate of 25 degrees/second. The peak temperature was reached at approximately 30-percent shaft speed. As the compressor furnished more air, the temperature rapidly dropped until the full-speed (23,300 rpm), no-load condition was attained. Addition of load then gradually increased the turbine blade temperature until full load was reached. Ignition at faster shaft speeds decreased the height of the startup peak and thus caused less thermal shock to the turbine blades.

Second-stage amplifier output was recorded on an oscilloscope. Typical traces are shown in Figure 68. A relatively slow sweep rate, 5 milliseconds/division, is shown in Figure 68A from Test Number 15. The turbine makes approximately two revolutions in 5 milliseconds. This trace, taken at the steady-state, full-load condition, indicates an average temperature of approximately 1410°F with a high of 1430°F and a low of 1400°F. The indicated temperature is that temperature

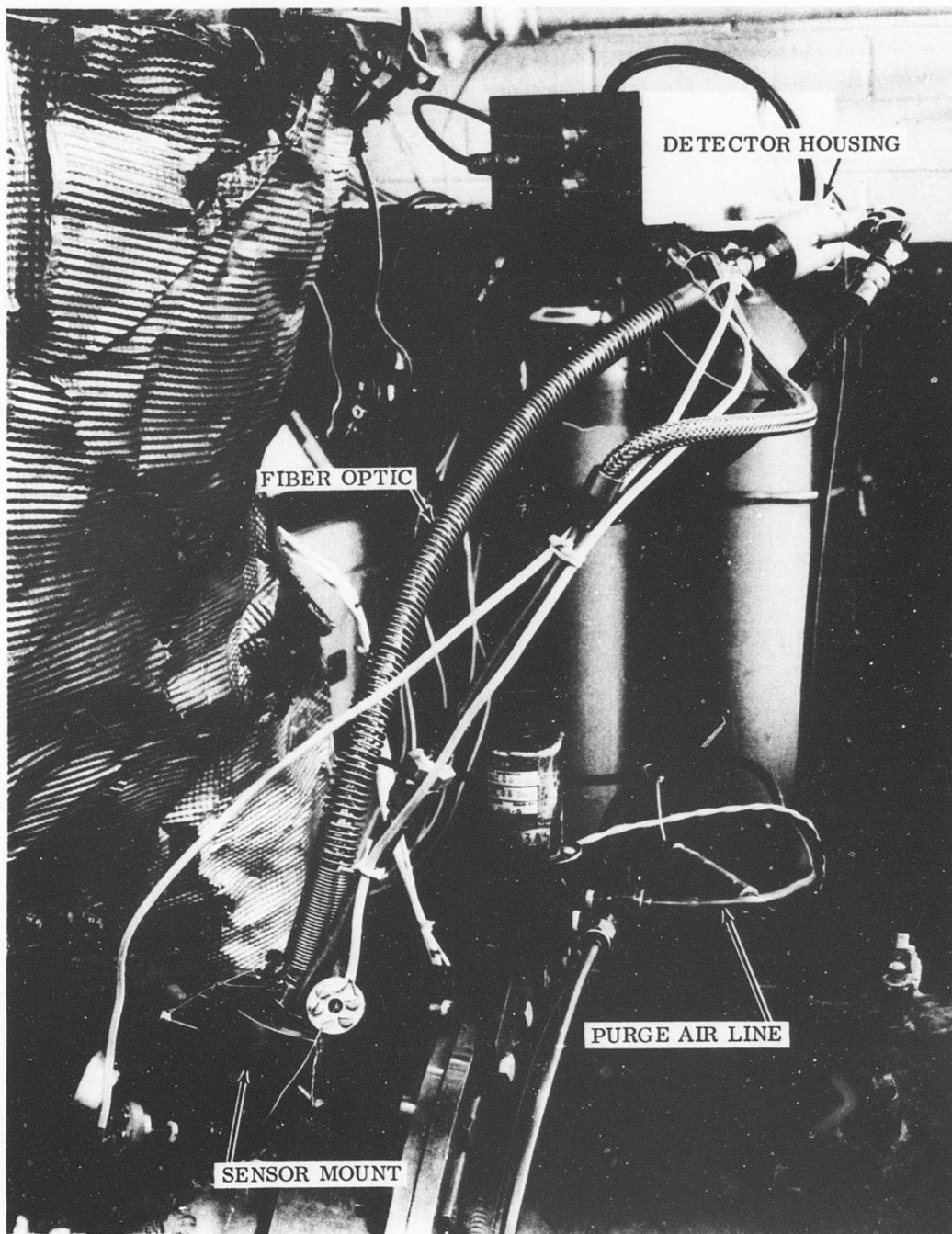


Figure 66. Saturn Test Engine With the Radiation Sensor.

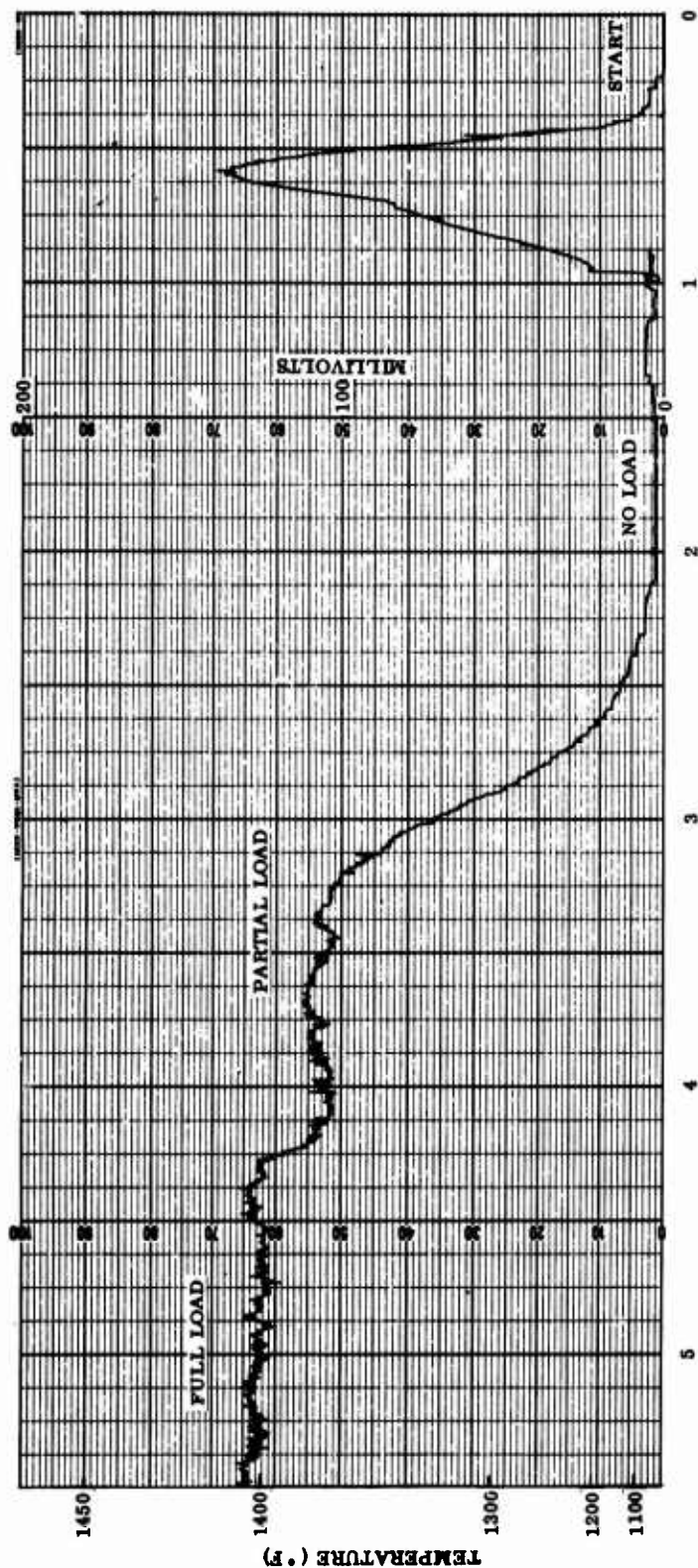
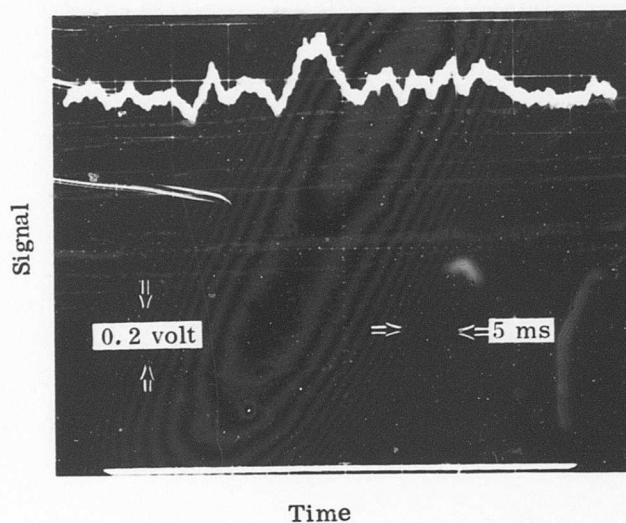


Figure 67. Start and Loading Cycle.



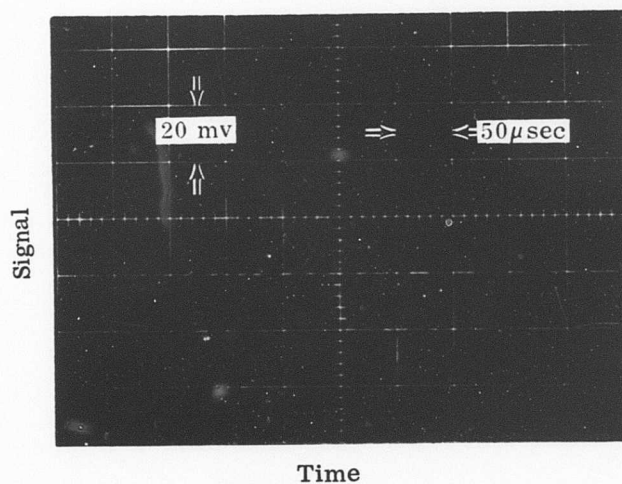
A.

Steady State

5 Milliseconds/Division

200 Millivolts/Division

Zero emf



B.

0.02 Millisecond/Division

20.0 Millivolts/Division

Figure 68. Oscilloscope Traces From Engine Tests.

that corresponds to the strip chart calibration. The effect of radiation reflected from the flame and other possible sources of error will be discussed. A fast-sweep time trace, 50 microseconds/division, is shown in Figure 68B. Each cycle corresponds to a blade passing the field of view of the sensor. A peak is measured as the tip of the leading edge enters the target area. As the blade advances, the target area drops down the front, concave side of the blade toward the root, which is at a lower temperature and produces a valley. This cycle is repeated for each blade. The amplifiers used during this test were not capable of handling the 20-kHz signal at the gain settings used, and so the amplitude of the waveform shown is considerably attenuated. Tests on a dynamic chopper rig, modulating a signal to the system at 20kHz, showed that the dynamic signal was attenuated to about 13 percent of the static value. Thus, an amplitude at about 300 millivolts was detected and attenuated to the 50 millivolts observed by the oscilloscope. Three hundred millivolts corresponds to a temperature gradient of 30 degrees from the tip of the blade to an area three quarters of the distance to the root.

Shutdown at the end of each test was recorded on a high-speed Visicorder. Shutdown for Test Number 15 is shown in Figure 69. Three parameters were recorded: fuel valve position, fuel pressure at the nozzle manifold, and sensor signal. Shutdown begins when the fuel valve is turned off (A, Figure 69); approximately 10 milliseconds later the fuel pressure drops (B, Figure 69) at the nozzle and the flame disappears. A few milliseconds after flame-out, the sensor signal begins to drop, very rapidly at first (C, Figure 69) and then more slowly. The initial drop of 30 millivolts occurs with a time constant of 5 milliseconds, which is a much faster cooling rate than would be expected from turbine blades. Disappearance of the flame is credited with causing the initial drop in signal, demonstrating that the indicated temperature was higher than true temperature because of reflected radiation. The nominal 1420°F reading was probably 30°F high. After the initial drop, the signal decayed with a calculated time constant of approximately 2 seconds, a reasonable value for turbine blade temperature change. An oscilloscope trace of the second-stage output (Figure 70) of the same event indicates that the initial drop might have been as much as 15 volts, which is equal to a 50-degree bias at 1420°F. A comparison of shutdown for two tests furnishes further evidence that the disappearance of reflected radiation from the flame causes the initial drop in signal (Figure 71). One test was run with diesel fuel and the other with JP-4. The two tests are shown superimposed, and it can be seen that there is a larger initial drop with diesel fuel than with JP-4. The difference was judged to have been caused by a greater flame luminosity with diesel than with JP-4 and thus more reflected radiation.



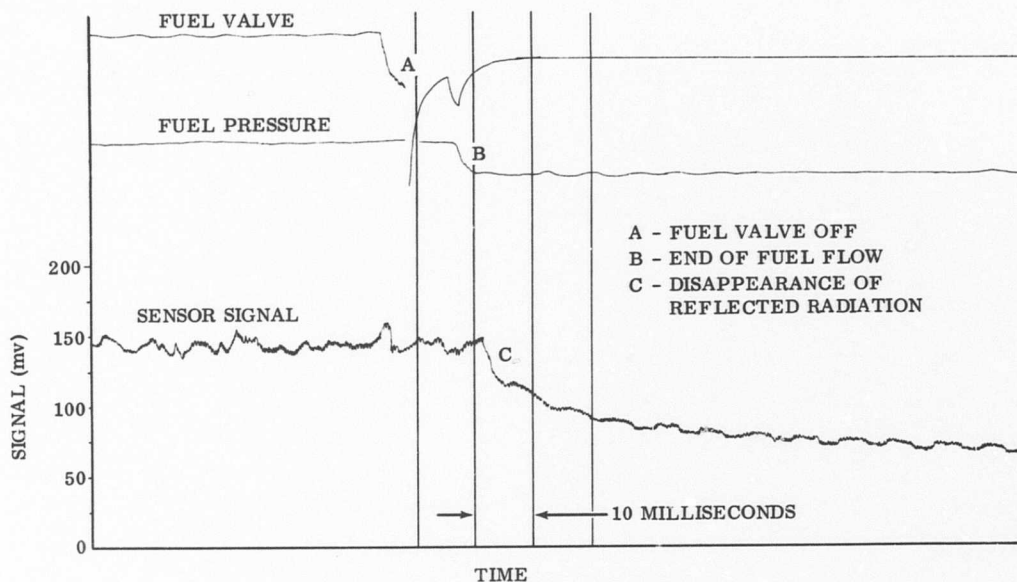


Figure 69. Engine Shutdown.

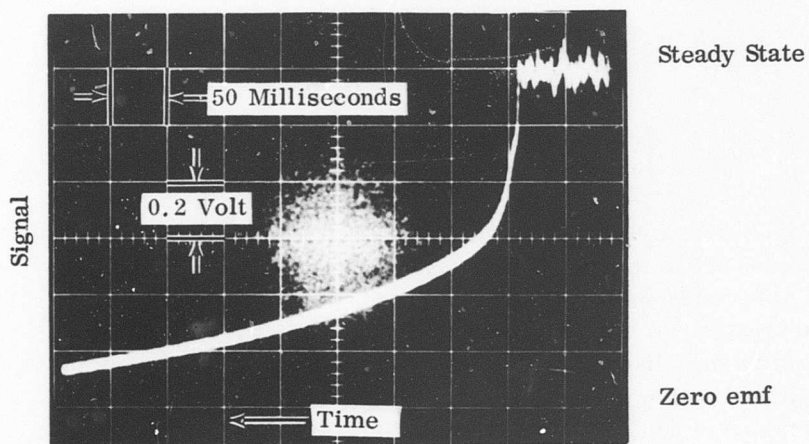


Figure 70. Oscilloscope Trace of Shutdown.

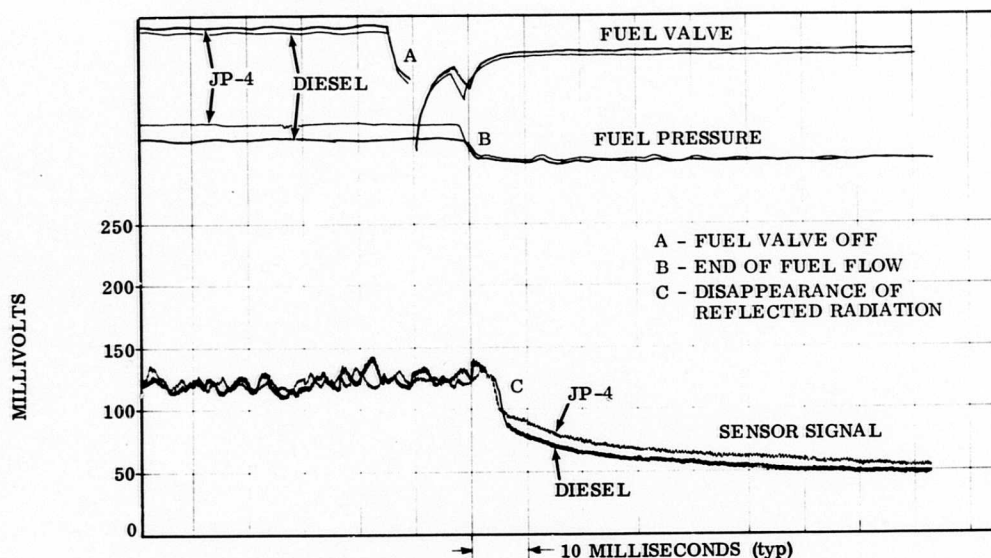


Figure 71. Effect of Fuel on Sensor Signal.

Even though the silicon detector avoids direct radiation from the hot gas, it is seen to be affected by the continuous radiation originating in the flame when viewed by the sensor directly or when reflected from the turbine blades. One solution to this problem is to view the back side of the blades to avoid all reflected radiation from the flame.

A clear optical path was maintained by the collimator interface throughout the test. Airflows of 1 to 8 standard cubic feet/second were used to purge the lens. No cracking or spalling of the lens was noted; a slight discoloration of the lens was detected during the first tests, but this did not reoccur and no noticeable effect on transmission was measured. The temperature of the optical housing was measured by a thermocouple pressed against the outside surface. Temperatures at steady state during a test were measured as high as 1050°F, with 750°F being more typical. Outside surface temperature was undoubtedly higher than the inside temperature to which the lens and fiber optic were subjected. Air temperature surrounding the optic housing was measured to be 1000° to 1050°F. The first recalibration, after Test Number 4, disclosed that there had been a large drop in transmission through the fiber optic. A thick layer of black powder had appeared on the front face of the fibers, causing a 150°F error in the blade temperature reading. Apparently the black powder was an organic substance used during manufacture



of the bundle, which had not been properly baked out prior to high-temperature use. Overtemperature conditions during the first test had caused the powder to oxidize and deposit onto the surface. No powder was found on any other part of the optical housing, indicating that it did not originate elsewhere. The fiber ends were cleaned, but small changes continued to occur in the calibration. A second fiber bundle was installed, and no measurable change in transmission occurred during the remaining four tests, indicating proper heat treating of the high-temperature end of the bundle before use. Increased purge airflow through the optic head kept the fiber bundle cooler, and no degradation in performance occurred. The maximum temperature measured at the optical head during the last four tests was 1010°F. The collimator interface and the detector performed well throughout the test. Thermal cycling did not cause any misalignment of the collimator passages. Maximum recommended fiber optic temperature is presently 1000°F for continuous duty.

#### CONCLUSIONS AND RECOMMENDATIONS

A solid-state radiation sensor was designed and tested to measure first-stage turbine blade temperature. Laboratory testing of the components and engine testing of the complete transducer demonstrated that a radiation sensor can operate on a gas turbine engine and produce a signal proportional to blade temperature.

The design consists of a silicon photovoltaic detector, a fiber optic bundle, an objective lens, an interface device, and a signal processor. Silicon detectors were operated at ambient temperatures up to 200°F. A dichroic filter in the optical system prevented signal changes resulting from ambient temperature change. The use of fiber optics allows remote placement of the detector away from hot engine parts.

Fiber optics withstood ambient temperatures up to 1000°F. The quartz objective lens was operated in severe thermal gradients without degradation. Testing of the interface devices was a qualitative comparison of different designs under specific geometric conditions. A collimator device operated satisfactorily during the engine testing. Operational amplifier circuitry allowed the use of the silicon detectors under short-circuit conditions.

The sensor operated successfully on a gas turbine engine. The sensor was able to respond to the blade-passing frequency (20,000 kHz) and resolve individual blades. Analysis of the shutdown cycle indicated that the signal was biased by reflected radiation from the flame. This effect may be avoided by viewing the backside of the blades.

Continued development of this concept is warranted. Two areas of testing deserve attention: long-term reliability of the individual components and testing of the system accuracy. Each of the several components must perform in a unique thermal and stress environment, and each must be tested to establish maximum environmental limitations that may then be used for the design of an operational system. End-to-end accuracy must also be experimentally established, first in a simulated environment and then in an engine. The system will then be ready for use as a diagnostic instrument for engine development and as an input transducer for control of advanced gas turbine engines.

#### LITERATURE CITED

1. Moffat, R. J. , GAS TEMPERATURE MEASUREMENT, Temperature, Its Measurement and Control in Science and Industry, Editor-in-Chief Herzfeld, C. M. , Reinhold, New York (1962), Vol. III, Part 2, Applied Methods and Instruments, ed. Dahl, A. I. , pp. 553-573.
2. Moffat, R. J. , DESIGNING THERMOCOUPLES FOR RESPONSE RATE, Transactions at the ASME, Vol. 80 (February 1959), pp. 267-297.
3. Gaylord A. M. , and Compton, W. A. , HIGH TEMPERATURE SENSORS FOR SMALL GAS TURBINES, Solar Division of International Harvester Company, Technical Report 67-76, U. S. Army Aviation Materiel Laboratories, Fort Eustis, Virginia (April 1968).
4. Sanders, V. D. , REVIEW OF HIGH-TEMPERATURE IMMERSION THERMAL SENSING DEVICES FOR IN-FLIGHT ENGINE CONTROL, The Review of Scientific Instruments, Vol. 29, No. II (November 1958), pp. 917-927.
5. Wasan, V. P. , and Gupta, C. L. , THERMOCOUPLES FOR HIGH TEMPERATURE MEASUREMENT, Engelhard Industries Technical Bulletin, Vol. 8, No. 3, (December 1967), pp. 77-92.
6. Caldwell, F. R. , THERMOCOUPLE MATERIALS, Temperature, Its Measurement and Control in Science and Industry, Editor-in-Chief Herzfeld, C. M. , Reinhold, New York (1962), Vol. III, Part 2, Applied Methods and Instruments, ed. Dahl, A. I. , pp. 81-134.
7. Zysk, E. D. , PLATINUM METAL THERMOCOUPLES, Temperature, Its Measurement and Control in Science and Industry, Editor-in-Chief Herzfeld, C. M. , Reinhold, New York (1962), Vol. III, Part 2, Applied Methods and Instruments, ed. Dahl, A. I. , pp. 135-175.
8. Burns, G. W. , and Gallagher, J. S. , REFERENCE TABLES FOR THE Pt-30 PERCENT Rh VERSUS VT-6 PERCENT Rh THERMOCOUPLE, Journal of Research, National Bureau of Standards - C - Engineering and Instrumentation, Vol. 89, No. 2, (April-June 1966), pp. 89-125.

9. Walker, B. E. , Ewing, C. T. , and Miller, R. R. , THERMOELECTRIC INSTABILITY OF SOME NOBLE METAL THERMOCOUPLES AT HIGH TEMPERATURES, The Review of Scientific Instruments, Vol. 33, No. 10 (October 1962), pp. 1029-1040.
10. Dahl, A. I. , and Fioch, E. F. , SHIELDED THERMOCOUPLES FOR GAS TURBINES, Transactions of the ASME (February 1949), pp. 153-161.
11. MODERN DEVELOPMENTS IN FLUID DYNAMICS, ed. Goldstein, S. , Oxford University Press (1938), pp. 421-424.
12. METHOD FOR CALIBRATION OF THERMOCOUPLES BY COMPARISON TECHNIQUES, ASTM E220-64, 1967 Book of ASTM Standards, American Society Testing and Materials, Philadelphia (1966), Part 30, pp. 647-664.
13. Olsen, L. O. , and Freeze, P. D. , REFERENCE TABLES FOR THE PLATINEL II THERMOCOUPLE, Journal of Research, National Bureau of Standards - C - Engineering and Instrumentation, Vol. 68C, No. 4 (Oct. - Dec. 1964), pp. 263-281.
14. Blackburn, G. F. , and Caldwell, F. R. , REFERENCE TABLES FOR 40 PERCENT IRIIDIUM-60 PERCENT RHODIUM VERSUS IRIIDIUM THERMOCOUPLES, Journal of Research, National Bureau of Standards, Vol. 66C, No. 1 (Jan. - Mar. 1962), pp. 1-12.
15. Bedford, R. E. , REFERENCE TABLES FOR PLATINUM 20% RHODIUM/ PLATINUM 50% RHODIUM THERMOCOUPLES, Review of Scientific Instruments, Vol. 35 (1964), pp. 1177-1190.
16. Zysk, E. D. , and Toenshoff, D. A. , CALIBRATION OF REFRACTORY METAL THERMOCOUPLES, Engelhard Industries Technical Bulletin, Vol. VII, No. 4 (Mar. 1967), pp. 137-146.
17. Blackburn, G. F. , and Caldwell, F. R. , REFERENCE TABLES FOR THERMOCOUPLES OF IRIIDIUM-RHODIUM ALLOYS VERSUS IRIIDIUM, Journal of Research, National Bureau of Standards, Vol. 68C, No. 1 (Jan. - Mar. 1964), pp. 41-58.
18. Wimber, R. T. , and Stetson, A. R. , DEVELOPMENT OF COATINGS FOR TANTALUM ALLOY NOZZLE VANES, Solar Division of International Harvester Company, CR-54529, National Aeronautics and Space Administration, Lewis Research Center, Cleveland, Ohio (July 1967).

19. Asamoto, R. R. , and Novak, P. E. , TUNGSTEN-RHENIUM THERMOCOUPLES FOR USE AT HIGH TEMPERATURES, Review of Scientific Instruments, Vol. 38, No. 8 (August 1967), pp. 1047-1052.
20. Zysk, E. P. , Toenshoff, D. A. , and Penton, J. , TUNGSTEN 3 RHENIUM VS TUNGSTEN 25 RHENIUM - NEW HIGH TEMPERATURE THERMOCOUPLE, Engelhard Industries Technical Bulletin, Vol. III, No. 4 (March 1963), p. 133.
21. Engelhard Data File Bulletin EL-6268-2.
22. Baker, H. D. , Rydye, E. A. , and Baker, N. H. , TEMPERATURE MEASUREMENT IN ENGINEERING, Volume II, John Wiley & Sons, New York (1961).
23. Franson, K. , Katz, S. , and Raisen, E. , SOME RADIATION CHARACTERISTICS OF BLACKBODY SOURCES, Temperature, Its Measurement and Control in Science and Industry, Vol. III, Part 1, Reinhold, New York (1962), p. 529.
24. Forsythe, W. E. , OPTICAL PYROMETRY, Temperature, Its Measurement and Control in Science and Industry, Reinhold, New York (1941), p. 1115.
25. Barber, R. , and Land, T. , THE PLACE OF PHOTOVOLTAIC DETECTORS IN INDUSTRIAL PYROMETRY, Temperature, Its Measurement and Control in Science and Industry, Vol. III, Part 2, Reinhold, New York (1962), p. 391.
26. Kamo, R. , Solbrig, C. , and Cooper, P. , EFFECTS OF COMBUSTION PRODUCTS FROM REGENERATIVE-TYPE AUTOMOTIVE GAS TURBINE, ASME Paper Number 63-WA-206 (1963).
27. Faitani, J. J. , SMOKE REDUCTION IN JET ENGINES THROUGH BURNER DESIGN, ASME Paper Number 680348 (1968).
28. Mossey, P. W. , EXPERIMENTAL PYROMETER FOR TURBINE BLADE TEMPERATURE MEASUREMENT, SAE Paper 690431 (1969).

Unclassified

Security Classification

DOCUMENT CONTROL DATA - R & D		
(Security classification of title, body of abstract and indexing annotation must be entered when the overall report is classified)		
1. ORIGINATING ACTIVITY (Corporate author)		2a. REPORT SECURITY CLASSIFICATION
Solar Division of International Harvester Company San Diego, California		Unclassified
		2b. GROUP
3. REPORT TITLE		
HIGH-TEMPERATURE SENSORS FOR SMALL GAS TURBINES		
4. DESCRIPTIVE NOTES (Type of report and inclusive dates)		
Final Report December 1967 - June 1969		
5. AUTHOR(S) (First name, middle initial, last name)		
A. Marshall Gaylord William A. Compton		
6. REPORT DATE	7a. TOTAL NO. OF PAGES	7b. NO. OF REFS
December 1969	118	28
8a. CONTRACT OR GRANT NO.	8b. ORIGINATOR'S REPORT NUMBER(S)	
DAAJ02-68-C-0043	USAAVLABS Technical Report 69-93	
b. PROJECT NO.	8c. OTHER REPORT NO(S) (Any other numbers that may be assigned this report)	
Task 1G162203D14416	Solar Report Number RDR 1645	
c.		
d.		
10. DISTRIBUTION STATEMENT		
This document is subject to special export controls, and each transmittal to foreign governments or foreign nationals may be made only with prior approval of US Army Aviation Materiel Laboratories, Fort Eustis, Virginia 23604.		
11. SUPPLEMENTARY NOTES		12. SPONSORING MILITARY ACTIVITY
		U. S. Army Aviation Materiel Laboratories Fort Eustis, Virginia
13. ABSTRACT		
<p>Temperature sensors for application to the turbine inlet of small gas turbine engines were developed. Two thermocouple designs to sense gas temperature were developed and tested. An optical sensor for first-stage turbine blade temperature measurement was tested in the laboratory and on a gas turbine engine. A bare multiple-junction platinum-rhodium thermocouple with a platinum-rhodium radiation shield was tested at temperatures to 2550°F. Response time, calibration, drift, and life were measured in a simulated gas turbine environment. A rugged, protected thermocouple was developed using advanced materials systems able to operate in an oxidizing environment to 2800°F. The probe consists of a W-3Re versus W-25Re thermoelement grounded in the flattened tip of a tantalum protection tube. The tube is coated by a duplex silicide coating to prevent oxidation of the refractory metal components. The unique flattened tip, fabricated by diffusion bonding techniques, maximizes the response rate of the probe. Response in moving gas and lifetime in a thermal shock cycle were measured. The radiation sensor consists of a silicon photovoltaic detector, a quartz lens, a high-temperature fiber optic bundle, an interface device, and a signal linearization system. It measures blade temperature and can resolve individual blades. The fiber optic bundle allows remote placement of the temperature-sensitive detector in a relatively cool environment. Silicon detectors provide high-temperature sensitivity and accuracy with an insensitivity to emittance and transmission errors. A unique interface device protects the optical system from transmission losses resulting from contamination of the optical system. Engine testing was performed with considerable success. The components functioned well over 16 start-endurance run-stop cycles. Reflected radiation from the flame caused a positive bias in temperature reading. Viewing of the backside of the blades will prevent this effect.</p>		

DD FORM 1473

REPLACES DD FORM 1473, 1 JAN 64, WHICH IS OBSOLETE FOR ARMY USE.

Unclassified

Security Classification

14. KEY WORDS	LINK A		LINK B		LINK C	
	ROLE	WT	ROLE	WT	ROLE	WT
high-temperature sensors gas turbines small gas turbines turbine controls turbine inlet temperature turbine blade temperature thermocouple thermocouple response noble metal thermocouple refractory metal thermocouple tungsten-rhenium thermocouple platinum-rhodium thermocouple grounded junction thermocouple radiation sensor silicon photovoltaic detector silicon detector pyrometer radiation pyrometry fiber optics light pipe quartz lens coated refractory metals						